Multi-Wavelength Study of Hot Stellar Populations in Galactic Globular Clusters

A thesis
submitted for the degree of

Doctor of Philosophy

in

The Department of Physics,
Pondicherry University,
Puducherry - 605 014, India

by

Deepthi S. Prabhu
Indian Institute of Astrophysics,
Bangalore - 560 034, India

July 2023

Multi-Wavelength Study of Hot Stellar Populations in Galactic Globular Clusters

Deepthi S. Prabhu
Indian Institute of Astrophysics

Indian Institute of Astrophysics
Bangalore - 560 034, India

Title of the thesis : **Multi-Wavelength Study of Hot Stellar Populations in Galactic Globular Clusters**

Name of the author : **Deepthi S. Prabhu**
Address : Indian Institute of Astrophysics
II Block, Koramangala
Bangalore - 560 034, India
Email : deepthi.prabhu@iiap.res.in

Name of the supervisor : **Prof. Annapurni Subramaniam**
Address : Indian Institute of Astrophysics
II Block, Koramangala
Bangalore - 560 034, India
Email : purni@iiap.res.in

Declaration of Authorship

I hereby declare that the matter contained in this thesis is the result of the investigations carried out by me at the Indian Institute of Astrophysics, Bangalore, under the supervision of Prof. Annapurni Subramaniam. This work has not been submitted for the award of any other degree, diploma, associateship, fellowship, etc. of any other university or institute.

Deepthi

Deepthi S. Prabhu
Ph.D. Scholar,
Indian Institute of Astrophysics,
Bengaluru-560034.

Date: 21st July 2023

Certificate

This is to certify that the thesis entitled **'Multi-Wavelength Study of Hot Stellar Populations in Galactic Globular Clusters'** submitted to Pondicherry University by Ms. Deepthi S. Prabhu for the award of the degree of Doctor of Philosophy is based on the results of the investigations carried out by her under my supervision and guidance, at the Indian Institute of Astrophysics. This thesis has not been submitted for the award of any other degree, diploma, associateship, fellowship, etc., of any other university or institute.

Prof. Annapurni Subramaniam
(Thesis Supervisor)
Indian Institute of Astrophysics,
Bengaluru-560034.

Date: 21^{st} July 2023

List of Publications

1. UV Photometry Of Spotted Stars In The Horizontal Branch Of The Globular Cluster NGC 2808 Using AstroSat*
Prabhu, D. S., Subramaniam, A. & Sahu, S.
Journal of Astrophysics & Astronomy, 42, 66 (2021). **Impact factor: 1.610**

2. The First Extensive Exploration Of UV-Bright Stars In The Globular Cluster NGC 2808*
Prabhu, D. S., Subramaniam, A. & Sahu, S.
The Astrophysical Journal, 908, 66 (2021). **Impact factor: 5.521**

3. Globular Clusters UVIT Legacy Survey (GlobULeS) I. FUV-optical Color-Magnitude Diagrams For Eight Globular Clusters
Sahu S., Subramaniam, A. et al. including **Prabhu, D. S.**
Monthly Notices of the Royal Astronomical Society, 514, 1122–1139 (2022).
Impact factor: 5.235

4. Prospects Of Measuring A Metallicity Trend And Spread In Globular Clusters From Low-Resolution Spectroscopy
Baratella, M., **Prabhu, D. S.**, Lima, L., & Prugniel, P.
Astronomy & Astrophysics, 661, A138 (2022). **Impact factor: 6.24**

5. Globular Clusters UVIT Legacy Survey (GlobULeS) III: Omega Centauri In Far-Ultraviolet*
Prabhu, D. S., Subramaniam, A., Sahu,S. et al.
The Astrophysical Journal Letters, 939, L20 (2022). **Impact factor: 8.811**

6. Globular Clusters UVIT Legacy Survey (GlobULeS) VI : Far-Ultraviolet Sources In The Nearby Globular Cluster NGC 6397*
Prabhu, D. S., Subramaniam, A., Sahu,S. et al., In preparation

---

*** Included in this thesis**

Conference Presentations

1. Poster presentation titled 'Exploring the enigmatic hot stellar population of the massive globular cluster NGC 2808 using UVIT', YAM 2019, held at Kodaikanal Solar Observatory, Kodaikanal, September 2019.
2. Contributed talk on 'The first extensive exploration of UV-bright stars in the globular cluster NGC 2808', 'MODEST 20 : Dense Star Clusters in the Era of Large Surveys', held at TIFR Mumbai, February 2020.
3. Contributed Talk on 'The First Extensive Exploration of UV-bright Stars in the Globular Cluster NGC 2808', 'UVIT : 5 years of Operation', held online during 1 - 3 December 2020.
4. Poster presentation, 'Re-assessment of the metallicity trend on the giants of the globular cluster NGC 6397, 'Precision Spectroscopy 21 - Stellar connections: from Galaxy evolution to exoplanets', held online, 1 - 3 Feb. 2021.
5. Contributed Talk on 'A census of UV-bright stars in the dense globular cluster NGC2́808' using UVIT-HST-GAIA', NUVA eMeeting 2021 'Status and new UV results from HST, Astrosat and LUT', held online during 26th & 27th October 2021.
6. Poster presentation titled 'Multi-wavelength study of the hot stars in massive globular clusters ω Centauri & NGC 2808', ASI meeting 2022, held at IIT Roorkee, March 2022.
7. Invited Talk on 'AstroSat/UVIT view of the most massive Galactic globular cluster Omega Centauri', IIA Foundation Day Symposium, held at IIA Bengaluru, during 31st March & 1st April 2022.
8. Contributed Talk on 'Massive Galactic globular clusters through the ultraviolet eyes of AstroSat/UVIT', COSPAR 2022 : 44th Scientific Assembly, held in Athens, Greece during 16 - 24 July 2022.
9. Invited Talk on 'Peculiar hot stars in the most massive Galactic globular cluster Omega Centauri as revealed by UVIT', Celebration of 7 years of AstroSat, at ISRO headquarters Bengaluru, during 28th & 29th Sept. 2022.

Acknowledgements

I wish to express my gratitude to everyone who helped me along the way to finishing this thesis. Without their invaluable assistance and encouragement, this work would not have been possible.

Firstly, I thank my thesis advisor Prof. Annapurni Subramaniam for her expert guidance and unwavering support throughout this journey. We had a lot of great science discussions in our personal meetings and with the research group. Her enthusiasm for science, contagious energy, and desire to constantly learn new things are motivating. I am truly fascinated by her time management skill and the ease with which she handles various roles and responsibilities. I sincerely thank her for helping me shape into an independent researcher.

I express my sincere thanks to Prof. Ram Sagar and Dr. Smitha Subramaniam for their valuable suggestions and feedback during the early years of my Ph.D. I am thankful to my research group members – Dr. Samyaday Choudhury, Dr. Snehalata Sahu, Sharmila Rani, Dr. Prasanta Nayak, Dr. Chayan Mondal, Dr. Sindhu Pandey, Dr. Vikrant Jadhav, Dr. Gaurav Singh, Ranjan Kumar, Sipra Hota, Dhanush, Arvind and others – for the discussions related to various topics. A special shout out to Snehalata and Sharmila for their help and support in learning various tools and techniques. I also wish to thank Prejwal Joseph for all the help related to UVIT data.

I want to thank my doctoral committee members, Prof. Gajendra Pandey and Prof. Ravikanth Kumar, for their valuable comments and suggestions. I sincerely acknowledge the Director, the Dean, and the members of the Board of Graduate Studies for providing a conducive environment for research at IIA. I am grateful to my coursework instructors and various faculty members at IIA and IISc. I

am immensely thankful to all the staff at the Library, Computer Center, UVIT-POC, and Administrative Section for their help in various aspects. My heartfelt gratitude to the service provided by the non-academic staff at IIA and at the Bhaskara guest house.

Many thanks to all my scientific collaborators for their input and immense support. I gratefully acknowledge Prof. Pavel Kroupa, Dr. Marilyn Latour, Dr. Yazan Momany, and Dr. Simone Zaggia for hosting my visit at their respective institutes.

At this juncture, I acknowledge the contributions of all my teachers in school and college, who have played a crucial role in developing my passion for science and also helped me grow as an individual.

Friends become your pillar of support during the long and rugged path towards a doctorate. I am lucky to have the company of Fazlu and Sonith, who have seen me at my worst and held my hands during the toughest times. I thank my dear friends Sioree, Indrani, Athira, Anirban, Swastik, Bharat, Partha, Sharmila, Satabdwa, Bibhuti, Manika, Suman, and Soumya for their care and support. Many thanks to all my juniors and seniors for all the help and memorable experiences at Bhaskara.

I am forever indebted to my best friends Bhavya, Reshma K.S., Reshma I., Swathy, Neethu, and Kavya for being my constants. I thank my friend Sachin for his care during the most testing times. I am also grateful to all my other friends who have helped and supported me at various stages in my life.

I am at a loss for words to express my gratitude to my family. I cannot thank my father, Sarvothama Prabhu, and my mother, Usha S. Prabhu, enough for their sacrifices and struggles. Their unconditional love, patience, and belief in my abilities have been a constant source of strength. Lots of love to my brother, Damodar S. Prabhu, for his care, support, and sacrifices. Without his guidance, I would not have evolved into the person I am today. I am extremely grateful to my parents-in-law, Ramesh Chandra and Jai Moorti, for their wholehearted encouragement in carrying out my work without hindrance. This acknowledgment would be incomplete without mentioning the role of my long-term partner and now husband, Sunil Chandra. I value him for tolerating all my idiosyncrasies and mood swings throughout these years. He inspires me to dream big and is a constant source of motivation for me. I am also grateful for the love and support of all my other family members.

Finally, I want to express my sincere gratitude to the frontline personnel who aided during the COVID-19 pandemic. Only because of their tireless efforts did we manage to survive.

Deepthi

Data usage

The research described in the thesis made use of data obtained from multiple space and ground-based facilities. I express my sincere gratitude to the individual instrument teams for making the data available.

The majority of the thesis work was done utilizing UVIT data from the Indian Space Research Organisation's (ISRO) AstroSat mission, which has been maintained at the Indian Space Science Data Centre (ISSDC). UVIT project is a result of collaboration between IIA, Bengaluru, IUCAA, Pune, TIFR, Mumbai, several centers of ISRO, and the Canadian Space Agency (CSA). Several groups from ISAC (ISRO), Bengaluru, and IISU (ISRO), Trivandrum have contributed to the design, fabrication, and testing of the payload. The Mission Group (ISAC) and ISTRAC (ISAC) continue to provide support in making observations with, receiving, and initially processing the data. I deeply acknowledge the contributions made by each member of the team.

Additionally, I made use of the publicly available catalogs based on observations from other space-based facilities such as *GALEX*, *HST*, and *Gaia*. I have used the *GALEX* archival data available at the Mikulski Archive for Space Telescopes (MAST) portal of the Space Telescope Science Institute (STScI). *GALEX* is operated for NASA by the California Institute of Technology under NASA contract NAS5-98034. I have also used the publicly available catalogs based on observations from the *Hubble Space Telescope*. I have used the catalogs based on the data from the Gaia mission of the European Space Agency (ESA). This data is processed by the Gaia Data Processing and Analysis Consortium (DPAC). Funding for the DPAC has been provided by national institutions, in particular, the institutions participating in the Gaia Multilateral Agreement.

The photometric analysis in the thesis was carried out using the software package, Image Reduction and Analysis Facility (IRAF). IRAF is distributed by the National Optical Astronomy Observatory (NOAO), which is operated by the Association of Universities for Research in Astronomy (AURA) under a cooperative agreement with the National Science Foundation. Additionally, I used the virtual observatory tool, VO SED Analyzer (VOSA), developed under the Spanish Virtual Observatory project supported by the Spanish MINECO through grant AyA2017-84089. This work also made use of software tools such as TOPCAT, Matplotlib, IPython, and Astropy, a community-developed core Python package for Astronomy.

Dedicated to

my mother, Usha S. Prabhu,

& my father, Sarvothama Prabhu

Abstract

Galactic Globular clusters (GGCs) are old stellar systems (age $\sim$ 12 Gyr) consisting typically of about 10^4-10^6 gravitationally bound stars. This makes them excellent astrophysical laboratories to study stellar evolution, particularly at the low-mass end, as well as the role of dynamical processes in the evolution of stars. GGCs are now widely accepted to host stars with variations in light element abundances and/or ages, a phenomenon known as multiple stellar populations (MSPs). The origin of MSPs in GGCs is still an open problem, with several scenarios proposed in the literature.

The hot stellar populations ($T_{\rm eff} \gtrsim 5\,500\,{\rm K}$) in GGCs exist in various advanced, relatively fast-paced stages of low-mass stellar evolution such as horizontal branch (HB; He-core burning phase) including extreme HB (EHB; $T_{\rm eff} > 20\,000\,{\rm K}$), post-horizontal branch (pHB; post-He-core burning phase) and white dwarf (WD). The census and characterization of these stellar populations are crucial to test and improve the models of late evolutionary stages. By studying GGCs with a broad HB color distribution, the MSP phenomenon, especially in terms of helium enhancement, can be probed. In a broader context, the EHB stars and their progeny are speculated to be causing the 'UV-upturn' seen in the spectra of elliptical galaxies, making their study highly relevant. Hot stars in GGCs additionally include non-canonical objects such as blue stragglers as well as exotic systems, including cataclysmic variables and other close binaries. The detection and characterization of such sources can shed light on the interplay between stellar evolution and stellar dynamics, in turn, the cluster's dynamical evolution itself.

The main goal of this thesis is to undertake the census and characterization of hot stellar populations in GGCs in order to : (a) shed light on the late stages of low-mass stars' evolution, (b) identify the formation pathways of non-canonical stars, (c)

trace multiple stellar populations and their origins, and (d) understand the effects of dynamical interactions on stellar evolution. To achieve these aims, a multi-wavelength study of hot stars in three GGCs is conducted. Out of these, two clusters, NGC 2808 and ω Centauri (NGC 5139), are massive and dense. Both these clusters have a wide color distribution of HB stars, including a significant population of EHB stars and pHB stars, as well as He-enriched populations. The third cluster is NGC 6397, a low-mass, nearby, core-collapsed cluster ideal for understanding the properties of exotic sources. The thesis mainly uses the ultraviolet (UV) data from the Ultra Violet Imaging Telescope (UVIT) onboard the Indian space observatory, *AstroSat*. In order to identify the optical counterparts of the UV sources, the published catalogs based on observations from the *HST*, $Gaia$, and ground-based telescopes are used.

The first complete census and characterization of the pHB population in NGC 2808 revealed that most are AGB-manqué stars that have bypassed the asymptotic giant phase altogether after core-He-burning and are expected to progress directly to the WD stage. The UV properties of EHB stars, speculated to be plagued by magnetic spots, are studied. This indicated interesting tentative correlations between their rotational periods and UV magnitudes, though it requires further investigation. The first far-UV photometric study of the most massive GGC ω Centauri helped to disentangle the MSPs along the HB and shed light on the peculiarities in the hot HB and WD populations. The study pointed to the origin of the second-generation stars in the system from the ejecta of intermediate-mass AGB stars and helped achieve constraints on the formation models of ω Centauri in terms of the estimated range in age, [Fe/H], and Y (in particular), for the HB sub-populations. In NGC 6397, exotic BSS binaries, possibly formed through the mass-transfer pathway, are detected. Several He-core WD candidates are also detected in the cluster.

This dissertation highlights the importance and advantages of UV observations using facilities such as the *AstroSat*/UVIT in the studies of hot stellar populations, even in the central regions of massive and dense clusters.

Contents

List of Figures

List of Tables

Abbreviations

ACS	**A**dvanced **C**amera for **S**urveys
α^2 **CVn**	α^2 **C**anum **V**enaticorum
AGB	**A**symptotic **G**iant **B**ranch
APOD	**A**stronomy **P**icture **o**f the **D**ay
BaSTI	**B**ag of **S**tellar **T**racks and **I**sochrones
BHB	**B**lue **H**orizontal **B**ranch
BHk	**B**lue **H**oo**k**
bMS	**b**lue **M**ain **S**equence
BS	**B**lue **S**traggler
BSS	**B**lue **S**traggler **S**tar
CCD	**C**harge **C**oupled **D**evice
CCP	**C**olor-**C**olor **P**lane
CMD	**C**olor **M**agnitude and **D**iagram
CMOS	**C**omplementary **M**etal **O**xide **S**emiconductor
COS	**C**osmic **O**rigins **S**pectrograph
CPM	**C**harge **P**article **M**onitor
CV	**C**ataclysmic **V**ariable
CZTI	**C**admium **Z**inc **T**elluride **I**mager
Decl.	**Decl**ination
E-AGB	**E**arly-**A**symptotic **G**iant **B**ranch
EHB	**E**xtreme **H**orizontal **B**ranch
EHF	**E**arly **H**ot **F**lasher

FG	**F**irst **G**eneration
FITS	**F**lexible **I**mage **T**ransport **S**ystem
FOV	**F**ield **O**f **V**iew
FUV	**F**ar **U**ltra-**V**iolet
FWHM	**F**ull **W**idth at **H**alf **M**axmimum
GALEX	**G**alexy **E**volution **E**xplorer
GC	**G**lobular **C**luster
GGC	**G**alactic **G**lobular **C**luster
GlobULeS	**Glob**ular Cluster **UV**IT **Le**gacy **S**urvey
H-R	**H**ertzsprung-**R**ussel
HB	**H**orizontal **B**ranch
hHBs	**h**ot **H**orizontal **B**ranch **s**tars
HST	**H**ubble **S**pace **T**elescope
HUGS	**H**ubble Space Telescope **UV** **G**lobular Cluster **S**urvey
IRAF	**I**mage **R**eduction and **A**nalysis **F**acility
ISRO	**I**ndian **S**pace **R**esearch **O**rganization
ISSDC	**I**ndian **S**pace **S**cience **D**ata **C**enter
L0	**L**evel **0**
L1	**L**evel **1**
L2	**L**evel **2**
LAXPC	**L**arge **A**rea **X**-ray **P**roportional **C**ounter
LHF	**L**ate **H**ot **F**lasher
LTE	**L**ocal **T**hermodynamic **E**quilibrium
MAST	**M**ikulski **A**rchive for **S**pace **T**elescopes
MCP	**M**icro**C**hannel **P**late
MS	**M**ain **S**equence
MSPs	**M**ultiple **S**tellar **P**opulation**s**
MSTO	**M**ain **S**equence **T**urn-**O**ff
MT	**M**ass **T**ransfer
MUSE	**M**ulti **U**nit **S**pectroscopic **E**xplorer

NASA	**N**ational **A**eronautics and **S**pace **A**dministration
NIR	**N**ear-**I**nfra**R**ed
NLTE	**N**on **L**ocal **T**hermodynamic **E**quilibrium
NUV	**N**ear **U**ltra-**V**iolet
OC	**O**mega **C**entauri
OpC	**Op**en **C**luster
pAGB	**p**ost **A**symptotic **G**iant **B**ranch
peAGB	**p**ost-**e**arly-**A**symptotic **G**iant **B**ranch
pHB	**p**ost-**H**orizontal **B**ranch
pHeCB	**p**ost **He**-**C**ore-**B**urning
PM	**P**roper **M**otion
PSF	**P**oint **S**pread **F**unction
R.A.	**R**ight **A**scension
RGB	**R**ed **G**iant **B**ranch
RHB	**R**ed **H**orizontal **B**ranch
rMS	**r**ed **M**ain **S**equence
RRLy	**RR** **Ly**rae
SED	**S**pectral **E**nergy **D**istribution
SG	**S**econd **G**eneration
SGB	**S**ub-**G**iant **B**ranch
SSM	**S**canning **S**ky **M**onitor
SSP	**S**imple **S**tellar **P**opulation
STIS	**S**pace **T**elescope **I**maging **S**pectrograph
STScI	**S**pace **T**elescope **Sc**ience **I**nstitute
SX Phe	**SX** **Ph**oenicis
SXT	**S**oft **X**-ray **T**elescope
TAHB	**T**erminal-**A**ge **H**orizontal **B**ranch
TMAP	**T**übingen NLTE **M**odel **A**tmosphere **P**ackage
TOPCAT	**T**ool for **OP**erations on **C**atalogues **A**nd **T**ables
TP-AGB	**T**hermally **P**ulsing **A**symptotic **G**iant **B**ranch

UIT	**U**ltraviolet **I**maging **T**elescope
UL2P	**U**VIT **L**evel-**2** **P**ipeline
UV	**U**ltra-**V**iolet
UVIS	**UV**/**VIS**ible Channel
UVIT	**U**ltra-**V**iolet **I**maging **T**elescope
UVOT	**U**ltraviolet-**O**ptical **T**elescope
vEHB	**v**ariable **E**xtreme **H**orizontal **B**ranch
(V)LTP	(**V**ery) **L**ate **T**hermal **P**ulse
VIS	**VIS**ible
VLT	**V**ery **L**arge **T**elescope
VOSA	**VO** **S**ED **A**nalyser
WCS	**W**orld **C**oordinate **S**ystem
WD	**W**hite **D**warf
WFC	**W**ide-**F**ield **C**hannel
WFC3	**W**ide **F**ield **C**amera **3**
WFPC2	**W**ide **F**ield and **P**lanetary **C**amera **2**
ZAHB	**Z**ero **A**ge **H**orizontal **B**ranch
ZAMS	**Z**ero **A**ge **M**ain **S**equence

Chapter 1

Introduction

Stars are to galaxies as galaxies are to the Universe – fundamental building blocks. Stars are born mostly in groups, from the collapse of molecular clouds having complex morphological hierarchies and masses ranging from 10^3-10^7 $M_\odot$, subject to various physical and kinematic conditions (See the review by Krause et al. 2020). Such a group is called a *star cluster* if there are at least 12 stars held together by gravity within a certain volume that is not dominantly composed of dark matter (Krause et al. 2020). If the stars are not bound gravitationally, the group is known as an *association* (Gieles & Portegies Zwart 2011; Adamo et al. 2020), and these generally consist of massive stars.

There are mainly two types of star clusters in the Milky Way:

1). Open Clusters (OpCs) – which are loosely bound, relatively young ($\lesssim$ 6 Gyr), having masses $\lesssim$ 5000 $M_\odot$ and found in the Galactic disk. An example of an OpC is shown in the left image of Fig. 1.1.

FIGURE 1.1: *Left*: Open Cluster M34 (Credits: Bob Franke, NASA APOD 2010 February 11). *Right*: Globular Cluster NGC 104 (Credits: Jose Mtanous, NASA APOD 2020 October 24)

2). Globular Clusters (GCs) – which are tight stellar agglomerations that are old (mostly $\gtrsim$ 10 Gyr), having masses $\gtrsim 10^4$ $M_\odot$ and associated with mainly the halo and the bulge (Kharchenko et al. 2013). A typical GC is shown in the right image of Fig. 1.1.

The next section goes into further depth on Galactic GCs (GGCs), which form the subject of this dissertation.

1.1 Globular Clusters

GCs are roughly spherical and consist of 10^4-10^6 gravitationally bound stars. The classic work by Shapley (1918) on the distances and structural parameters of GGCs paved the way for our current understanding of these sources.

GGCs are old systems with ages mostly greater than 10 Gyrs. Their ages can be used to constrain the age of the Universe independent of cosmological models (Krauss & Chaboyer 2003; Valcin et al. 2021). As fossil relics from the time of the

Galaxy's formation, GGCs are fundamental to our knowledge of the origin and chemical evolution of the Galaxy. Distributed in the halo, thick disk, and bulge, there are 157 known GGCs as per the catalog by Harris (1996, 2010 edition).

Structurally, GCs can be described on the basis of three types of radii : (i) *core radius*, r_c – the radius at which the surface brightness falls to half of the value at the center, (ii) *half-mass radius*, r_h – the radius that encloses half of the system's mass, and (iii) *tidal radius*, r_t – the radius at which the host galaxy's gravitational field becomes more significant than the cluster's self-gravity (Binney & Tremaine 2008). The median values corresponding to r_c, r_h and r_t for GGCs are respectively, 1 pc, 3 pc and 35 pc (Harris 1996).

In terms of chemistry, GC stars were classically conceptualized as being homogeneous. However, with innumerable photometric and spectroscopic investigations, it is now widely accepted that GGCs host populations differing in chemistry and/or age, a phenomenon commonly known as *multiple stellar populations* ($MSPs$; See the recent reviews by Bastian & Lardo 2018; Gratton et al. 2019; Milone & Marino 2022). The presence of anti-correlations in the abundances of light elements among member stars is now accepted to be a characteristic of GCs (Carretta et al. 2010). More details on MSPs are included in Section 1.4.

1.2 Evolution of GC Stars

Stars in GCs have different masses as set by the initial mass function (IMF) and are found in various phases of evolution depending on the cluster age. Fig 1.2 shows a snapshot in time of the GGC M55 represented by the color-magnitude diagram (CMD), where the main stellar evolutionary sequences are depicted. The changes in the stellar properties as stars evolve are reflected in the CMD, and hence, analyzing the CMD greatly contributes to our understanding of stellar evolution.

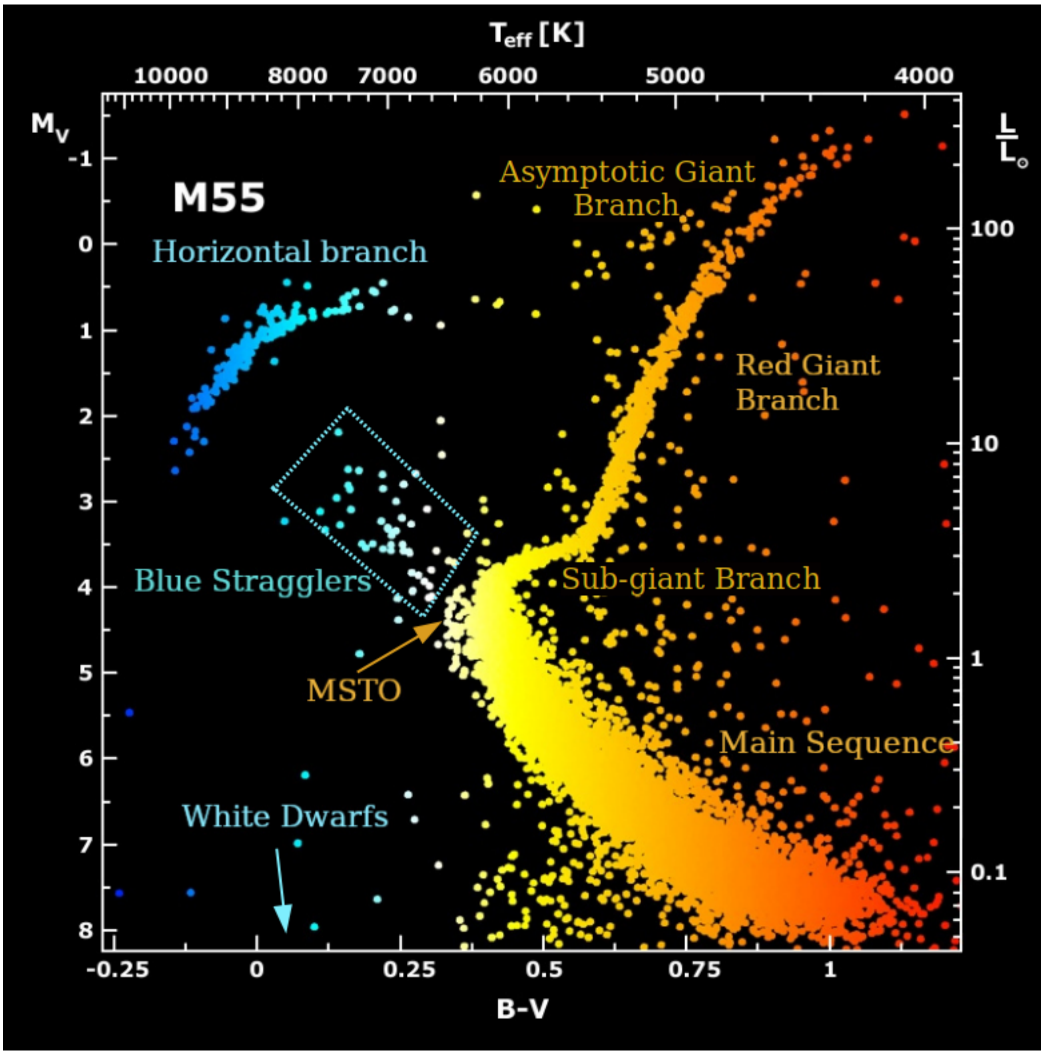

FIGURE 1.2: Color-magnitude diagram of GC M55 Cluster (Modified version of the NASA APOD on 2001 February 23. Original Credits: B.J. Mochejska, J. Kaluzny, 1 m Swope Telescope).

Most of the stars on the CMD are located on the *main sequence (MS)* where hydrogen (H) in the core is fused to helium (He). Stars with higher mass undergo hydrogen fusion at a faster rate than those with lower mass. As the core H gets exhausted, stars begin to leave the MS onto the *sub-giant branch (SGB)*, and the point of transition is called the *main sequence turn-off (MSTO)* point. The MSTO is used as an indicator of the age of the stellar system. Due to the inverse relationship between the star's initial mass and its lifetime on the MS, the masses of stars on the MSTO decrease as the cluster ages. For GGCs, the MSTO mass is $\sim 0.8\ M_\odot$ which implies that stars below this mass are still on the MS. Hence, the discussion further is limited to low-mass stars having masses $\lesssim 2\ M_\odot$. Here, a key point to be noted is that higher-mass stars in GGCs have already ended up as dead remnants, namely white dwarfs, neutron stars, or black holes.

Fig. 1.3 depicts the Hertzsprung-Russell (H-R) diagram showing the theoretical evolutionary sequence of a low-mass star with M = $0.862\ M_\odot$, He mass fraction $Y = 0.23$, and mass fraction of metals, Z = 0.0015 from Catelan (2013).

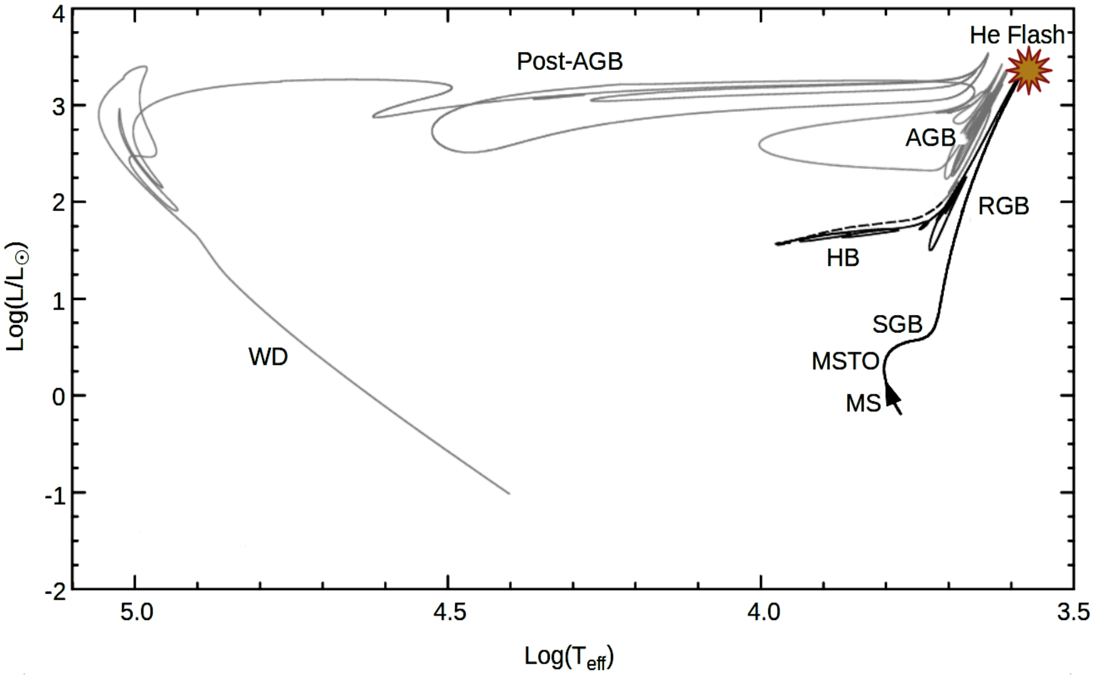

FIGURE 1.3: H-R diagram showing the evolutionary sequence of a star with M = $0.862\ M_\odot$, $Y = 0.23$, and $Z = 0.0015$ from Catelan (2013) based on the calculations by Brown et al. (2001).

On the SGB, H fuses in a shell around the inert He core with the occurrence of core contraction owing to gravity and envelope expansion due to radiation pressure. Stars then further progress onto the *red giant branch (RGB)* phase where a degenerate He core develops while the shell burning of H and envelop expansion continue. As stars reach the end of the RGB phase, depending on the initial mass, the degeneracy of the He-core is lifted with the runaway ignition of He in a process called the *helium flash* (Mestel 1952; Schwarzschild & Härm 1962). He flash occurs in stars with initial masses $\lesssim 2.2\ M_\odot$ when the temperature of the degenerate core reaches the He fusion temperature of $\sim 10^8$ K (Shu 1982).

Following the He flash, stars start fusing He in the core to form carbon and/or oxygen, surrounded by an H-burning shell. The locus of stars with varying masses that have just begun core-He fusion is called the *zero-age horizontal branch (ZAHB)*, which is generally known as *horizontal branch (HB)*. A star's location in this stage of the theoretical H-R diagram is determined by several factors, including its starting mass, chemical makeup, and the amount of envelope mass it lost on the RGB. This is illustrated in Fig. 1.4 where Star A has experienced more mass-loss on the RGB compared to Star B. Thus, on the HB, Star A has a higher effective temperature (T_{eff}) with respect to Star B. Although stars end up having slightly different envelope masses at this stage, their core mass remains nearly the same ($\sim 0.5\ M_\odot$), resulting in a horizontal sequence with nearly constant luminosity on the H-R diagram, leading to the name HB. However, on the optical CMD in Fig. 1.2, it can be observed that the HB droops as the stars become hotter. This is because, at $T_{\text{eff}} \gtrsim 10\,000\,\text{K}$, the $B-V$ color becomes less sensitive to temperature, and bolometric corrections increase.

The evolution of stars post the HB phase depends on the amount of envelope mass on the HB (Dorman et al. 1993, 1995), the details of which will be discussed in Section 1.3.2. In the case shown in Fig. 1.3, after core-He exhaustion, the inert core made of carbon (C) and/or oxygen (O) begins contracting, and He ignites in a shell around it. The He-burning shell is surrounded by a thin, almost inactive H-burning shell. The star is now said to be in the *asymptotic giant branch (AGB)* stage as it asymptotically approaches the RGB phase. The AGB may be divided into two distinct phases: (i) the *early-AGB (E-AGB)*, which continues until hydrogen is ignited with full efficiency in a shell around the He-burning shell, and (ii) the *thermally pulsing AGB, also known as the TP-AGB*, which lasts until

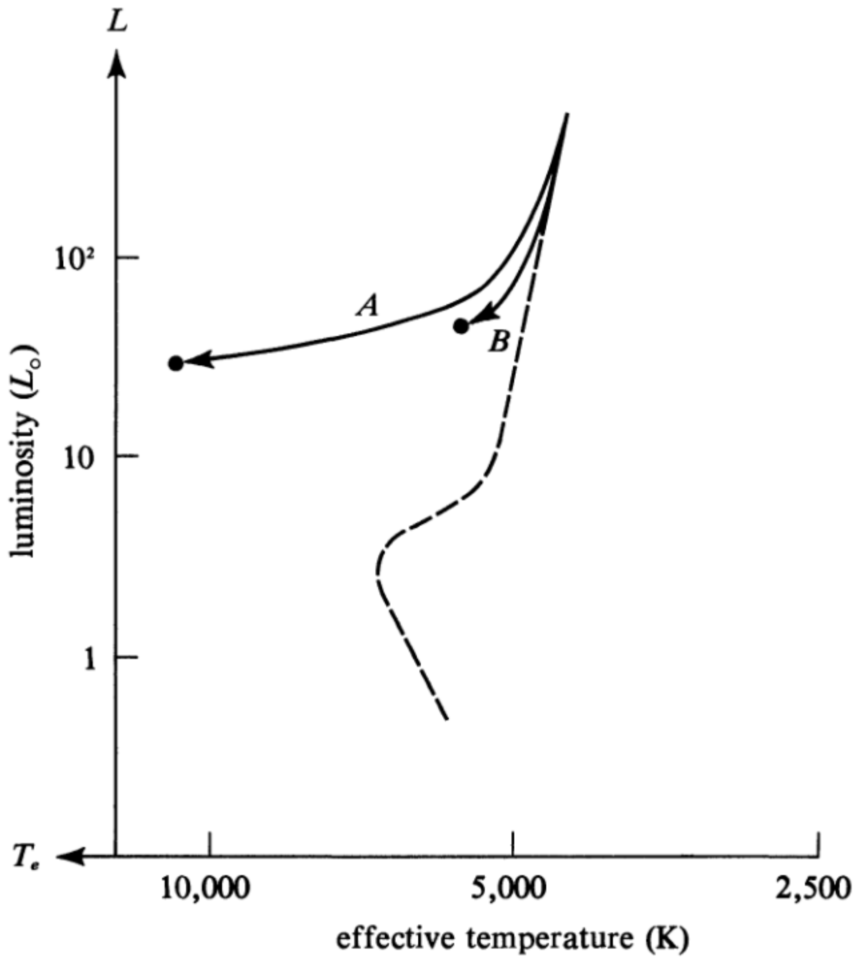

FIGURE 1.4: H-R diagram depicting the positions of population II stars after the He flash, having suffered different amounts of mass-loss on the RGB. Sequence A corresponds to a star that has lost relatively more envelope mass compared to that of sequence B. (Image Credits: Shu 1982, adapted from Iben 1967).

the majority of the hydrogen-rich envelope is swept away due to stellar wind. In the TP-AGB phase, a series of *thermal instabilities or pulses* occur due to a form of duet between the He-burning shell and the surrounding H-burning shell (Schwarzschild & Härm 1965). The H-burning shell remains the more important energy source in the star 90% of the time. However, it is occasionally quenched by the bouts of activity from the He-burning shell. In stars with sufficiently high core mass ($\gtrsim 0.7$ M$_\odot$) and total mass (> 2 M$_\odot$), during the TP-AGB phase, the envelope convection zone moves inwards and merges with the inner convection zone. This brings the products of helium fusion, i.e., carbon-rich material, along with s-process elements to the surface of the AGB star, and the process is called *third dredge-up* (See the review by Iben & Renzini 1983). During the TP-AGB phase, a substantial amount of envelope mass is lost. Eventually, all the outer layers are ejected, exposing the hot core of the progenitor AGB star. At this point, the star is said to be in the *post-AGB (pAGB)* phase. The pAGB star further evolves quickly at high luminosities towards hotter effective temperatures and finally settles on the *white dwarf (WD)* cooling track. In canonical models, the luminosity of WDs is solely attributed to the residual thermal radiation as the thermonuclear reactions cease, and they gradually cool down, becoming dimmer (See the detailed review by Iben 1991).

The next section focuses on the details of GC stars that are hotter than $\sim 5500\,\mathrm{K}$, depicted using shades of blue in Fig. 1.2.

1.3 Hot Stellar Populations in GCs

In general, it may be a little perplexing to find hot stars in old stellar systems like GGCs because hot stars are often related to young stellar systems. However, GGCs have been known to host hot stars for a long time (Moehler 2001, and references therein). The term "hot stars" in this context refers to stars with $T_{\mathrm{eff}} \gtrsim 5500\,\mathrm{K}$, which can be significantly bright in the blue and ultra-violet (UV) wavelength regimes. In GCs, hot stars exist in various advanced evolutionary phases like HB, post-HB (pHB), and WD, as well as non-canonical phases such as blue straggler (BS). These phases are discussed in depth in the next few subsections.

1.3.1 Horizontal Branch Stars

Fig. 1.5 shows the schematic structure of an HB star. It consists of a He-fusing core, a shell undergoing hydrogen fusion, and a radiative, hydrogen-rich envelope.

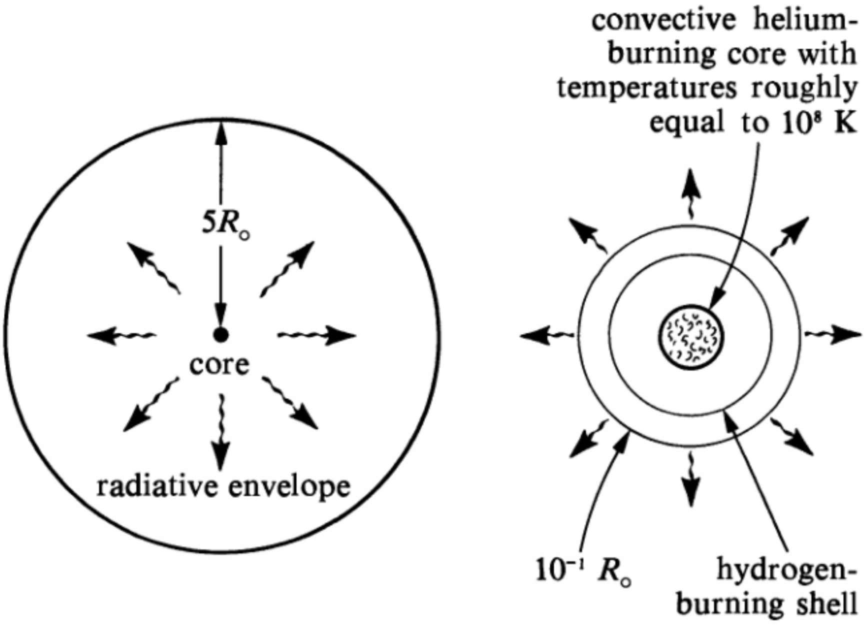

FIGURE 1.5: The schematic structure of an HB star. *Left*: Entire star from core to the surface layer. *Right*: Enlarged image of the region close to the He-burning core. (Image Credits: Shu 1982)

On GC CMDs, HB stars exhibit an extended range in color. In the 1960s, it was suggested that the morphology of the HB is primarily influenced by the cluster metallicity, the so-called *first parameter* (Sandage & Wallerstein 1960). It was found that metal-rich GCs ([Fe/H] > -0.8 dex) had redder HBs, and metal-poor ones had pronounced blue HB populations. However, the studies by Sandage & Wildey (1967) and van den Bergh (1967) demonstrated that some GGCs with the same metallicity have different HB morphologies. As a result, it became apparent that a factor other than metallicity affects the color distribution of HB stars. This issue is commonly referred to as the *second parameter problem*. Several parameters were proposed, including the initial He fraction (Y_{ini}; van den Bergh 1967; Sandage & Wildey 1967), mass of the GGC (e.g., Recio-Blanco et al. 2006), age of the GGC (e.g., Searle & Zinn 1978) and so on (See also Catelan 2009; Gratton et al. 2010; Milone et al. 2014 and references therein).

At a given metallicity, the color distribution of the HB on the CMD is a function of the stars' envelope mass, which in turn is influenced by the mass-loss on the RGB phase (Iben & Rood 1970; Rood 1973). The less massive the envelope is, the hotter the resulting star will be. The HB is thus made up of various sub-populations having similar core masses ($\sim 0.5\ M_\odot$) but with different envelope masses. These include the following groups in the increasing order of $T_{\rm eff}$ as shown in Fig. 1.6:

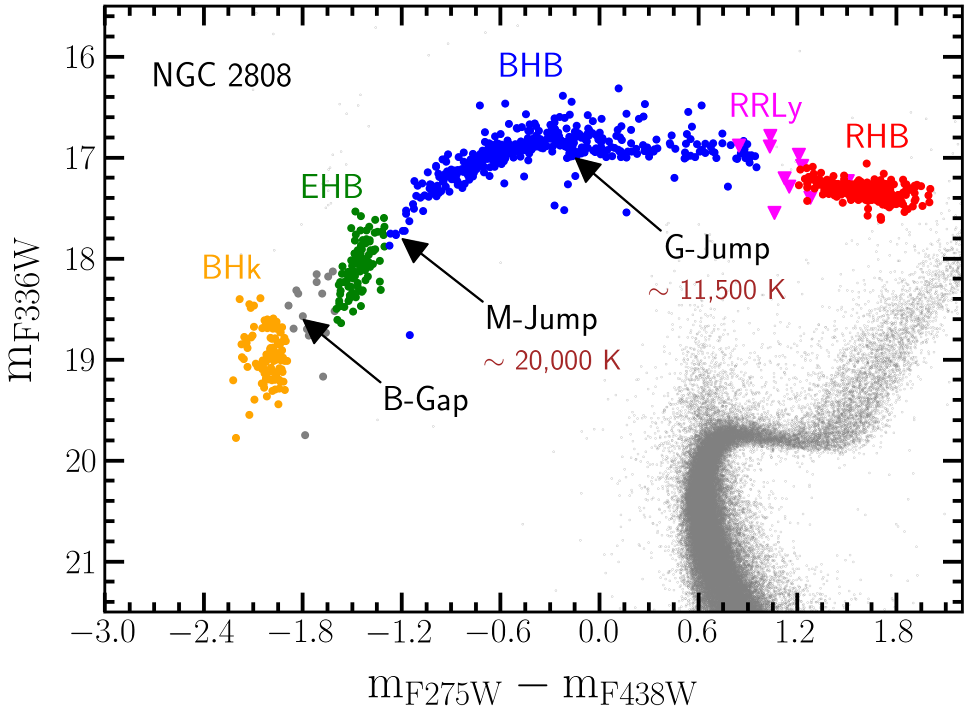

FIGURE 1.6: The UV-optical CMD of NGC 2808 showing the extended HB where stars are categorized into RHB, BHB, EHB, and BHk populations using the *Hubble Space Telescope* UV Globular Cluster Survey (HUGS; Piotto et al. 2015; Nardiello et al. 2018) dataset. The RRLy stars are also shown. The notable photometric discontinuities, such as the Grundahl jump (G-jump), the Momany jump (M-jump), and the gap between EHB and BHk stars (B-gap), are also marked.

(i) *red HB (RHB)* - stars lying at the red (cool) end of the HB, spanning temperatures from $\sim$ 5500 to 6200 K.

(ii) *RR Lyrae (RRLy) variables* - pulsating stars lying in the region where the HB meets the instability strip. These have pulsation periods ranging from 0.2 to 1.2 days (Smith 1995).

(ii) *blue HB (BHB)* - These stars lie on the hot end of the RRLy instability strip and have $T_{\rm eff}$ in the range 8000-20 000 K.

(iii) *extreme HB (EHB)* - These stars have extremely thin radiative envelopes ($\lesssim$ 0.02 $M_{\odot}$), having undergone significant mass-loss on the RGB and T_{eff} ranging from $\sim$ 21 000 to 30 000 K. Their counterparts in the Galactic field are sub-dwarf B-type (sdB) stars (Caloi et al. 1982).

(iv) *blue hook (BHk)* stars - These are the hottest HB stars with $T_{\rm eff}$ > 32 000 K and faintest in the optical regime. They are named after their location in far-UV (FUV) CMDs where they take the shape of a *hook* on the hot side of the HB (Whitney et al. 1998), appearing fainter than canonical EHB stars (D'Cruz et al. 1996, 2000; Brown et al. 2001).

The CMD in Fig. 1.6 also shows the important photometric discontinuities along the HB, namely the the Grundahl jump (G-jump; Grundahl et al. 1998, 1999) at $\sim$ 11 500 K; the jump at $\sim$ 20 000 K discovered by Momany et al. (2002, 2004), known as the Momany jump or M-jump; and the gap between the EHB and the BHk stars – B-gap (Brown et al. 2016). These discontinuities are attributed to the effects in stellar atmospheres, such as atomic diffusion and gravitational settling, operating at specific temperatures.

One of the open problems in understanding HB stars is the mechanism leading to the origin of the EHB and BHk populations. The two main propositions of BHk formation are as follows:

(i) *late hot flasher (LHF)* scenario, where due to the extreme amount of mass-loss in the RGB phase, the He-flash occurs in the star only as it descends the WD cooling track. Due to the delayed He-flash, the thin H-rich envelope gets mixed with the He-burning core, resulting in the enhancement of He (∼ 96% by mass) and carbon (∼ 4% by mass) in the star's atmosphere (e.g., Castellani & Castellani 1993; Brown et al. 2001). In another scenario, named the *early hot-flasher (EHF)*, the He-flash takes place when the star evolves at a constant luminosity after leaving the RGB. However, this case does not result in envelope mixing and produces EHB stars with standard surface composition. Fig. 1.7 adapted from Brown et al. (2010a) depicts the evolutionary pathways described above ((b) and (c)) along with the canonical pathway of RGB tip flash (a).

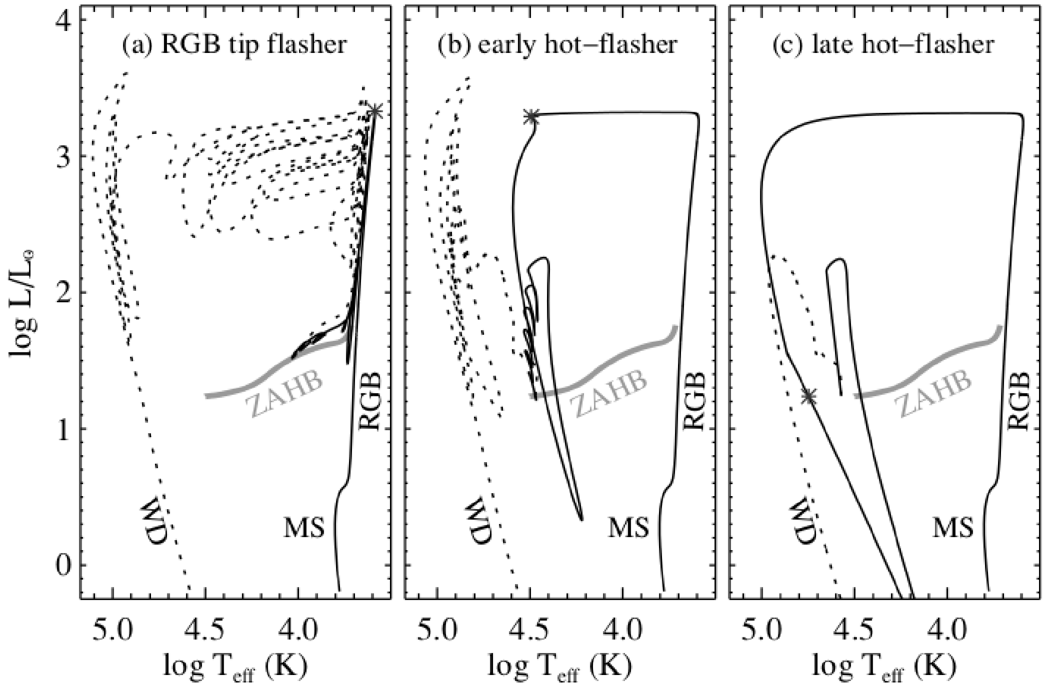

FIGURE 1.7: Various scenarios for the evolution of an HB star depending on the location of the He-flash (Adapted from Brown et al. 2010a).

(ii) *He self-enrichment* scenario, where the He-enhanced ($Y \sim 0.4$), second generation sub-populations in the cluster evolve to form BHk stars (Lee et al. 2005; D'Antona et al. 2010). He-enhanced HB stars will have lower masses than typical HB stars with the same age and metallicity, leading to bluer and fainter ZAHB locations (Chung et al. 2017).

One important point to be noted is that the mechanism causing large mass-loss on the RGB is unknown.

1.3.2 Post-Horizontal Branch Stars

According to canonical stellar evolution models, the post-helium-core-burning (pHeCB) or pHB evolution of a star depends strongly on its envelope mass (Dorman et al. 1993, 1995). Following He depletion in the core, the HB stars with the largest envelope masses begin the AGB phase, undergo thermal pulsations, and ultimately lose their envelopes to become extremely hot stars with constant luminosity. Known as pAGB stars, these are short-lived (lifetime $< 10^5$ years) with luminosity, $log\ (L/L_{\odot}) \geq 3.1$. The HB stars with slightly lower envelope masses (> 0.02 M$_{\odot}$) ascend the AGB but do not undergo thermal pulsations or third dredge-up in this phase. They eventually lose their envelopes and evolve towards higher temperatures with slightly lower luminosities ($log\ (L/L_{\odot}) \sim 2.65$ to 3.1) than the pAGB stars. These are known as post-early-AGB (peAGB) stars (Brocato et al. 1990) and have a lifetime of $\simeq 10^5$ years. After core-He exhaustion, HB stars with the lowest envelope masses are unable to ascend the AGB and instead migrate directly onto the WD cooling curve with a slight enhancement in luminosity. These are referred to as AGB-manqué stars (Greggio & Renzini 1990). The range of their luminosities is $log\ (L/L_{\odot}) \sim 1.8$ to 2.65, with lifetimes of 20 to 40 Myr (Moehler et al. 2019). Fig. 1.8 depicts the schematic H-R diagram from Dorman et al. (1993) along with the various pHB evolutionary scenarios.

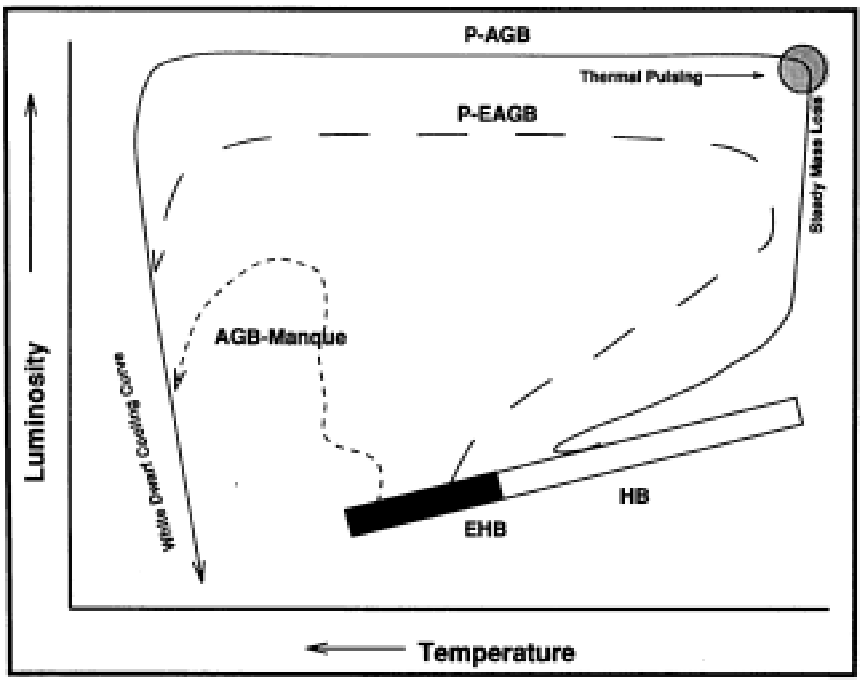

FIGURE 1.8: A schematic H-R diagram with the various pHB evolutionary scenarios from Dorman et al. (1993).

In the UV images of GGCs, a couple of luminous pHeCB stars in different evolutionary phases may be seen. Zinn et al. (1972) referred to them as *UV-bright stars* and were looked for as stars whose *U*-band magnitudes were brighter than that of any other star in the GGC. These were identified using short, alternate exposures of *U* and *V* photographic plates, leading to the name *UV-bright stars.* Since these searches were based on optical observations, they were biased towards the most luminous pAGB stars and were unable to detect the less luminous peAGB and AGB-manqué stars (Moehler 2001). Moreover, most of the stars detected were cooler than 30 000 K, although there were theoretical predictions of even hotter pAGB stars. The crowded cores of GGCs posed yet another difficulty for ground-based optical observations. Thus, the census of pHB stars in GGCs remains largely incomplete.

1.3.3 White Dwarfs

WDs represent the ultimate stage of evolution for $\sim$ 98% of all the stars (Kalirai et al. 2009). Investigation of WDs offers a wealth of knowledge on the physical characteristics and evolution of their progenitors (See Moehler & Bono 2008 for an excellent review). Canonical single-stellar evolutionary theory suggests that the masses of CO core WDs in GGCs should be within the range 0.51 to 0.55 $\mathrm{M}_{\odot}$ (Kalirai et al. 2009, and references therein). However, WDs of smaller masses and different core compositions (e.g., He-core) may be produced in GGCs from alternate evolutionary pathways. WDs with cores composed of He, having masses in the range 0.1 to 0.4 $M_{\odot}$, can result from the evolution of compact binaries with neutron star/millisecond pulsar companions (e.g., Cadelano et al. 2019, 2020; Chen et al. 2023). It was shown theoretically by Althaus et al. (2017) that He-core WDs with masses in the range 0.44 to 0.46 $M_{\odot}$ can form from He-enhanced ($Y \sim 0.4$), metal-poor (Z = 0.001) progenitors with initial masses less than 0.65 $M_{\odot}$ as they do not undergo He-flash.

WDs are widely employed as chronometers to estimate the ages of various Galactic populations like OpCs, GGCs, and so on. This is because their evolution is canonically regarded to be pure cooling due to radiation of residual thermal energy. However, recent observations of WD sequences in two GGCs (M13 and NGC 6752) have revealed a surplus of luminous WDs that cannot be explained with the standard WD evolutionary models (e.g., Chen et al. 2021, 2022). According to these studies, the excess is created by the slowdown of the cooling mechanism in 70% of the WDs in these clusters, which is driven by steady thermonuclear burning in their remaining H-rich envelope. These *slowly-cooling WDs* are the evolutionary products of stars with ZAHB mass $\lesssim 0.56$ $\mathrm{M}_{\odot}$ that do not undergo third dredge-up (peAGB stars) and thus have sufficiently thick H envelope remaining. These newly discovered slow WD populations have significant consequences regarding the way WDs should be used to age-date stellar populations.

Observations of WD sequences and their characterization in a large number of GGCs are the need of the hour to shed more light on the physics behind such non-standard evolutionary scenarios.

1.3.4 Blue Straggler Stars

Fig. 1.2 shows a few stars located brighter than the MSTO, appearing like an extension of the MS, towards bluer colors. According to standard single-stellar evolutionary theory, in old stellar systems like GGCs, all the massive stars above the MSTO should have evolved. Yet, such apparently massive, younger/rejuvenated stars are found in almost all GGCs. Sandage (1953) first identified such objects in the outskirts of the GGC, M3, and later in the OpCs, M67 (Johnson & Sandage 1955) and NGC 7789 (Burbidge & Sandage 1958). They were named *blue straggler stars* (*BSSs*; Burbidge & Sandage 1958) as they had bluer colors and appeared to "straggle" or trail behind in evolutionary rate compared to their counterparts in the cluster. BSSs remained elusive in GGCs until the study of M71 by Arp & Hartwick (1971). Later, observations using Charge-Coupled Devices (CCDs) as back-end instruments on ground-based telescopes and the *Hubble Space Telescope (HST)*, BSSs were found to exist even in the dense cores of GCs (See the review by Bailyn 1995).

The full details regarding the formation of BSSs in different environments are still an open puzzle. The location of BSSs on CMDs suggests them to be more massive than their counterparts in the cluster. Thus, the genesis of the BSSs should be sought in processes capable of enhancing the initial mass of the stars in some kind of revitalization process. Three main such theories are as follows: (i) Hills & Day (1976) proposed that, in high-density environments, collisions among stars inducing mergers can produce BSSs, (ii) McCrea (1964) and Zinn & Searle (1976) proposed that the process of mass transfer (MT) between binary stars, possibly up to the extent of coalescence, can result in BSSs, (iii) Perets & Fabrycky (2009) and Naoz & Fabrycky (2014) proposed that BSSs can form in hierarchical triple systems when the inner binaries tighten and merge. The MT and triple scenarios are preferred in low-density environments like the outskirts of GGCs, where binaries/triples have higher survival probabilities. Depending upon the type of donor in the binary system, MT can result in BSSs with either He-core or CO-core WD companions. Thus, BSSs undoubtedly serve as an avenue to explore the link between non-standard stellar evolution and the dynamics of the cluster.

BSSs, being more massive than other cluster members (with M $\sim$ 1.2-1.3 $M_{\odot}$), are affected significantly by dynamical friction, which makes them segregate near the central regions of the GGC. Thus, the radial trend of the spatial distribution of BSSs can be used to infer the dynamical evolutionary status of the cluster (Boffin & G. 2015, and references therein).

BSSs also cross the instability strip in the H-R diagram, thereby becoming pulsating variables called *SX Phoenicis (SX Phe)* variables that have periods in the range of $\sim$ 0.01 to 0.1 days (Ngeow et al. 2023, and references therein). The pulsation properties of SX Phe variables can be employed to derive BSS masses (e.g., Fiorentino et al. 2015). Independent estimates of the cluster distance can be derived from the period-luminosity relations of these variables (e.g., Cohen & Sarajedini 2012; Arellano Ferro et al. 2018).

1.4 Importance of Probing Hot Stars in GGCs

Investigation of hot stars in GGCs can contribute to many aspects, as outlined in the following paragraphs.

Understanding the late stages of low-mass stars – The late evolutionary stages of low-mass stars, starting from the pHB phase, are some of the least understood phases in low-mass stellar evolution. This is because of the uncertainties in the estimates of CO core size (Charpinet et al. 2011; Constantino et al. 2015) and stellar winds in the RGB phase, which determine the envelope mass of HB stars (McDonald & Zijlstra 2015; Salaris et al. 2016). Due to the lack of suitable observations, the census of stars in these quickly evolving stages is incomplete. Thus, the existing pHB models have not been tested extensively and have scope for improvement.

UV-upturn in elliptical galaxies – In a broader context, the EHB stars and their progeny, AGB-manqué stars, are considered strong candidates to explain the *UV-upturn* seen in elliptical galaxies' spectra (Dorman et al. 1995; Greggio & Renzini 1999, and references therein). It is interesting to note the hypothesis that extreme helium abundance ($Y \sim 0.4$) plays a common role in the origin of both EHB stars in GGCs and the *UV-upturn* phenomenon (Yi et al. 2011). The *UV-upturn* phenomenon has also been found to be strongly correlated with the Mg_2 absorption line feature, which is a measure of the metallicity of old stellar populations (Burstein et al. 1988). GGCs thus constitute excellent local analogs to investigate the properties of EHB stars and their progeny, which can help in accurately determining their contribution to the UV luminosities of other old stellar systems. Investigating GGCs covering a range of values in metallicity and helium abundance can also give clues on the role of these parameters in the *UV-upturn* phenomenon.

Multiple Stellar Populations (MSP) – The astronomical community widely believes that GGCs are formed from two generations of stars: a *first generation (FG)*, whose composition resembles that of halo field stars, and a *second generation (SG)*, wherein stars are enhanced in elements such as nitrogen, sodium, helium, and depleted in carbon and oxygen. Although several scenarios have been proposed in the literature to explain the origin of MSPs, this is still an unsolved problem. All of these hypotheses rely on the presence of a source to "pollute" the pristine material from which the SG stars take shape. The leading scenarios predict that the SG stars form from the material polluted by (i) intermediate-mass AGB stars, (ii) fast-rotating massive stars, (iii) massive interacting binary stars, or (iv) supermassive stars (See the reviews by Bastian & Lardo 2018; Milone & Marino 2022). The photometric signatures of MSPs include multiple sequences in the CMD along different evolutionary phases such as MS, SGB, RGB, WD, etc., and extended HB morphologies (See Fig. 1.6). The presence of sub-populations enhanced in He abundance results in blue HB tails. Another example is shown in Fig. 1.9, where the split sequences along the MSTO and WD cooling track in the CMD of GGC, Omega Centauri, are depicted. Thus, by investigating hot HB stars and their progeny, specific insights can be gained into the MSP phenomenon, especially in terms of He-enhancement.

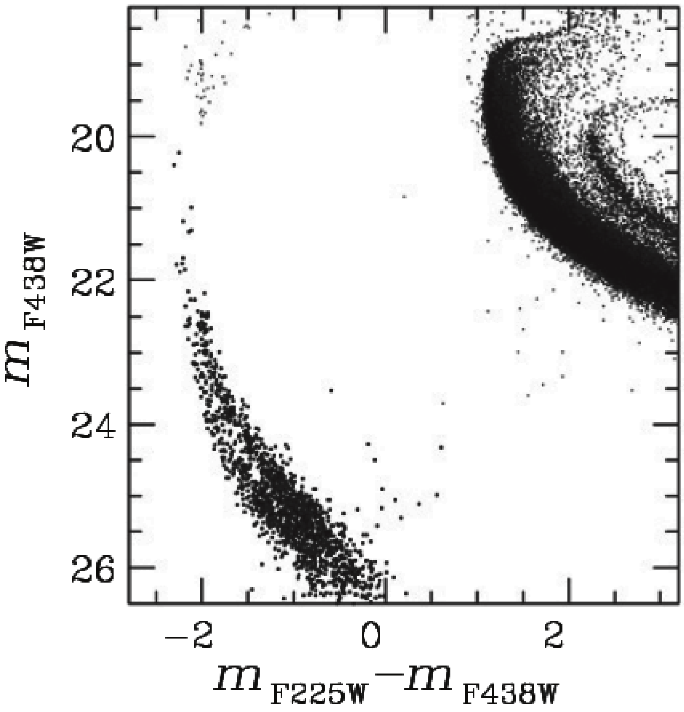

Figure 1.9: The UV-optical CMD based on *HST* data depicting the multiple MSTO sequences and the two WD sequences in the GC Omega Centauri (Adapted from Bellini et al. 2013).

Origin of stellar exotica – The detection and characterization of stellar exotica, such as BSSs, are important to understand how stellar dynamics in clusters influence stellar evolution. There is growing evidence for the fact that dynamical processes in GGCs, such as core-collapse, can be traced from the morphology of BSSs in CMDs, such as the presence of double sequences (e.g., Ferraro et al. 2009; Cadelano et al. 2022). Thus, it is crucial to investigate BSSs in more GGCs, particularly those that have undergone core collapse. Another interesting aspect is to understand binary evolution and the MT scenario by characterizing BSSs with hot companions using multi-wavelength photometric observations.

1.5 Need for UV Observations

The black body continua of hot stars described in Section 1.3 peak at blue and UV regimes. Thus, observations in the UV are crucial to detect and characterize hot stars in GGCs, especially in the dense central regions. UV study also helps to suppress the contribution from cooler stellar populations such as MS and RGB stars and produce images with reduced stellar crowding. Fig. 1.10 shows the optical and FUV images of the GC NGC 6341 downloaded from the STScI MAST archive*. It can be clearly observed that the FUV image has far less number of stars compared to the optical image.

Fig. 1.11 shows schematic GGC CMDs in the optical and UV-optical planes. It can be observed that the sequences of hot stars turn brighter and span a larger range in magnitudes while going from the optical to the UV-optical plane.

UV observations are also important to study the effect of He-enrichment in hot HB stars. The top panel of Fig. 1.12 shows the theoretical spectral energy distributions

---

*https://mast.stsci.edu/portal/Mashup/Clients/Mast/Portal.html

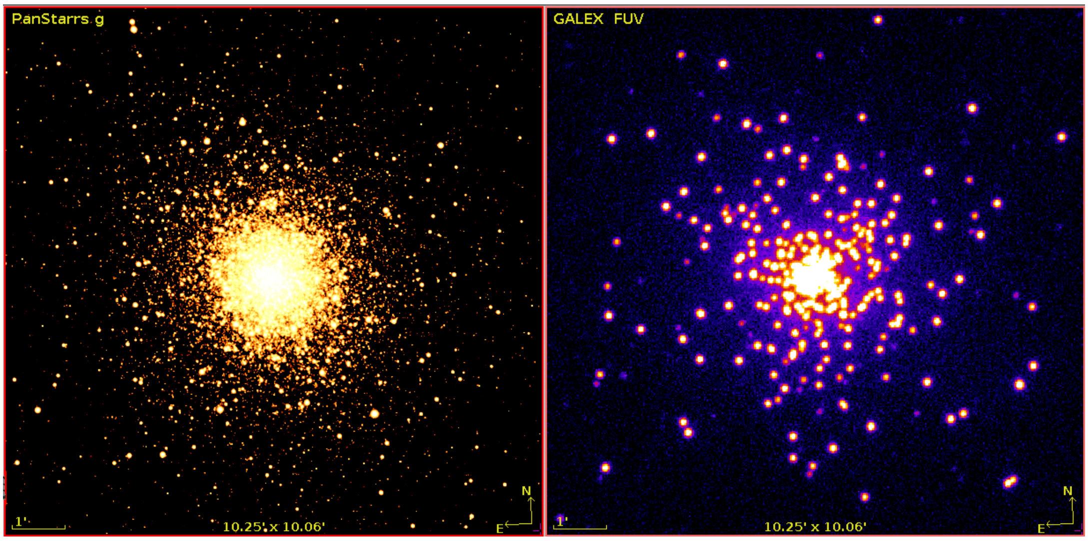

FIGURE 1.10: Images of NGC 6341 from the STScI MAST archive. *Left*: Pan-STARRS g band image, *Right*: *GALEX* FUV image.

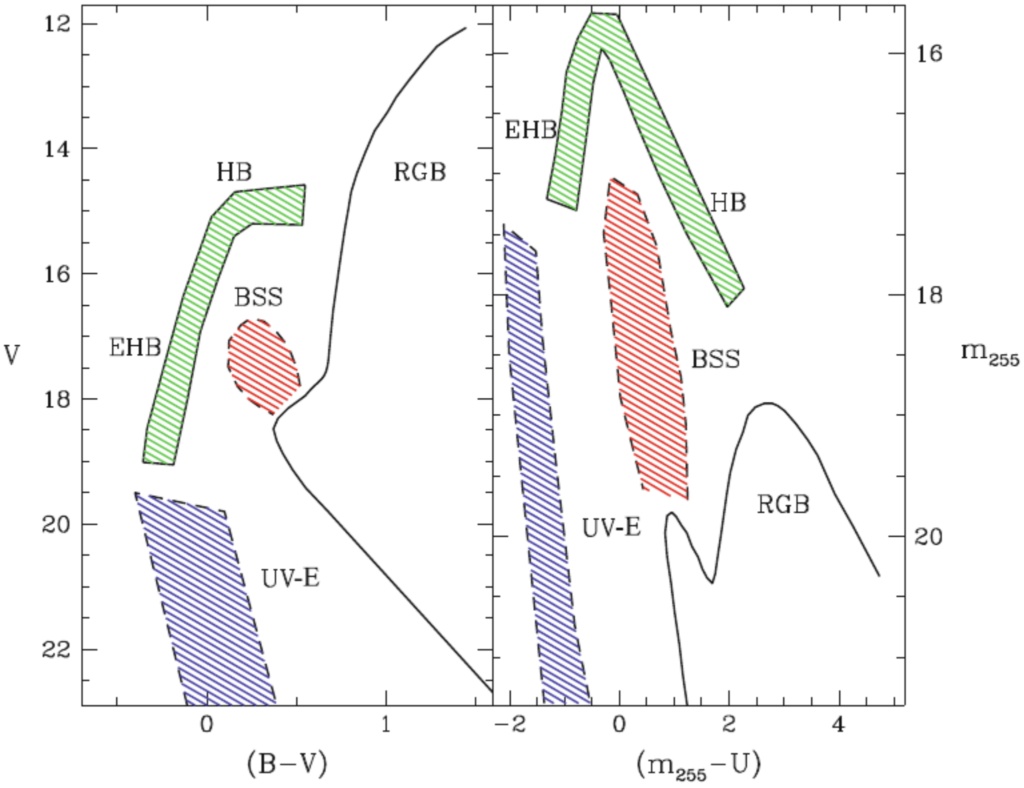

FIGURE 1.11: Schematic GC CMDs. *Left* - optical CMD and *Right* - UV-optical CMD (Modified version of the figure from Ferraro et al. 1999).

(SEDs) of three BHB stars with the same metallicity ([Fe/H] $= -1.5$ dex) and age (13 Gyr) but different Y values from Sahu et al. (2022) based on the models from

Chung et al. (2017). In the bottom panel are the transmission windows of filters from various UV missions. It is evident that the SEDs deviate considerably at wavelengths shorter than 2000 Å, highlighting the importance of UV investigation.

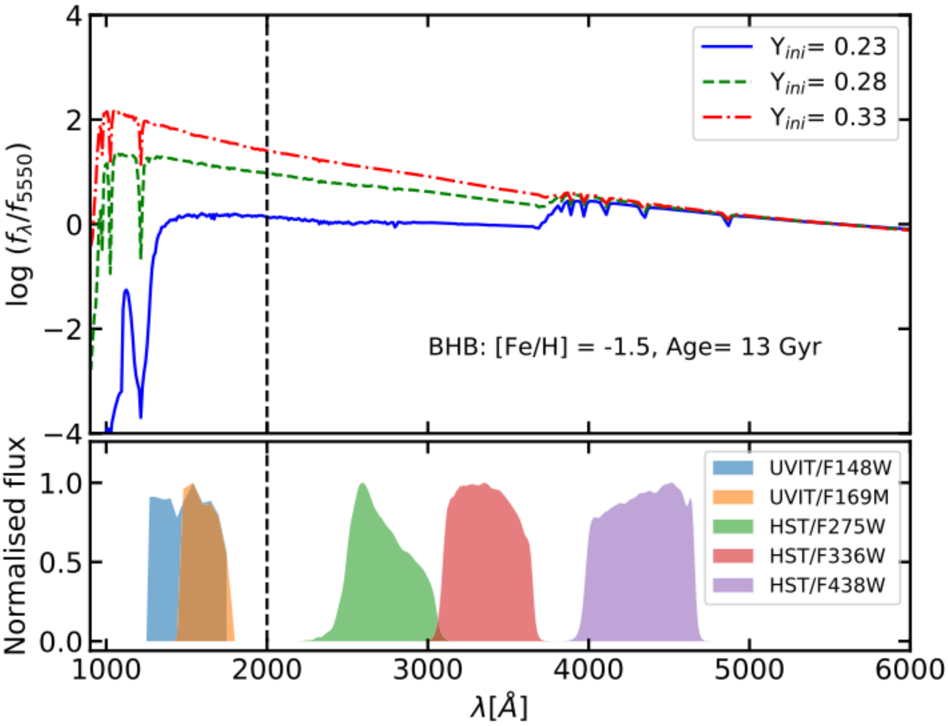

FIGURE 1.12: Theoretical SEDs of BHB stars with the same metallicity ([Fe/H] $= -1.5$ dex) and age (13 Gyr) but different Y values (Adapted from Sahu et al. (2022) based on the models from Chung et al. (2017)).

1.6 Thesis Goals

The main aim of this dissertation is to carry out the census of hot stars in GGCs and characterize them in order to:

1. Shed light on the late stages of low-mass stars' evolution
2. Identify the formation mechanisms of non-canonical stars and stellar exotica
3. Investigate the effects of stellar dynamics in clusters on stellar evolution

4. Trace MSP phenomenon in GGCs and probe their origin

To achieve these aims, a multi-wavelength study of hot stars in three GGCs is carried out. Out of these, two clusters, NGC 2808 and NGC 5139 (also known as Omega Centauri), are massive and dense. Both these clusters have a wide color distribution of HB stars, including a significant population of EHB stars and pHB stars. These GGCs are also known to host highly complex MSPs with populations significantly enhanced in He ($Y \sim 0.4$). The third cluster is NGC 6397, a low-mass, nearby core-collapsed cluster, ideal for understanding the properties of exotic sources bright in the UV regime. The primary dataset comes from the Ultra Violet Imaging Telescope (UVIT) onboard the Indian space observatory, *AstroSat*. UVIT gives a spatial resolution of ~ 1.2", has a moderate field of view (FOV), and has multiple filters in FUV and NUV wavebands. In order to identify the optical counterparts of the UV sources, catalog-based datasets from the *HST*, *Gaia*, and ground-based telescopes are used.

1.7 Thesis Overview

Chapter 1 gives an introduction to GGCs, the hot stars in GGCs that exist in the late evolutionary phases of low-mass stars (HB, pHB, and WDs) and those that are formed through non-canonical pathways (BSSs). The chapter also outlines the motivation and objectives of this dissertation.

Chapter 2 presents an overview of the datasets used in the thesis and the general methodologies adopted for the reduction of data and analysis.

Chapter 3 describes the first complete census of the pHB member stars in the massive and dense GGC NGC 2808 carried out using UV observations, their physical properties derived utilizing multi-wavelength photometric datasets, and their evolutionary status inferred using available theoretical models.

Chapter 4 deals with the UV properties of the newly discovered variable EHB stars in NGC 2808.

Chapter 5 presents the important findings from the first comprehensive FUV photometric investigation of the most massive and complex GGC system, ω Centauri, going into the details of its peculiar HB and WD populations and the MSPs along the HB.

Chapter 6 reports the census and characterization of the FUV-bright stellar populations of the nearby, core-collapsed GGC, NGC 6397.

Chapter 7 sums up the major findings of the thesis, presents the conclusions, and gives a glimpse into the future directions.

Chapter 2

Data and Methodology

2.1 Introduction

The study of hot stellar populations in GCs is best accomplished using observations in the UV regime as their black body continuum peaks at these short wavelengths. These observations, when complemented with archival datasets in other wavebands such as optical/near-infrared (NIR), will help to characterize the stellar populations and identify cooler binary companions, if any. In this thesis, I have utilized the UV observations from *AstroSat*/UVIT supplemented with cataloged data from space missions such as *HST*, *Gaia*, and several ground-based telescopes. The following section provides a detailed overview of the UVIT instrument and the procedures adopted to reduce the data and analyze the images. The complementary archival datasets used are described in Section 2.3. The methodology employed to characterize the stellar populations is discussed in Section 2.4.

2.2 AstroSat/UVIT

Astrophysical sources can be observed using telescopes on the ground only within certain windows, including the optical, NIR, and radio regimes. Fig. 2.1 shows the relative transparency of the Earth's atmosphere as a function of the wavelength of electromagnetic radiation and the different atmospheric transmission windows. As evident from the figure, the Earth's atmosphere blocks off high-energy radiation, including X-rays and UV rays. Hence, space-based telescopes are crucial to study sources emitting such photons.

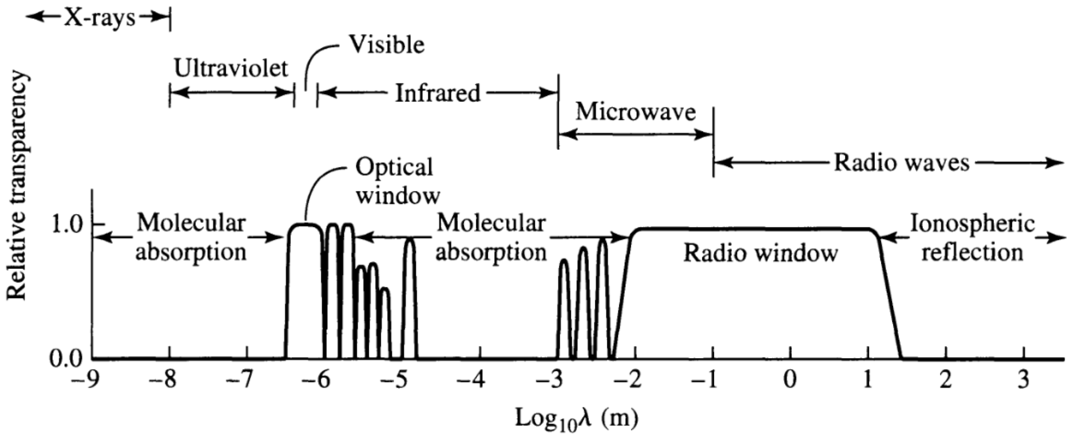

FIGURE 2.1: A plot showing the relative transparency of the Earth's atmosphere to electromagnetic radiations of different wavelengths. (Adapted from Carroll & Ostlie (2017))

India launched its first multi-wavelength space observatory, *AstroSat*, on 28th September 2015. The UVIT, primarily used for UV imaging, is one of the five scientific instruments onboard *AstroSat*. The other major payloads are used for X-ray observations and include a Soft X-ray Telescope (SXT), three Large Area X-ray Proportional Counters (LAXPCs), a Cadmium–Zinc–Telluride Imager (CZTI), and a Scanning Sky Monitor (SSM). *AstroSat* also carries a supplementary instrument known as the Charge Particle Monitor (CPM), which issues warnings to other instruments in case the spacecraft passes through regions with high flux of charged particles and monitors the entry and exit points of the South Atlantic

Anomaly. A schematic of *AstroSat* with all the scientific instruments is shown in Fig. 2.2, and a detailed review can be found in Singh (2022).

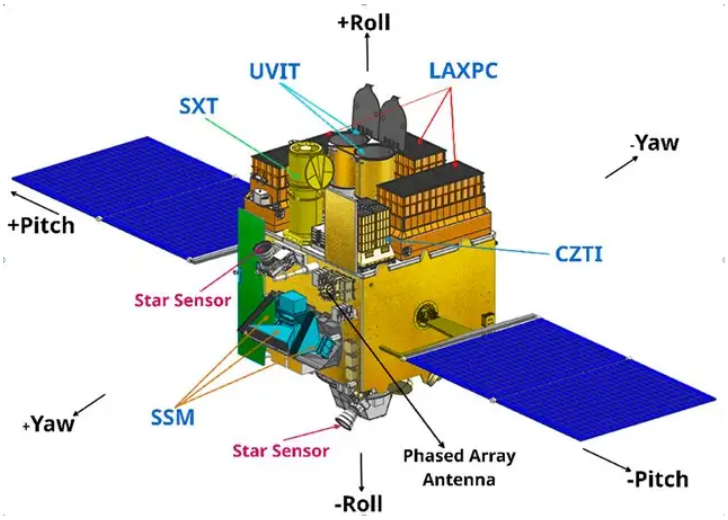

FIGURE 2.2: A representative image of the *AstroSat* observatory showing all the payloads. (Adapted from Singh (2022). Original credits: V. Girish, ISRO.)

The UVIT has two telescopes, each of length 3.1 m and diameter 0.87 m, in Ritchey–Chretien optical configuration with a focal length of 4.75 m and an aperture of $\sim$ 0.38 m. One telescope detects FUV photons covering the wavelength range from 130 nm to 180 nm, and another one observes simultaneously in the NUV and visible (VIS) covering wavelength ranges from 200 nm to 300 nm and 320 nm to 550 nm respectively (see the UVIT configuration in Fig. 2.3). A dichroic beam splitter is used in the NUV/VIS telescope, which reflects NUV and transmits VIS. The data from the VIS channel are primarily meant for correcting the spacecraft drift while creating science-ready images. Each passband has multiple filters allowing the advantage of observations in narrower wavelength ranges. Fig. 2.4 shows the effective areas of the FUV and NUV filters from Tandon et al. (2017, 2020). The FOV covered is circular with a diameter of 28′. Additional details regarding the instrument design can be found in Kumar et al. (2012). The information related to the instrument calibration are detailed in Tandon et al. (2017) and updated in Tandon et al. (2020).

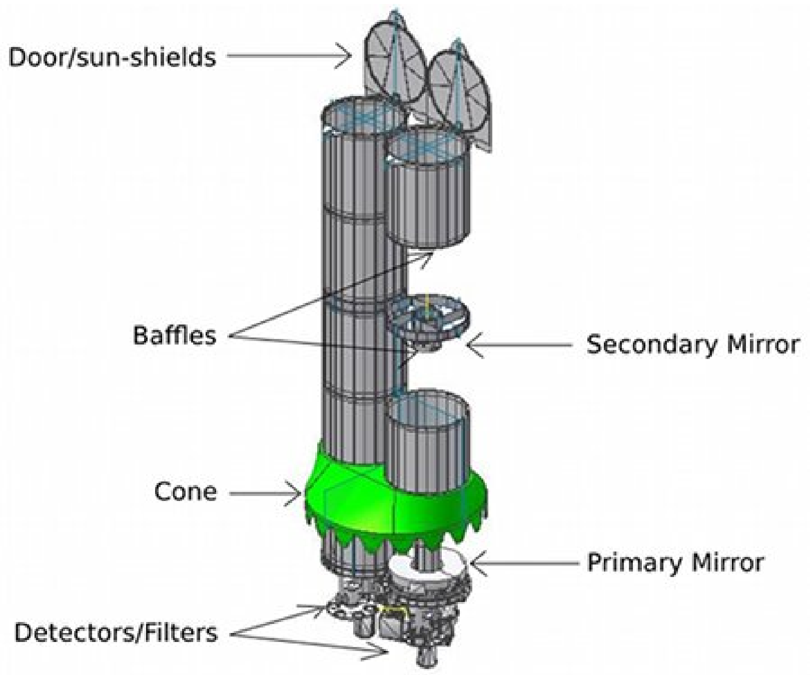

FIGURE 2.3: UVIT schematic (Adapted from Singh (2022). Original credits: UVIT teams at IIA and ISRO.)

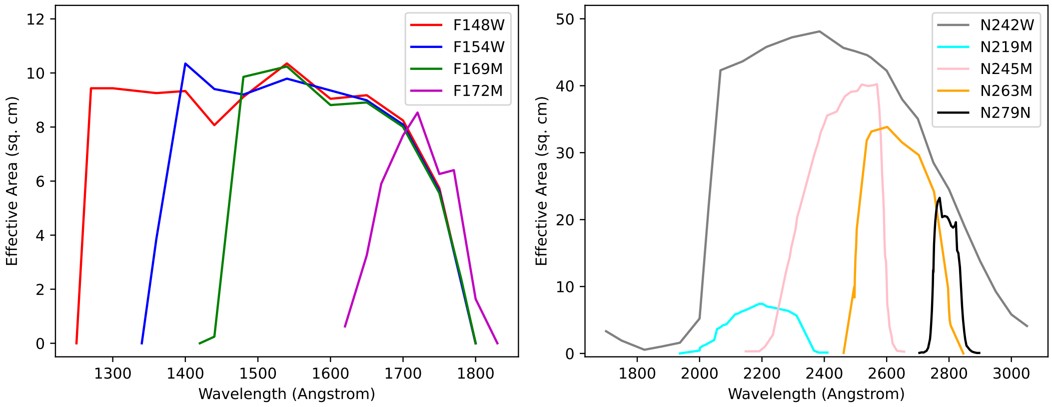

FIGURE 2.4: Effective areas for UVIT/FUV filters (left) and those for UVIT/NUV filters (right) from Tandon et al. (2017, 2020)

The UV (VIS) channel detectors operate in the photon-counting (integration) mode using intensified imagers (see Fig. 2.5) consisting of the following components : (i) an input window, (ii) a photocathode, (iii) two microchannel plates (MCPs), (iv) phosphor anode, (v) optical fiber taper, and (vi) a Complementary Metal Oxide Semiconductor (CMOS) sensor with 512 × 512 pixels. The FUV and NUV/VIS detectors are identical in most aspects except in the compositions of the input window and photocathode.

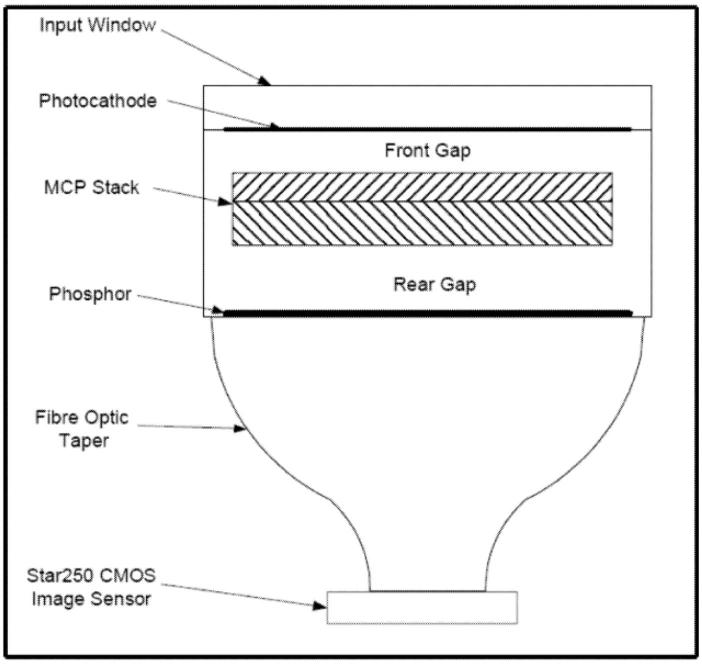

Figure 2.5: Detector system of UVIT - a sketch from Hutchings et al. (2007)

A photon entering through the input window onto the photocathode produces an electron that is accelerated across a gap of ∼100 μm towards the MCPs having a gain of 10^7. The MCPs generate a shower of electrons that are propelled again toward the phosphor anode, leading to its illumination. The emission from the anode is directed through the optical fiber taper to the CMOS sensor and covers several pixels on it (called an *event*). Each event is recognized, and the center of the shower is estimated to be about $1/8^{th}$ of a pixel in real-time as described in Hutchings et al. (2007) and Postma et al. (2011). One CMOS pixel maps to about $3.33''$ on the sky after the taper. However, the centroiding algorithm helps to achieve a spatial resolution better than $1.5''$. The CMOS array is read out at the rate of 29 frames/sec for the full field. Further details on the detector are described in Hutchings et al. (2007); Postma et al. (2011).

The Level 0 (L0) raw data from the satellite is transmitted to the ground station operated by the Indian Space Research Organization (ISRO). This, along with the satellite metadata, is then processed into Flexible Image Transport System (FITS) table format and is called Level 1 (L1) data. The L1 data are converted into science-ready images (Level 2 or L2 data) following the steps described in the next subsection.

2.2.1 UVIT Data Reduction

The L1 data can be downloaded from the *AstroSat* archive webpage of the Indian Space Science Data Center (ISSDC)*. The creation of scientifically usable L2 data from L1 involves several steps, which are implemented in the form of pipelines. For generating the L2 datasets of GCs studied in Chapters 3, 4 and 5, I have used CCDLAB, a graphical user interface software package (Postma & Leahy 2017, 2021, hereafter PL17 and PL21). For the work in Chapter 6, I have directly utilized the science-ready L2 data downloaded from the *AstroSat* archive webpage, which is processed using the UVIT Level-2 pipeline (UL2P; Ghosh et al. 2022).

The major steps implemented in the reduction pipeline involve (i) correction for the *fixed pattern noise*, which is a bias introduced while calculating centroids for under-sampled point spread functions (PSFs), (ii) correction for field distortion that occurs primarily because of the optical fiber taper, (iii) rejection of duplicate data, (iv) weighting each event centroid with the flat-field to account for changes in the quantum efficiency across the detector, (v) correction for non-uniform exposure, especially in the outskirts of the imaging field, caused as a result of the spacecraft drift, (vi) removal of frames that have cosmic ray shower, (vii) correction for the satellite drift using the VIS data or UV data, (viii) orienting all the centroid-lists to the same frame by applying a transformation matrix, (ix) addition of the co-aligned centroid lists for each filter to create a *master* image, (x) PSF optimization

---

*`https://webapps.issdc.gov.in/astro_archive/archive/Home.jsp`

to correct for any excess drift in the images that tends to stretch a point source into a streak.

2.2.2 Astrometric Calibration

The astrometric calibration of the science-ready images was carried out in two steps. An approximate solution was first obtained by visually matching stars in the UVIT image with those from the *GALEX* FUV or NUV image (whichever available) using the *Astrometrical Calibration* option in *Aladin* software (Bonnarel et al. 2000). This solution was then fine-tuned using the *Gaia* catalog. Finally, the instrumental positions in the UVIT catalog were transformed into World Coordinate System (WCS) coordinates using the *wcsctran* task of Image Reduction and Analysis Facility (IRAF). The final solution has an accuracy of $\sim 0.5''$.

2.2.3 Image Analysis: Crowded Field Photometry

To measure the brightness of the sources in the UVIT images, I used the *daophot* package (Stetson 1987) included in IRAF following the steps described in the manual by W. E. Harris[†]. Firstly, the sources were detected with the *daofind* task, and their aperture photometry magnitudes were computed with the *phot* task with an aperture ~ average full-width at half maximum (FWHM) of a few bright, isolated stars. A few stars with good profiles were chosen interactively using the *pstselect* task to generate the model PSF using the PSF task. The model PSF was then fitted to all the sources in the aperture photometry file using the *allstar* task to obtain the PSF-fitted magnitudes. These magnitudes were then converted to the aperture photometry scale by adding the mean difference between

---

[†] `https://physics.mcmaster.ca/~harris/daophot_irafmanual.txt`

the *allstar* magnitudes and aperture photometry magnitudes of bright, isolated stars. The fiducial aperture to estimate the aperture correction was determined using the curve-of-growth method. The correction thus estimated was added to the magnitudes of all the sources. Lastly, the magnitude conversion to the AB system was carried out, and saturation correction was applied following the prescriptions in Tandon et al. (2017, 2020).

2.3 Archival Datasets

The UVIT dataset was complemented with multiband astrophotometric catalogs for selecting cluster members and characterizing the stellar populations. The catalogs used are discussed below.

2.3.1 HST-based Catalogs

The stellar populations in the crowded central regions of GGCs are best studied using a facility with excellent spatial resolution, such as the HST. This space-based telescope with a primary mirror of diameter 2.4 m has an imaging FWHM ranging from $\sim 0.067''$to $0.156''$. The telescope has been operational for more than three decades with several instruments. The instruments presently operational include the Advanced Camera for Surveys (ACS), Wide Field Camera 3 (WFC3), Cosmic Origins Spectrograph (COS), Space Telescope Imaging Spectrograph (STIS), and so on.

The ACS Survey of Globular Clusters (PI A. Sarajedini, Anderson et al. 2008) presented a homogeneous photometric catalog covering the central $202''\times\ 202''$of 65 GGCs using the Wide-Field Channel (WFC). The catalog included observations in two optical passbands, F606W and F814W. This dataset was complemented by imaging numerous GGCs with the UV/Visible channel (UVIS) of the WFC3 covering the central $162'' \times 162''$. The observations were made using the NUV/blue filters F275W, F336W, and F438W. These are known as “magic trio” filters due to their sensitivity to the variations in the abundances of elements such as C, N, and O, facilitating the identification and characterization of MSPs. By merging both these datasets, it was also possible to measure each subpopulation’s helium content. Thus, Piotto et al. (2015); Nardiello et al. (2018) published the final catalog, including the astrometry, photometry, and proper-motion-based cluster membership probabilities for 56 GGCs under the HUGS program.

The HUGS catalog provides photometric values measured by adopting three different methods, each suitable for different magnitude ranges. The best choice is to adopt the photometric method that yields CMDs with the least spread. All the magnitudes in the catalog are calibrated to the Vega system. In the case of NGC 2808 and NGC 6397, I have used the HUGS dataset.

Since ω Centauri was not included in the HUGS program, a comprehensive astrophotometric catalog published by Bellini et al. (2017a) covering the core radius of ω Centauri was used. The catalog included photometry for 478,477 stars in 18 WFC3/UVIS passbands and 8 WFC3/IR passbands.

2.3.2 Gaia-based Catalogs

The UVIT covers a much larger FOV compared to HST, and several sources lie outside the coverage of HST. Hence, to identify the cluster members among these sources, the datasets from *Gaia DR2* and *Gaia EDR3* were used.

Gaia, a space-based astrometric survey mission, was launched by the European

Space Agency on 19 December 2013. A successor to the Hipparcos satellite, the main goal of *Gaia* is to survey a billion stars and map the Galaxy in 3 dimensions to shed light on its genesis and evolution. The satellite makes astrometric, photometric, and spectroscopic measurements. Over the entire duration of the mission lifetime, each part of the sky will be revisited up to 70 times. The spacecraft houses two telescopes having the same focal plane where 106 CCDs are arranged. The CCDs are grouped into four main components : (i) Sky Mapper - a group of 14 CCDs used for source detection and tracking, (ii) Astrometric CCDs - a collection of 62 CCDs to estimate the object positions, parallaxes, and proper motions by observing with a broad filter, G band (330 to 1050 nm), (iii) Red and Blue photometers - assemblies of 7 CCDs each, carrying out photometric observations in two passbands, G_{RP} (640-1050 nm) and G_{BP} (330-680 nm), (iv) Radial Velocity Spectrometer - illuminates 12 CCDs and measures spectra with resolving power, $R = \lambda/\delta\lambda \sim 11\,700$. Further details on the mission can be found in Gaia Collaboration et al. (2016).

The first release of the *Gaia* data happened in September 2016 and had many shortcomings in terms of completeness, photometric accuracy, etc., which were overcome significantly in further data releases. In the case of NGC 2808 (Chapters 3 and 4, I used the catalog of possible cluster members provided by Gaia Collaboration et al. (2018) based on proper motions measurements from *Gaia DR2* released in April 2018. In order to identify the cluster members in ω Centauri (Chapter 5) and NGC 6397 (Chapter 6), I used the catalog published by Vasiliev & Baumgardt (2021) with cluster membership probabilities based on proper motions from *Gaia EDR3* released in December 2020. However, it is to be noted that the *Gaia* catalogs still suffer from limitations in crowded regions and are complete only within the magnitude range of 12 to 17 mag in the G band.

2.3.3 Ground-based Photometric Catalog

The optical counterparts of UVIT sources outside *HST* FOV were identified, and their multiband photometric measurements were obtained from the catalog published by Stetson et al. (2019).

This catalog is based on archival and proprietary data collected over several years from various ground-based facilities such as the 0.4 m telescope at the Maria Mitchell Observatory, Nantucket, to the 8 m Very Large Telescope at the European Southern Observatory, Paranal. It includes photometric observations of 48 GGCs in the Johnson-Cousins $UBVRI$ bands. The photometric magnitudes reported in the catalog are the weighted means of magnitudes from individual observations. The catalog also reports the source positions, photometric errors in each passband, photometric quality parameters, and the number of images used to derive the photometry.

2.4 Analysis Methodology

2.4.1 Catalog Cross-Matches

A crucial step in the analysis methodology employed in this thesis is the cross-matching between various datasets. The identification of NUV/optical counterparts to the UVIT detections from the HST-based catalogs is especially challenging because of the following reasons : (i) the high stellar densities in the central regions of GCs, (ii) the superior spatial resolution of HST compared to UVIT which results in multiple HST sources entering within the PSF of one UVIT source, and (iii) larger number of sources in the NUV/optical regimes compared to FUV-bright sources which increase the possibility of wrong cross-matches. The general cross-match steps adopted were as follows. In order to minimize wrong cross-identifications, only those stars which were expected to be UV-bright were pre-selected from the HST catalogs. In the case of NGC 2808, where the central region could not be resolved even using UVIT/FUV filters, the HST subset was further filtered to only include those sources which did not have a neighbor within $1.8''$(which was the maximum UVIT PSF). The cross-match between the HST subset and UVIT catalogs was then carried out using the TOPCAT software package (Taylor 2005) with appropriate match radii. The cross-identification of counterparts in the outer regions of the clusters from *Gaia* and ground-based catalogs is simpler because of the reduced crowding. More details on the cross-identifications are described in the respective chapters.

2.4.2 Spectral Energy Distributions

SED encodes the information regarding the energy emitted by an astrophysical source as a function of the wavelength. The SED of a source can be generated using photometric measurements in multiple bandpasses over different wavelength ranges. This is equivalent to obtaining a very low-resolution spectrum of the object but has many advantages. In crowded environments like GGCs, getting the spectra of several sources is extremely challenging due to limited access to the appropriate facilities and time constraints. Multiband photometry and SEDs prove to be excellent alternatives in such scenarios. Stellar parameters such as effective temperature and bolometric luminosity can be estimated from SEDs.

I used the VO SED Analyser (VOSA; Bayo et al. 2008) tool for fitting the SEDs. This functionality generates flux values for the chosen theoretical models using the transmission curves of the required photometric filters. The best-fit parameters of the SEDs were estimated by comparing the observed and synthetic photometric points using a χ^2 minimization method. Assuming there are N photometric points and N_f fitted parameters for the model, the χ^2_{red} value is calculated using the relation,

$$\chi^2_{red} = \frac{1}{N - N_f} \sum_{j=1}^{N} \left\{ \frac{(F_{o,j} - M_d F_{m,j})^2}{\sigma^2_{o,j}} \right\} \tag{2.1}$$

where $F_{o,j}$ is the observed flux and $\sigma_{o,j}$ is the error associated, $F_{m,j}$ is the theoretical flux predicted by the model and $M_d = (\frac{R}{D})^2$ is the multiplicative dilution factor (where R is the star's radius and D is the distance to the star). Therefore, if we know the object's distance, we can determine its radius using the scaling factor. The bolometric luminosity of the source is calculated from the best-fit temperature, T_{eff}, using the relation,

$$L_{bol} = 4\pi\sigma_{SB} R^2 T^4_{eff} \tag{2.2}$$

VOSA calculates two additional parameters, Vgf and Vgf_b, as estimates of the *visual goodness of fit*. These modified chi-square parameters can be employed in cases where the chi-square value is large, although the fit seems good visually. This can typically happen when there are data points with very small photometric errors. Vgf (Vgf_b) is a modified, reduced chi-square parameter calculated by mandating that the flux errors are, at least, 2% (10%) of the observed values. Vgf (Vgf_b) less than 25 (15) is accepted as a good fit (Rebassa-Mansergas et al. 2021).

VOSA uses the relation given by Fitzpatrick (1999) to account for the extinction in the observed photometric points.

The errors in the fitted parameters are estimated using the statistical approach described in the VOSA documentation. Starting from the observed SED, one hundred or more virtual SEDs are produced by incorporating a Gaussian random noise for each point (proportional to the observational error). The best fit is then obtained for each of these SEDs, and the statistics for the distribution of each parameter are estimated. If the standard deviation of the parameter distribution is greater than half the grid step, this value is reported as the corresponding uncertainty. If not, half the grid step is quoted as the parameter uncertainty.

The next subsection briefly describes the theoretical models used for fitting the SEDs.

2.4.3 SED Models

This thesis explores the properties of UV-bright sources in various evolutionary phases covering multi-wavelength datasets ranging from FUV to NIR wavelengths. Hence, various theoretical models have been adopted to fit the SEDs of sources appropriate for the source type and wavelength range. These are described below:

Kurucz models: The Kurucz stellar atmospheric models were developed by Castelli et al. (1997); Castelli & Kurucz (2003), based on the ATLAS9 code (Kurucz 1970) considering Local Thermodynamical Equilibrium (LTE) and hydrostatic equilibrium as well as by incorporating appropriate treatments for opacities, stellar convection, rotation, etc. The synthetic photometric data points corresponding to various filters are derived by convolving the filter response functions with the Kurucz synthetic spectra obtained from the model atmospheres. The synthetic spectra cover the wavelength range from UV to IR. The model grid has three parameters, [Fe/H], $T_{\rm eff}$, and $\log g$, spanning a wide range of values. [Fe/H] ranges from -2.5 to 0.5 dex in steps of 0.5 dex. $T_{\rm eff}$ covers the range from 3500 to 50 000 K with step sizes of 250 K for $T_{\rm eff} < 13\,000$ K and 1000 K for $T_{\rm eff} >$ 13 000 K. The $\log g$ ranges from 0 to 5 dex in steps of 0.5 dex. The models have also been computed for different values of α abundances, namely, $\alpha = 0.0$ dex and $\alpha = 0.4$ dex.

Tübingen NLTE Model Atmosphere Package (TMAP) models: In TMAP (Werner & Dreizler 1999; Werner et al. 2003; Rauch & Deetjen 2003), the stellar atmospheres are calculated assuming a spherical or plane-parallel geometry, considering hydrostatic and radiative equilibrium, by allowing departures from LTE. There are several TMAP model grids available. The TMAP Grid 1 has two parameters, namely, $T_{\rm eff}$ ranging from 20 000 to 40 000 K and $\log g$ ranging from 4.5 to 7 dex in steps of 0.5 dex. The TMAP Grid 2 has two parameters, namely, $T_{\rm eff}$ ranging from 20 000 to 150 000 K and $\log g$ ranging from 4.5 to 9 dex in steps of 0.5 dex. The TMAP Grid 3 has three parameters, namely, $T_{\rm eff}$ ranging from 50 000 to 190 000 K; $\log g$ ranging from 5 to 9 dex in steps of 0.5 dex and H mass fraction ranging from 0 to 1 in steps of 0.1. The TMAP Grid 4 has the same parameters as Grid 3 except that the $T_{\rm eff}$ starts from 20 000 K and $\log g$ from 4 dex. The TMAP grid has the following parameters: $T_{\rm eff}$ ranging from 50 000 to 190 000 K (with finer and coarser steps); $\log g$ ranging from 5 to 9 dex in steps of 0.5 dex and He mass fraction ranging from 0 to 1 in steps of 0.1. The TMAP Tübingen grid has the four parameters: $T_{\rm eff}$ ranging from 30 000 to 1 000 000 K (with finer and coarser steps); $\log g$ ranging from 3.8 to 9 dex (with finer and coarser steps), H and He mass fractions ranging from 0 to 1.

Koester WD models: The Koester models (Koester 2010) are suitable for DA-type WDs having pure H atmospheres. These model atmospheres are calculated assuming plane-parallel, 1D geometry, considering hydrostatic equilibrium and

LTE. The model grid has two parameters: $T_{\rm eff}$ ranging from 5000 to 80 000 K with varying step sizes, and $\log g$ ranging from 6.5 to 9.5 dex in steps of 0.25 dex.

Levenhagen models: The Levenhagen models (Levenhagen et al. 2017) are a set of LTE and NLTE models ideal for hot WDs of DA spectral type with pure H atmospheres. The synthetic spectra cover wavelengths ranging from 90 nm to 2.5 µm. The model grid has two parameters: $T_{\rm eff}$ ranging from 17 000 to 100 000 K with a step size of 10 000 K; and $\log g$ ranging from 7 to 9.5 dex in steps of 0.1 dex.

Pacheco models: Pacheco et al. (2021) provided synthetic spectral grids for subdwarf stars by adopting non-LTE fully line-blanketed atmospheres, covering a wavelength range from 100 to 1000 nm. The model grid has the following parameters: $T_{\rm eff}$ ranging from 10 000 to 65 000 K (step size of 5 000 K for $T_{\rm eff}$ upto 45 000 K and then a step size of 20 000 K); $\log g$ ranging from 4.5 to 6.5 dex in steps of 0.5 dex; [Fe/H] which can take two values, −1.5 dex or 0.0 dex; and log (n_{He}/n_H) ranging from -4.98 to 3.62.

Husfeld models: Husfeld et al. (1989) developed NLTE model atmospheres for hot He-rich stars considering plane-parallel geometry, hydrostatic and radiative equilibrium. The atmosphere was assumed to be composed of hydrogen and helium. The model grid has three parameters: $T_{\rm eff}$ ranging from 35 000 to 80 000 K with a step size of 5 000 K; and $\log g$ ranging from 4 to 7 dex in steps of 0.5 dex; and He mass fraction, Y ranging from 0 to 0.7.

2.5 Summary

This chapter of the thesis deals with the data used and the general analysis methodologies adopted. To summarize,

- The *AstroSat*/UVIT instrument, which is the main observational facility used in this thesis, is described. The pipelines used to generate science-ready images, the astrometric calibration, and the image analysis method are also discussed.
- The major complementary catalogs based on *HST*, *Gaia* and ground-based telescopes, used to identify optical counterparts and cluster members, are described.
- The general steps adopted to cross-match catalogs are briefly discussed.
- The main analysis technique of SED-fitting and its details are described.

Chapter 3

A Census of Post-Horizontal Branch Stars in NGC 2808[†]

3.1 Introduction

The late evolutionary stages of low-mass stars, especially post the core-He burning stage, are not well characterized yet. Since these phases are relatively fast progressing, the number of stars observable at a given time is small. The poor number statistics of such observed stars hinders the testing and improvement of available theoretical models. This Chapter deals with the census and analysis of the unexplored evolved population of pHB members or UV-bright stars in the GC, NGC 2808.

[†] Results of this work are published in Prabhu et al. (2021a).

NGC 2808, located at a distance of 9.6 kpc (Harris 1996, 2010 edition, H96), is a massive and dense GC, with a mass = 7.42×10^5 $M_\odot$ and a central density ≈ 4×10^4 $M_\odot/pc^3$ (Baumgardt & Hilker 2018). It has an age = 10.9 ± 0.7 Gyr (Massari et al. 2016) and [Fe/H] = −1.14 dex. Schiavon et al. (2012) presented a catalog of candidate pAGB, peAGB and AGB-manqué stars in 44 Galactic GCs, including NGC 2808, using *Galaxy Evolution Explorer* (*GALEX*) FUV and NUV observations. However, the spatial resolution of GALEX ($\sim 5''$) posed limitations on their investigation. Furthermore, the membership information for these stars was not available then.

Moehler et al. (2019) combined photometric observations from various missions such as Ultraviolet Imaging Telescope (UIT), *GALEX*, *Swift* Ultraviolet-Optical Telescope (UVOT) and *HST* to obtain the census of UV-bright stars in 78 GCs. The atmospheric parameters of the brightest pHB stars in the sample (including 3 stars from NGC 2808), derived from optical spectroscopic observations, were used to assess their evolutionary status. The number of theoretically predicted and observed hot pAGB stars for 17 GCs (excluding NGC 2808) were found to be comparable, though affected by poor statistics. The catalog of such stars in their list of clusters is yet to be published. Several optical spectroscopic studies of previously identified bright pHB stars in other GCs have been performed to shed light on their chemistry and evolutionary status (Thompson et al. 2007; Chayer et al. 2015; Dixon et al. 2017, 2019).

Jain et al. (2019) studied NGC 2808 using the data obtained from the UVIT. They reported the detection of hot stars belonging to different classes, such as EHB, BHB, RHB, BHk, pAGB, and BSSs, from UV CMDs, albeit without membership analysis. They focused on the photometric gaps in the UV CMDs and the multiple stellar populations in the cluster.

In this chapter, the first catalog of UV-bright member stars in this cluster is presented along with their surface parameters derived through the analysis of their SEDs. The archival UV data from the UVIT is combined with the UV-optical catalogs based on observations from the *HST* (Brown et al. 2001; Nardiello et al. 2018), *Gaia* (Gaia Collaboration et al. 2018) and ground-based telescopes (Stetson et al. 2019). The member stars in the central cluster region covered by *HST*– within $\sim 2\farcm7 \times 2\farcm7$ (hereafter referred to as inner region), and the region outside *HST* FOV (outer region) are identified utilizing the proper motion-based membership information from the *HST* and *Gaia DR2* catalogs, respectively. The evolutionary phase of the UV-bright stars is investigated, and the observed number of hot p(e)AGB [*] stars are compared with the expected number derived from theoretical estimations. Though Jain et al. (2019) used the UVIT data to study the HB population, here the aim is to focus on the UV-bright members of the cluster and parameterize them to throw light on the short-lived late evolutionary phases of low-mass stars.

3.2 Observations and Data Reduction

The archival UVIT data for NGC 2808 is utilized in two FUV (F154W and F169M) and four NUV filters (N242W, N245M, N263M, and N279N). The images were created using the CCDLAB software package (PL17) as described in Chapter 2. The final exposure times for the science-ready image in various filters are tabulated in Table 3.1. The UVIT image of NGC 2808 is shown in Figure 3.1 with the sources detected in F154W represented by blue color and those in N242W by green color.

---

[*] The notation p(e)AGB is used to indicate either pAGB or peAGB star.

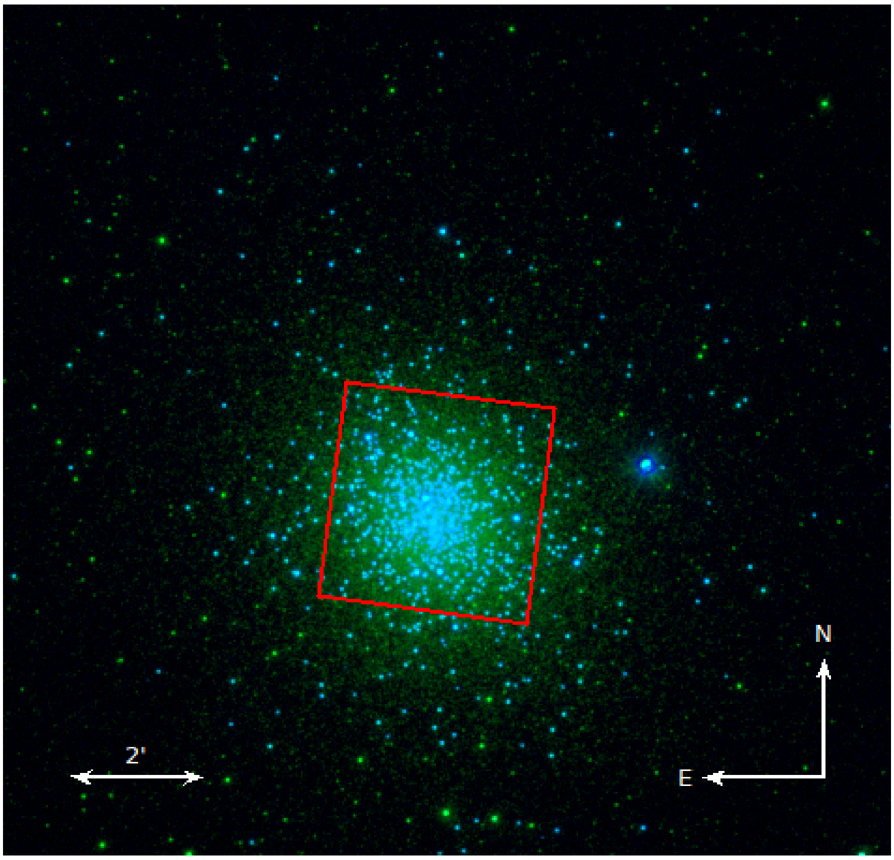

FIGURE 3.1: The UVIT image of NGC 2808 with F154W detections in blue and N242W ones in green. The *HST* WFC3/UVIS FOV which covers the inner $\sim 2\overset{\prime}{.}7 \times 2\overset{\prime}{.}7$ region of the cluster is marked in red.

3.2.1 Photometry

Crowded-field photometry was carried out on the FUV and NUV images from the UVIT, as detailed in Chapter 2. The number of detected stars in various filters is presented in Table 3.1. The plots of magnitude versus PSF-fit error for different filters are shown in Figure 3.2.

The magnitudes in all filters were corrected for extinction by adopting a reddening value, $E(B-V) = 0.22$ mag (H96) and $R_V = 3.1$. The corresponding extinction coefficient in the V band is, $A_V = 0.682$ mag. The extinction coefficients presented in Table 3.1 were calculated employing the relation given by Cardelli et al. (1989).

TABLE 3.1: The UVIT observation and photometry details for NGC 2808

Filter	λ_{mean} (Å)	$\Delta\lambda$ (Å)	Zero point (mag)	Exp. time (s)	No. of stars	FWHM of Model PSF (*arcsec*)	A_λ (mag)
F154W	1541	380	17.77	4987.34	2692	1.47	1.79
F169M	1608	290	17.45	4220.36	3996	1.45	1.75
N242W	2418	785	19.81	1040.99	5056	1.41	1.70
N245M	2447	280	18.50	886.42	2686	1.64	1.65
N263M	2632	275	18.18	354.46	1309	1.58	1.43
N279N	2792	90	16.50	2629.94	2868	1.42	1.32

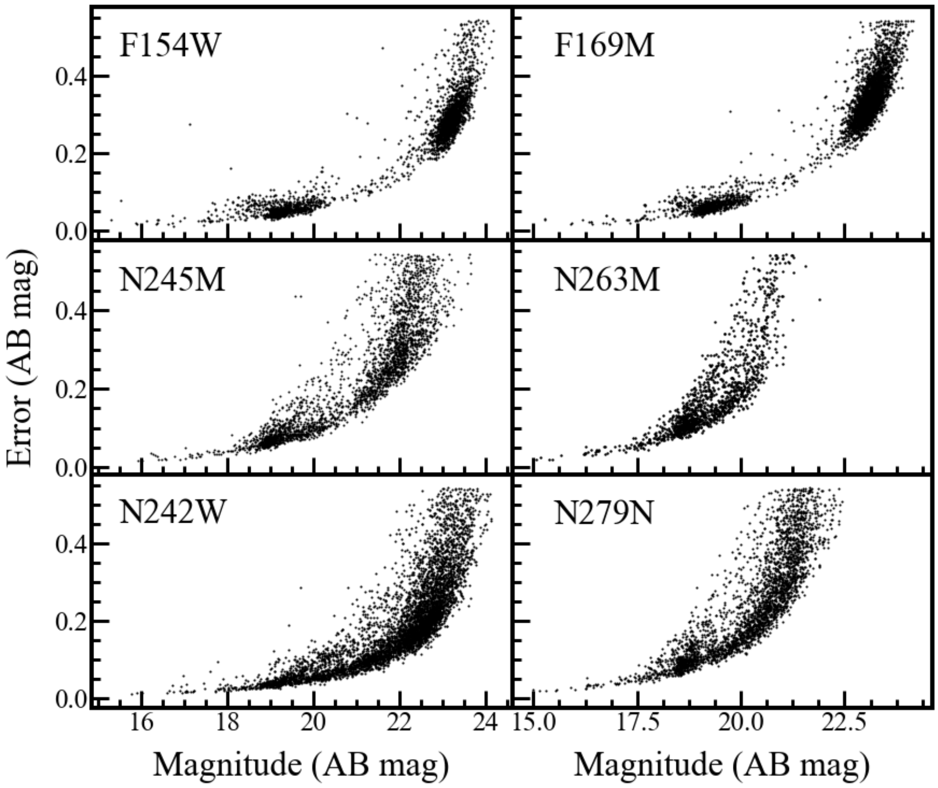

FIGURE 3.2: The magnitude (without extinction correction) versus PSF-fit errors for the UVIT observations of NGC 2808 in six filters. The filter names are indicated in the top left corner of each panel.

3.3 UV-Optical and UV CMDs

3.3.1 Cross-Match Of The UVIT Data With The *HST* Data

In order to identify various stars detected in the UVIT images, they were cross-matched with the HUGS catalog (Nardiello et al. 2018; Piotto et al. 2015) in the inner region of the cluster (within $\sim 2\farcm7 \times 2\farcm7$). Since the main focus of this work is the UV-bright population, only the stars which are expected to be bright in the UV were chosen, such as the pHB, HB, and BSSs from the *HST* CMD and their unique counterparts in the UVIT images were identified as explained below.

The CMDs and color-color plane (CCP) using the *HST* data for the inner region of the cluster are shown in Figure 3.3, where the stars are color-coded according to their classification. The top right panel shows the CMD used to identify the 28 pHB member stars (purple diamond symbols). The bottom right panel shows the CMD used to identify the 176 BSS members (magenta circles) as per the procedure described in Raso et al. (2017). To highlight how effectively the adopted color combinations separate the BSSs and pHB stars from the rest of the populations, we have depicted these sources in faded colors on the top and bottom right panels as well. The division of HB into RHB, BHB, EHB, B gap objects, and BHk was done using the $m_{F275W} - m_{F438W}$ vs. $C_{F275W,F336W,F438W}$ plane, as shown in the left panels. Here, the quantity $C_{F275W,F336W,F438W}$ is a pseudo-color defined by Milone et al. (2013) which corresponds to $(m_{F275W} - m_{F336W}) - (m_{F336W} - m_{F438W})$. The classification adopted here is similar to that of Brown et al. (2016). The RR Lyrae sources were identified by cross-matching with the data from Kunder et al. (2013). Since the *HST* images have a much better spatial resolution, a simple cross-match with the UVIT data may yield wrong identifications due to crowding in the innermost region of the cluster. A case of multiple *HST* stars for a single

UVIT detection is demonstrated in Figure 3.4, where the *HST* F275W image and the UVIT F154W image are overlaid. The gray patch is the UVIT detection, whereas in black are the stars from *HST* in a region of about $5'' \times 5''$. In order to avoid such wrong/multiple identifications, a Python code that returns only those *HST* stars among the pHB, HB, and BSS stars, which have no neighbors within $1.8''$ radius (maximum UVIT PSF) from them, was used. As the crowding is maximum near the cluster center, no *HST*-UVIT cross-match was performed for the innermost region (radius $< 30''$). Finally, 491 stars were selected from the *HST* catalog, and these were then cross-matched with the UVIT-detected stars with a maximum match radius of $1''$. All the cross-matched stars were found to have a photometric error < 0.2 mag in all the UVIT filters.

3.3.2 Cross-Match Of The UVIT Data With The *Gaia DR2* And Ground-Based Optical Data

The UVIT FOV is much larger than the *HST* FOV, and it includes the cluster's outer region as well. In order to effectively use the stars detected by UVIT in the outer region, the UVIT data were combined with other data for their identification and membership, as explained below. The list of possible member stars of the cluster in the outer region was obtained from the *Gaia DR2* paper, Gaia Collaboration et al. (2018), and their *UBVRI* photometry from Stetson et al. (2019). These datasets were cross-matched first to get the cluster members and their optical photometry. The resultant set was then cross-matched with the UVIT data, with a maximum match radius of $0\farcs5$. Then, only those stars with UVIT magnitude error < 0.2 mag were included in the analysis. The cross-matched stars were visually checked for wrong/multiple identifications. Further, the B, V, and I Johnson-Cousins magnitudes of all these stars were transformed into the equivalent *HST* filter magnitudes (WFC3/UVIS F438W, ACS/WFC F606W, and

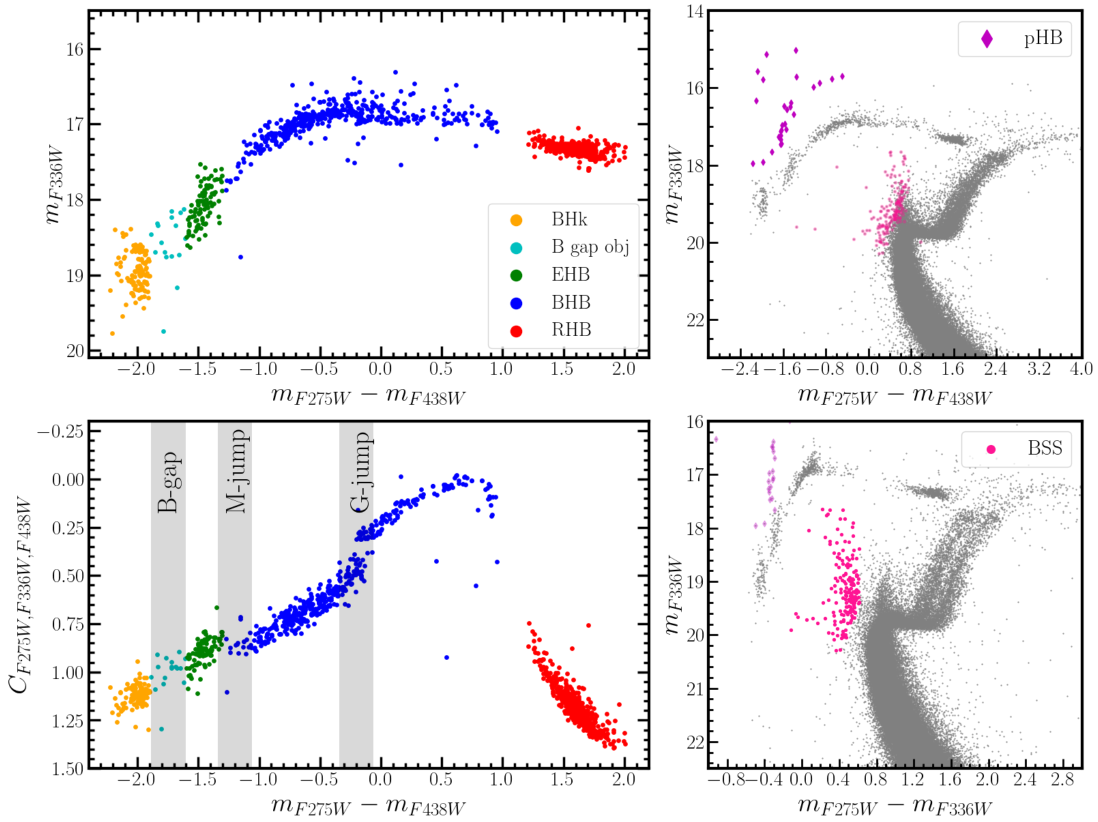

FIGURE 3.3: On the left panels are the CMD and CCP showing the categorization of HB stars into RHB, BHB, EHB, and BHk stars using HUGS data. The prominent photometric discontinuities such as the Grundahl jump (G-jump; Grundahl et al. (1998, 1999)), the Momany jump (M-jump; Momany et al. (2002, 2004)) and the gap between EHB and BHk stars (B-gap; Sweigart (1997); Brown et al. (2001)), are shown in the CCP. The top and bottom right panels show the CMDs used to select the pHB stars and BSSs, respectively, with all the other member stars shown in gray.

ACS/WFC F814W), using the transformation equations of Harris (2018) and Sirianni et al. (2005) so that stars in the inner and outer regions could be shown in the same color and magnitude plane.

3.3.3 Color-Magnitude Diagrams

The UV-optical and UV CMDs were constructed for the cluster with all cross-matched members. The BaSTI (Bag of Stellar Tracks and Isochrones) theoretical

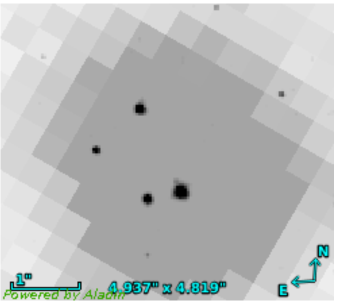

Figure 3.4: An example of a possible wrong cross-match between *HST* and UVIT detected stars due to the crowding in the inner region of the cluster. The UVIT detection in the F154W filter is shown in gray, overlaid with the *HST* F275W detected stars in black.

ZAHB and terminal-age HB (TAHB; end of He burning phase) models from Hidalgo et al. (2018) were fitted to the HB sequence of the cluster CMD. These models were generated in the UVIT, *HST*/WFC3, and *HST*/ACS filters by choosing metallicity [Fe/H] = −0.9 dex, He abundance = 0.249, solar scaled [α/Fe] = 0.0, and no convective overshoot. These models take into account the effects due to atomic diffusion at the hotter end of the HB, as is evident from the close match with the CMDs.

Figure 3.5 shows the CMD of the cluster for the inner region using the *HST* data. Stars that are used for the cross-match with the UVIT data are shown along with the ZAHB and TAHB models. The gray dots represent stars with more than 90% membership probability.

Figure 3.6 shows the optical and FUV-optical CMDs for all the members detected in the F154W UVIT filter. To plot these CMDs, the F438W and F606W magnitudes in the Vega system were transformed into the AB system.[†] The filled (unfilled) symbols represent the stars located in the inner (outer) region of the cluster. In FUV, mainly the hotter part of the HB (BHB and EHB), BHk, pHB, and a few BSSs have been detected. Three RR Lyrae variables are also identified. In the $m_{F154W} - m_{F606W}$ vs. m_{F154W} plot (shown in the right panel), the BHB

[†] The conversion factors from http://waps.cfa.harvard.edu/MIST/BC_tables/zeropoints.txt were used.

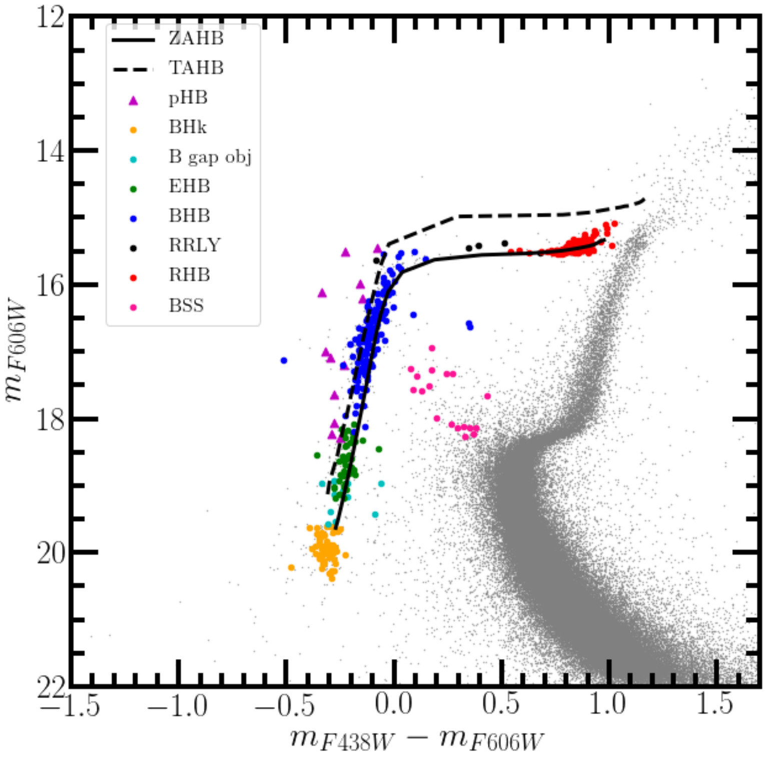

FIGURE 3.5: The optical CMD showing the 491 stars (in colored symbols) selected from *HST* catalog for cross-match with the UVIT data based on the selection criteria described in the text. All the cluster members (membership probability more than 90%) in the *HST* FOV are shown with gray points, and the black solid and dashed lines represent the BaSTI ZAHB and TAHB models with [Fe/H] = −0.9 dex, respectively.

stars have a relatively tight distribution in magnitude, whereas the EHB, B gap and BHk stars show a spread in the m_{F154W} magnitude, and with respect to the ZAHB track. Many of them are also found to be fainter than the ZAHB model. One of the detected BSSs, located in the outer region, is very bright in the F154W filter. The RHB stars are hardly detected as their surface temperatures are not high enough for significant FUV emission. The detected pHB stars are found to be brighter than the TAHB, with a spread of about 2 magnitudes in the F154W filter and 4 magnitudes in the FUV-optical color. These UV-bright stars are discussed in detail in the next section.

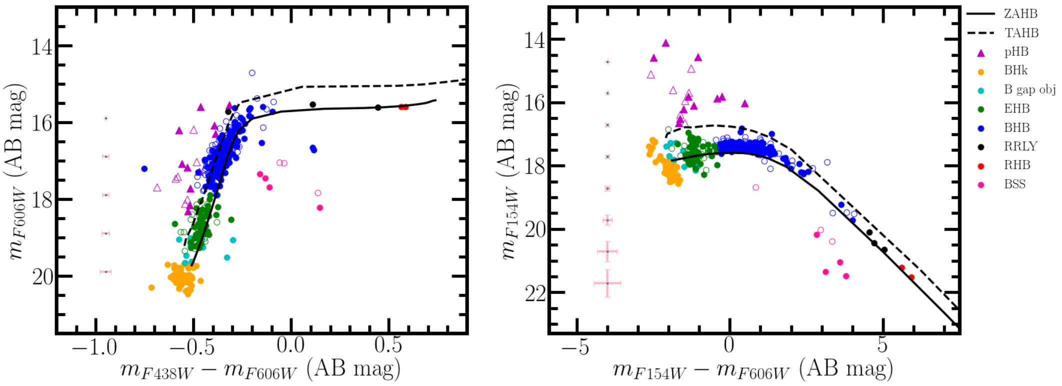

FIGURE 3.6: The optical and FUV-optical CMDs for all the members in NGC 2808 common to the UVIT FUV F154W filter and other catalogs (*HST*, *Gaia DR2* and ground-based optical data). The stars detected within the inner 2.′7 × 2.′7 region of the cluster are marked with filled symbols and those in the outer region with unfilled symbols. The black solid and dashed lines are the ZAHB and TAHB models, the same as in Figure 3.5. The photometric errors in magnitude and color are also shown along the left side of each plot.

Similarly, Figure 3.7 shows the optical and NUV-optical CMDs for stars detected in the N245M UVIT filter. In the N245M filter, apart from the above-mentioned sequences, the cooler RHB population has also been detected. The RHB stars form a tight sequence when compared to the rest of the HB sequence and are located close to the ZAHB track. On the other hand, the other HB phases show a large spread, with many of them located above and below the ZAHB track. The BHk sequence has the largest statistically significant spread in the N245M magnitude, as is evident from the $m_{N245M} - m_{F606W}$ vs. m_{N245M} CMD (right panel). The bright BSS is found to be located slightly fainter than the faintest BHB star.

The UV CMDs for all the stars common in the UVIT filters F154W and N245M are shown in Figure 3.8. In the $m_{F154W} - m_{N245M}$ vs. m_{N245M} CMD (left panel), the HB stars show a progressive reduction in the N245M magnitude as a function of $m_{F154W} - m_{N245M}$ color. In the case of the $m_{F154W} - m_{N245M}$ vs m_{F154W} CMD, the HB stars with color < 0.0 mag, have a horizontal sequence. The hot BHB, EHB, B gap, and BHk stars get mixed up in these CMDs. The bright BSS is found slightly fainter than the BHB stars, with $m_{F154W} - m_{N245M}$ color ~ 0.0 mag.

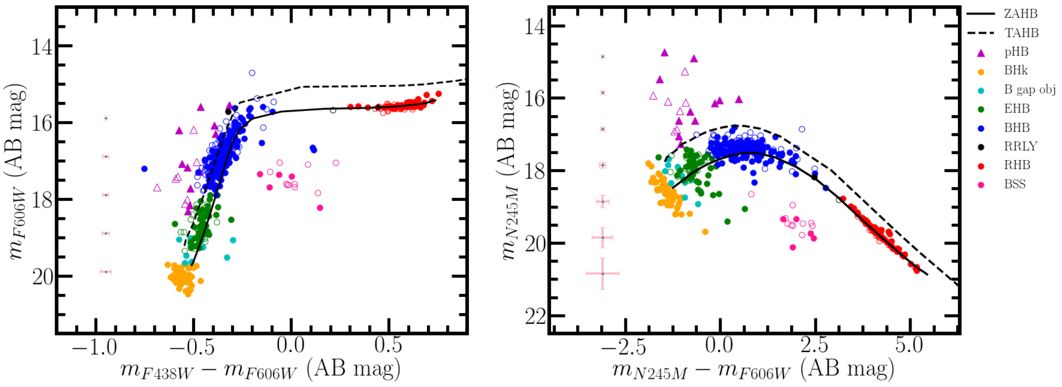

FIGURE 3.7: The optical and NUV-optical CMDs for all the stars in NGC 2808 common to the UVIT NUV N245M filter and other catalogs (*HST*, *Gaia DR2* and ground-based optical data). The details are the same as in Figure 3.6.

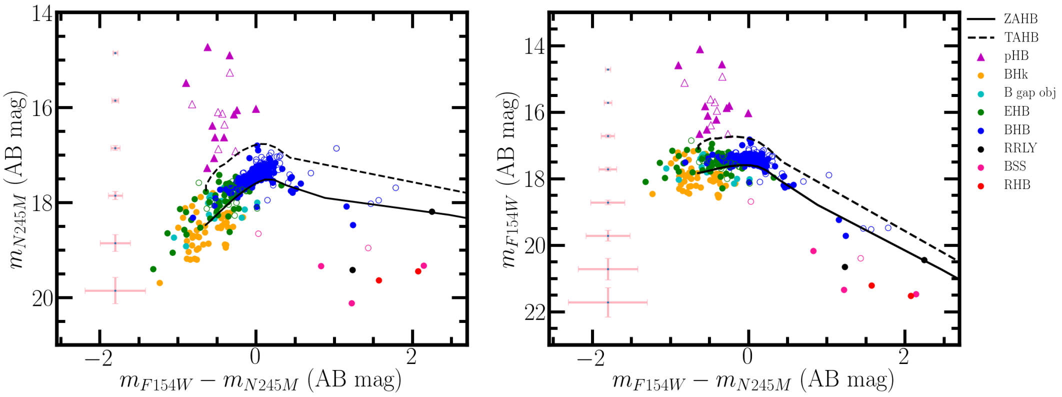

FIGURE 3.8: The UV CMDs for the cluster member stars common in F154W and N245M filters. The UV-bright stars (shown as purple triangles) are clearly brighter than the ZAHB by 1 mag or more in FUV and have FUV−NUV $<$ 0.7 mag.

Table 3.2 tabulates the number of stars belonging to different categories detected in each UVIT filter. In the outer region, since cluster members were selected based on *Gaia DR2* data with an approximate limiting magnitude of $V \simeq 20.5$ mag, no stars belonging to the optically faint B gap and BHk categories were found. A separate detailed study of the HB stars and BSSs presented in this section is planned for the near future.

Table 3.2: Number of pHB stars, BSSs, and different categories of HB stars in NGC 2808 detected in each UVIT filter, located within the HST FOV in the image. In parentheses are the numbers of these stars detected outside.

Filter	N_{pHB}	N_{BHk}	N_{Bgap}	N_{EHB}	N_{BHB}	$N_{RRLyrae}$	N_{RHB}	N_{BSS}
F154W	11(7)	53(0)	12(0)	48(21)	147(65)	3(0)	2(0)	4(3)
F169M	11(7)	52(0)	12(0)	49(21)	146(64)	2(1)	1(0)	3(1)
N242W	11(7)	49(0)	11(0)	45(21)	146(66)	4(1)	119(124)	9(28)
N245M	11(7)	48(0)	12(0)	45(20)	146(66)	2(1)	65(23)	5(10)
N263M	11(7)	23(0)	8(0)	29(17)	140(66)	3(1)	38(4)	4(1)
N279N	11(7)	40(0)	10(0)	40(17)	147(64)	5(1)	103(49)	8(2)

3.4 Observed UV-Bright Stars

The main aim of this study was to identify and characterize the pHB stars. Among the UVIT-detected stars in the outer regions, some bright stars were found to be non-members as per the list of possible members from Gaia Collaboration et al. (2018). The membership of these stars in the outer region was re-assessed, using methods presented in Singh et al. (2020), which also uses the *Gaia DR2* data. Two stars were found to have a membership probability of $\sim 90\%$. One star was found to have $\sim 40\%$ membership probability, and this was studied by Moehler et al. (2019) using optical spectroscopy. These 3 stars were included, along with the other pHB stars, for further study.

From the analysis, a total of 34 UV-bright member stars in this cluster were found, which could be classified as pHB stars. Of these, 18 stars have FUV and NUV data UVIT and are marked with purple triangles in the CMDs in Figures 3.6, 3.7 and 3.8. These sources satisfy the observational criteria for them to be classified as UV-bright stars, as laid out in Schiavon et al. (2012) – "brighter than the ZAHB by more than 1 mag in FUV, and the FUV−NUV color is less than 0.7 mag". The UVIT photometry for these stars is presented in Table 3.3.

TABLE 3.3: The UVIT photometry of pHB member stars in the GC, NGC 2808. Column 1 lists the star ID; columns 2 and 3 correspond to the R.A. and Decl. of the stars; columns 4 to 15 give the magnitudes and errors (AB system) in different UVIT filters. Note that the magnitudes are not corrected for extinction. The stars with IDs 12 to 27 are not resolved by UVIT and, hence, are not available in this table.

ID	R.A. (deg)	Decl. (deg)	F154W	err1	F169M	err2	N242W	err3	N245M	err4	N263M	err5	N279N	err6
Star 1	137.96181	-64.84165	18.437	0.039	18.514	0.041	19.017	0.033	18.924	0.070	18.757	0.093	18.783	0.083
Star 2	138.02575	-64.84307	16.349	0.018	16.346	0.023	16.923	0.029	16.549	0.023	16.389	0.045	16.515	0.031
Star 3	138.06046	-64.86146	16.376	0.020	16.417	0.018	17.450	0.038	17.135	0.027	17.077	0.056	17.190	0.037
Star 4	138.05040	-64.84379	15.899	0.018	15.891	0.018	16.724	0.031	16.380	0.028	16.325	0.040	16.444	0.032
Star 5	138.04719	-64.87492	18.313	0.030	18.289	0.034	19.015	0.039	18.710	0.052	18.476	0.088	18.483	0.068
Star 6	138.06813	-64.86459	17.817	0.025	17.727	0.031	17.826	0.024	17.680	0.039	17.419	0.053	17.439	0.055
Star 7	138.05264	-64.86779	17.888	0.028	17.825	0.029	18.629	0.045	18.274	0.052	18.105	0.094	18.224	0.060
Star 8	138.04842	-64.84887	17.597	0.025	17.559	0.029	18.087	0.031	17.702	0.046	17.473	0.064	17.525	0.049
Star 9	138.04760	-64.85790	17.657	0.025	17.611	0.034	18.208	0.055	17.799	0.041	17.588	0.051	17.524	0.056
Star 10	138.03820	-64.87028	17.613	0.023	17.579	0.030	18.743	0.061	18.031	0.042	17.930	0.075	17.856	0.059
Star 11	137.96088	-64.85092	18.006	0.032	18.004	0.035	18.540	0.032	18.277	0.044	17.995	0.071	18.403	0.065
Star 28	137.85352	-64.87929	18.184	0.029	18.178	0.044	18.652	0.030	18.525	0.048	18.342	0.087	18.623	0.087
Star 29	137.92453	-64.70158	17.404	0.025	17.465	0.025	17.807	0.022	17.749	0.034	17.675	0.048	17.814	0.054
Star 30	138.08369	-64.84865	17.747	0.025	17.738	0.031	18.173	0.026	18.010	0.041	17.975	0.071	17.932	0.053
Star 31	138.00728	-64.79293	16.723	0.020	16.748	0.020	17.058	0.019	16.917	0.020	16.855	0.042	16.950	0.039
Star 32	137.99974	-64.89071	16.906	0.025	16.953	0.024	17.844	0.035	17.583	0.038	17.515	0.044	17.712	0.066
Star 33	138.02306	-64.89646	18.447	0.034	18.477	0.036	18.759	0.025	18.569	0.055	18.339	0.082	18.651	0.093
Star 34	138.09187	-64.87727	17.489	0.025	17.493	0.027	18.003	0.035	17.779	0.042	17.745	0.064	17.704	0.063

Figure 3.9 shows the spatial locations of all the 34 observed UV-bright stars marked over the UVIT F154W image. Here, 11 out of the 18 UVIT-detected pHB stars (shown in red circles) lie in the *HST* FOV, and they have been uniquely cross-matched. This can be seen in Figure 3.10, where the *HST* F275W and the UVIT F154W images for these stars have been overlaid. Note that similar unique cross-matches are achieved for all the stars shown in the CMDs. The remaining 16 UV-bright stars (marked in blue circles in Figure 3.9) are located in the crowded innermost region of the cluster and, hence, could not be resolved by the UVIT. Among these, only 4 stars have FUV, and NUV photometric measurements from the *HST* STIS instrument (Brown et al. 2001), whereas all 16 have the NUV-optical data from the HUGS catalog.

These multi-wavelength photometric data for the UV-bright stars were used to determine their evolutionary status by estimating various parameters.

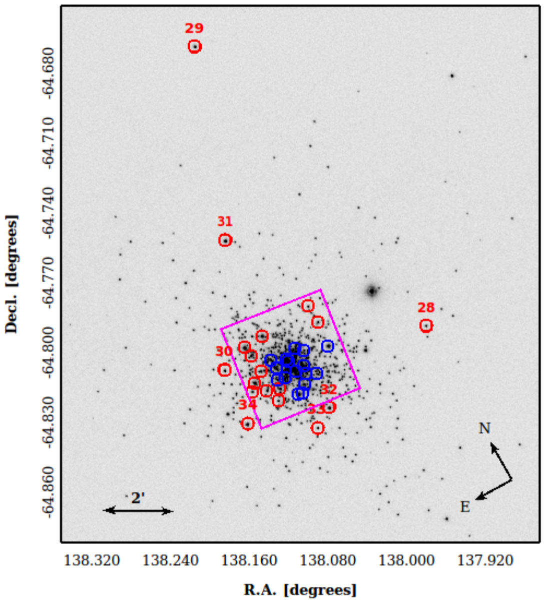

Figure 3.9: The 34 UV-bright stars in NGC 2808 marked over the UVIT F154W filter image of the GC. The magenta region marks the *HST* FOV. The star IDs are indicated near each star in the region outside the *HST* FOV. The 18 UV-bright stars with UVIT photometry are marked with red circles, and the rest with blue circles.

3.5 Spectral Energy Distributions

For estimating the physical parameters of the UV-bright stars, such as $T_{\rm eff}$, $L_{\rm bol}$, and radius, their SEDs were constructed with the available photometric data points. The virtual observatory tool, VOSA, was employed for the purpose as discussed in Chapter 2. A distance of $D = 9.6$ kpc and $E(B-V) = 0.22$ mag (H96) were assumed for the SEDs of all the pHB sources.

For all the UV-bright stars except two, the Kurucz models (Castelli & Kurucz 2003, hereafter CK03) with log g, [Fe/H] and T_{eff} as the possible free parameters were used for fitting the SED. In these models, the range of admissible values

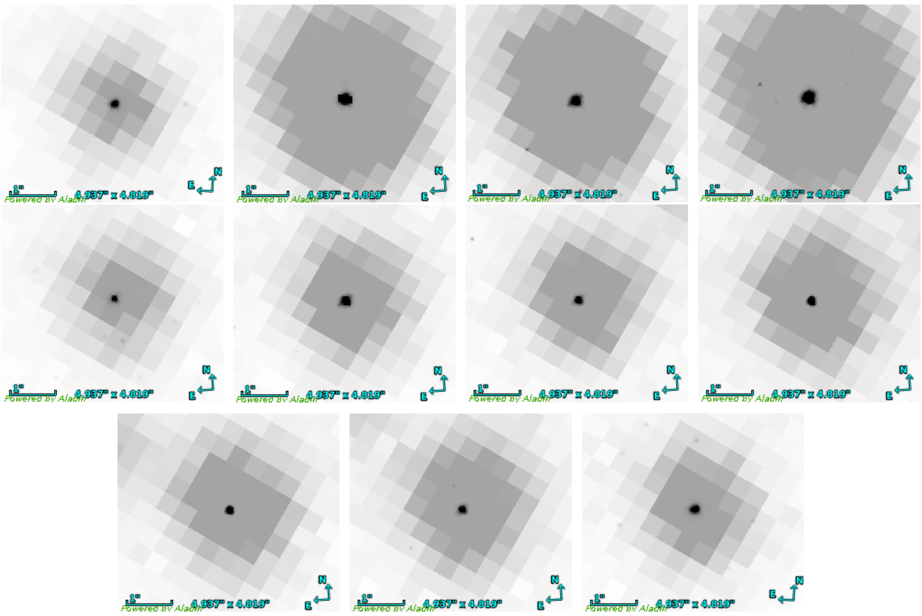

Figure 3.10: The UVIT F154W images of all the 11 UV-bright stars in the inner region of the cluster, which are uniquely cross-matched with stars in the HUGS catalog. Here, the UVIT F154W image of each star is shown in gray and overlaid with the corresponding *HST* F275W detection in black.

for the free parameters is 0.0 to 5.0 for log g, -2.5 to 0.5 for [Fe/H] and 3500 to 50000 K for T_{eff}. For the remaining two stars, i.e., Star 3 and Star 32 in Table 3.4, the TMAP Tübingen; Werner & Dreizler (1999); Werner et al. (2003); Rauch & Deetjen (2003)) was used as the Kurucz model parameter space was inadequate to fit the SEDs of these stars. The free parameters in these models include T_{eff} with range 30000 to 1000000 K, log g ranging from 3.8 to 9, and H, He mass fractions in the range 0 to 1.

To fit SEDs using Kurucz models, the [Fe/H] value was fixed at -1.0 dex, close to the value for the cluster. Additionally, the log g was constrained to range from 3 to 5 for Kurucz models and 3.8 to 6 for the TMAP models. This is the observed range of log g values for stars in pHB evolutionary phases from previous studies (Moehler et al. 2019). The important parameters obtained from SED analysis are tabulated in Table 3.4. The errors in the estimated parameters are derived as half of the step size of the grid around the value of best-fit. For the two stars fitted with TMAP models, the best-fit values of H and He mass fractions, respectively, are 0.7383, 0.2495 for Star 3 and 0.8, 0.2 for Star 32. However, note that SED fitting is not the optimal method to estimate the above parameters. The log g values obtained from the SED fits are not reported as the SED fitting technique does not provide accurate values of this parameter.

Table 3.4: Table showing the results from the SED analysis of UV-bright stars. The second last column shows the number of fitted data points, and in the last column, F stands for FUV, N for NUV, and O for optical.

ID	R.A. (deg)	Decl. (deg)	Model	T_{eff} (K)	ΔT_{eff} (K)	$\frac{L}{L_\odot}$	$\Delta\frac{L}{L_\odot}$	$\frac{R}{R_\odot}$	$\Delta\frac{R}{R_\odot}$	χ^2_{red}	N_{fit}	Phot. used
Star 1	137.96181	-64.84165	Kurucz	27000	500	50.80	0.27	0.33	0.01	7.58	11	F, N, O
Star 2	138.02575	-64.84307	Kurucz	21000	500	352.95	1.53	1.42	0.07	8.21	10	F, N, O
Star 3	138.06046	-64.86146	TMAP	80000	3750	2857.45	0.88	0.28	0.03	3.31	8	F, N, O
Star 4	138.05040	-64.84379	Kurucz	39000	500	781.10	0.95	0.61	0.02	4.51	9	F, N, O
Star 5	138.04719	-64.87492	Kurucz	27000	500	59.54	0.25	0.35	0.01	2.34	10	F, N, O
Star 6	138.06813	-64.86459	Kurucz	12500	125	108.50	1.11	2.20	0.04	6.86	11	F, N, O
Star 7	138.05264	-64.86779	Kurucz	22000	500	85.73	0.44	0.64	0.03	3.36	9	F, N, O
Star 8	138.04842	-64.84887	Kurucz	16000	500	117.20	0.96	1.41	0.09	6.44	10	F, N, O
Star 9	138.04760	-64.85790	Kurucz	17000	500	109.80	0.78	1.21	0.07	3.50	10	F, N, O
Star 10	138.03820	-64.87028	Kurucz	22000	500	106.20	0.62	0.71	0.03	5.78	10	F, N, O
Star 11	137.96088	-64.85092	Kurucz	26000	500	79.93	0.32	0.44	0.02	3.94	9	F, N, O
Star 12	138.02716	-64.86694	Kurucz	25000	500	102.60	0.87	0.54	0.02	0.10	7	F, N, O
Star 13	138.01470	-64.85891	Kurucz	15000	500	128.83	2.02	1.68	0.11	0.09	7	F, N, O
Star 14	138.01349	-64.86046	Kurucz	27000	500	86.65	0.09	0.42	0.02	4.86	7	F, N, O
Star 15	138.01173	-64.86674	Kurucz	26000	500	131.15	0.22	0.56	0.02	1.59	7	F, N, O
Star 16	138.03578	-64.86580	Kurucz	23000	500	54.90	0.04	0.47	0.02	1.39	5	N, O
Star 17	138.03122	-64.85554	Kurucz	25000	500	41.40	0.02	0.34	0.01	8.76	5	N, O
Star 18	138.03010	-64.86050	Kurucz	22000	500	211.00	0.07	1.00	0.05	6.01	5	N, O
Star 19	138.02244	-64.87728	Kurucz	45000	500	633.00	0.10	0.41	0.01	1.33	5	N, O
Star 20	138.01776	-64.87794	Kurucz	27000	500	72.00	0.03	0.39	0.01	1.98	5	N, O
Star 21	138.01103	-64.87463	Kurucz	24000	500	49.30	0.08	0.41	0.02	3.75	5	N, O
Star 22	138.00244	-64.87014	Kurucz	22000	500	102.00	0.69	0.69	0.03	0.02	5	N, O
Star 23	138.00133	-64.86623	Kurucz	50000	500	113.00	0.02	0.14	0.00	4.61	5	N, O
Star 24	137.99932	-64.85673	Kurucz	50000	500	97.80	0.13	0.13	0.00	3.77	5	N, O
Star 25	137.99187	-64.87307	Kurucz	35000	500	56.10	0.18	0.20	0.01	0.33	5	N, O
Star 26	137.99182	-64.85956	Kurucz	27000	500	67.70	0.32	0.38	0.01	0.11	5	N, O
Star 27	137.96443	-64.86377	Kurucz	50000	500	988.00	1.22	0.42	0.01	0.26	5	N, O
Star 28	137.85352	-64.87929	Kurucz	26000	500	65.36	0.97	0.39	0.02	2.58	15	F, N, O
Star 29	137.92453	-64.70158	Kurucz	32000	500	145.80	1.09	0.39	0.01	2.66	15	F, N, O
Star 30	138.08369	-64.84865	Kurucz	25000	500	98.59	1.03	0.52	0.02	2.89	13	F, N, O
Star 31	138.00728	-64.79293	Kurucz	23000	500	251.00	2.12	0.99	0.04	4.49	14	F, N, O
Star 32	137.99974	-64.89071	TMAP	100000	5000	3010.25	1.20	0.18	0.02	9.06	12	F, N, O
Star 33	138.02306	-64.89646	Kurucz	26000	500	53.26	0.51	0.36	0.01	2.39	11	F, N, O
Star 34	138.09187	-64.87727	Kurucz	24000	500	119.91	0.75	0.63	0.03	4.40	11	F, N, O

The SEDs for stars 1 to 11 contain the UVIT (FUV, NUV) and the *HST* (NUV, optical) photometric data points. Stars 12 to 26, lying within the inner region of the cluster, could not be resolved by the UVIT. Hence, only the *HST* photometry was used to construct the SEDs of these stars. Four stars among these, namely, Stars 12, 13, 14, and 15, have the *HST* STIS photometry (FUV, NUV) from Brown et al. (2001) apart from the NUV and optical HUGS data. For stars 27 to 34, which lie outside the *HST* FOV, the UVIT, *GALEX* (Schiavon et al. 2012), *Gaia DR2* and ground-based optical data were utilized for SED generation. Examples of SED fits for star 3 and star 27 are shown in Figure 3.11. The SEDs for the other UVIT-resolved stars are shown in Figure 3.12. The residuals shown in these plots were calculated for each data point as follows :

$$Residual = \frac{F_o - F_m}{F_o} \tag{3.1}$$

where F_o and F_m are the observed and model fluxes corresponding to the photometric points.

Figure 3.13 shows a histogram of the temperature distribution of the UV-bright stars in the cluster. The values take range from 12500 to 100000 K, with the maximum number of stars having a temperature between 20000 to 30000 K.

Figure 3.14 shows the trends in the best-fit parameters of the 18 UV-bright stars with UVIT photometry in the $m_{F154W} - m_{N245M}$ vs. m_{F154W} CMD. The left, middle, and right panels display the trends in T$_{eff}$, luminosity, and radius, respectively. Among the 5 stars with the brightest m_{F154W} magnitudes, the hottest stars are also the most luminous and have the smallest radii. The coolest among these 5 stars have $log(L/L_{\odot}) \sim 2.5$ and $R/R_{\odot} \sim 1.0$. The star with the brightest

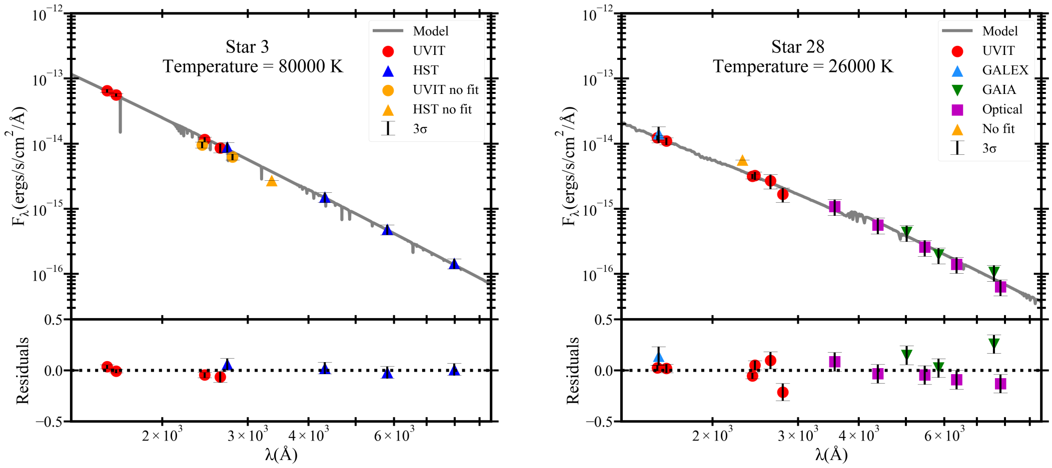

FIGURE 3.11: The SEDs for two of the observed UV-bright stars, namely star 3 and star 28, after correcting for extinction. Star 3 lies in the inner region of the cluster and has photometry from the *HST* and the UVIT. Star 28 lies in the outer region and has photometric data from UVIT, *GALEX*, *Gaia DR2*, and ground-based optical data from Stetson et al. (2019). In both plots, the photometric points excluded from the fitting procedure are shown with orange symbols. The gray line shows the model spectrum. The residuals of the SED fit are shown in the bottom panels of both plots.

m_{F154W} magnitude has log $T_{eff} \sim 4.6$, with a fairly high luminosity ($log(L/L_\odot) \sim 3$) and a smaller radius ($R/R_\odot \sim 0.5$). Most of the remaining pHB stars with m_{F154W} fainter than 15.5 mag have log T_{eff} in the range 4.3 to 4.5, with $log(L/L_\odot) \lesssim 2.2$ and radii $R/R_\odot \lesssim 0.5$. The three coolest stars with $m_{F154W} \sim 16$ mag have $log(L/L_\odot) \sim 2.0$ and are relatively larger in size with $R/R_\odot \gtrsim 1.5$.

In order to evaluate the importance of FUV data points in the estimation of fundamental parameters, the SEDs of Stars 1 to 15 and Stars 28 to 34 were fitted, excluding their available FUV photometric points. It was found that the parameter values changed significantly for stars hotter than T_{eff} = 40,000 K with the underestimation of T_{eff}, L (by upto 60% and 90% respectively) and the overestimation of R (by upto 100%). This implied that FUV data is crucial to estimate the parameters of very hot stars. Hence, the results derived for hot stars without FUV data points are to be considered with lesser weightage.

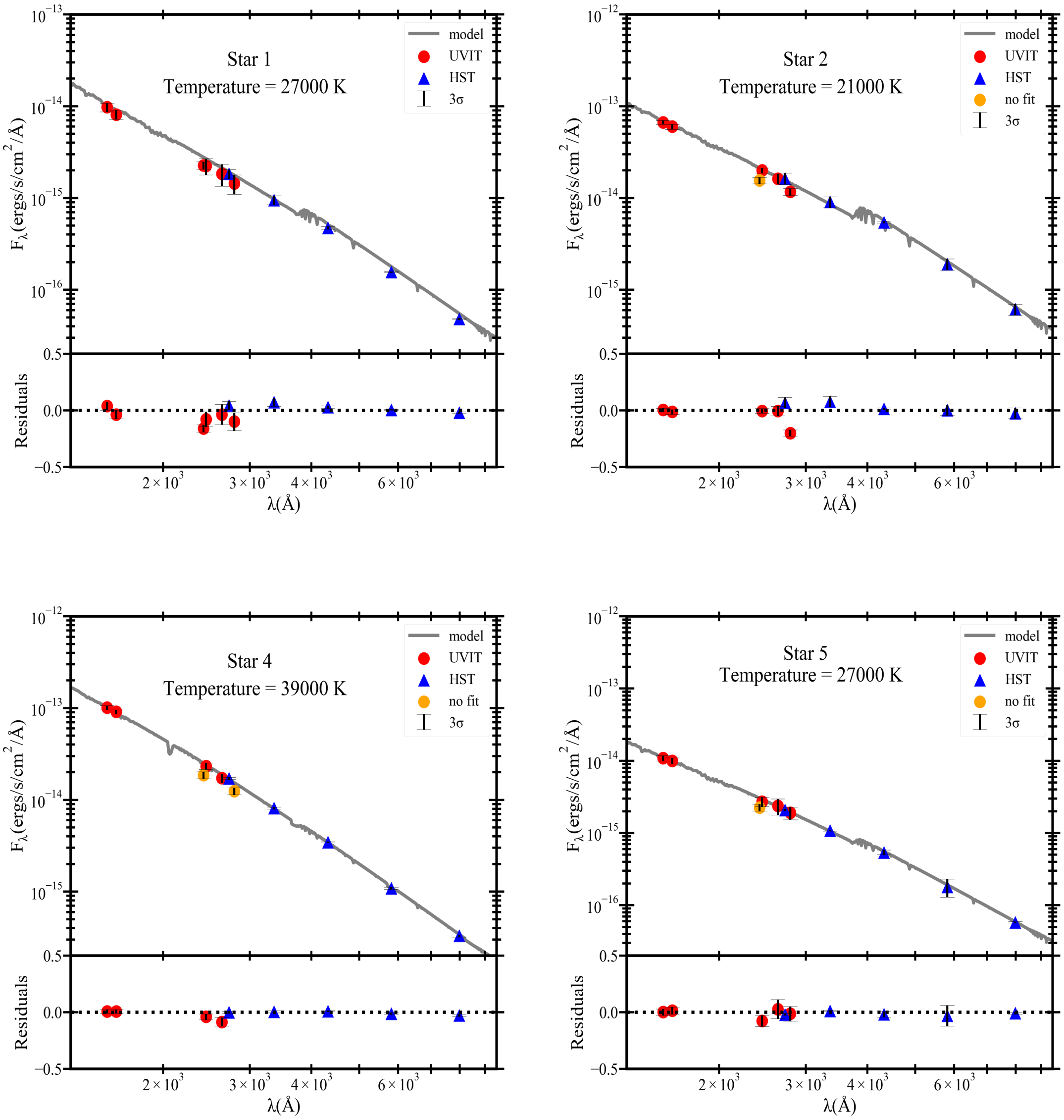

FIGURE 3.12: SEDs for UV-bright stars listed in Table 3.3 except those of Star 3 and Star 28, which are already shown in Figure 3.11.

Since several previous studies (Bedin et al. 2000; Marino et al. 2017) adopted a reddening value of $E(B-V) = 0.19$ mag for this cluster, the SEDs were also fitted using this value to see by what amount the estimated parameter values change. With this reddening measure, it was found that the effective temperature values decreased by 10 (e.g., in the case of the hottest star) to 20%, the bolometric luminosities decreased by about 20 to 30%, and the radii increased by about 5 to 10%.

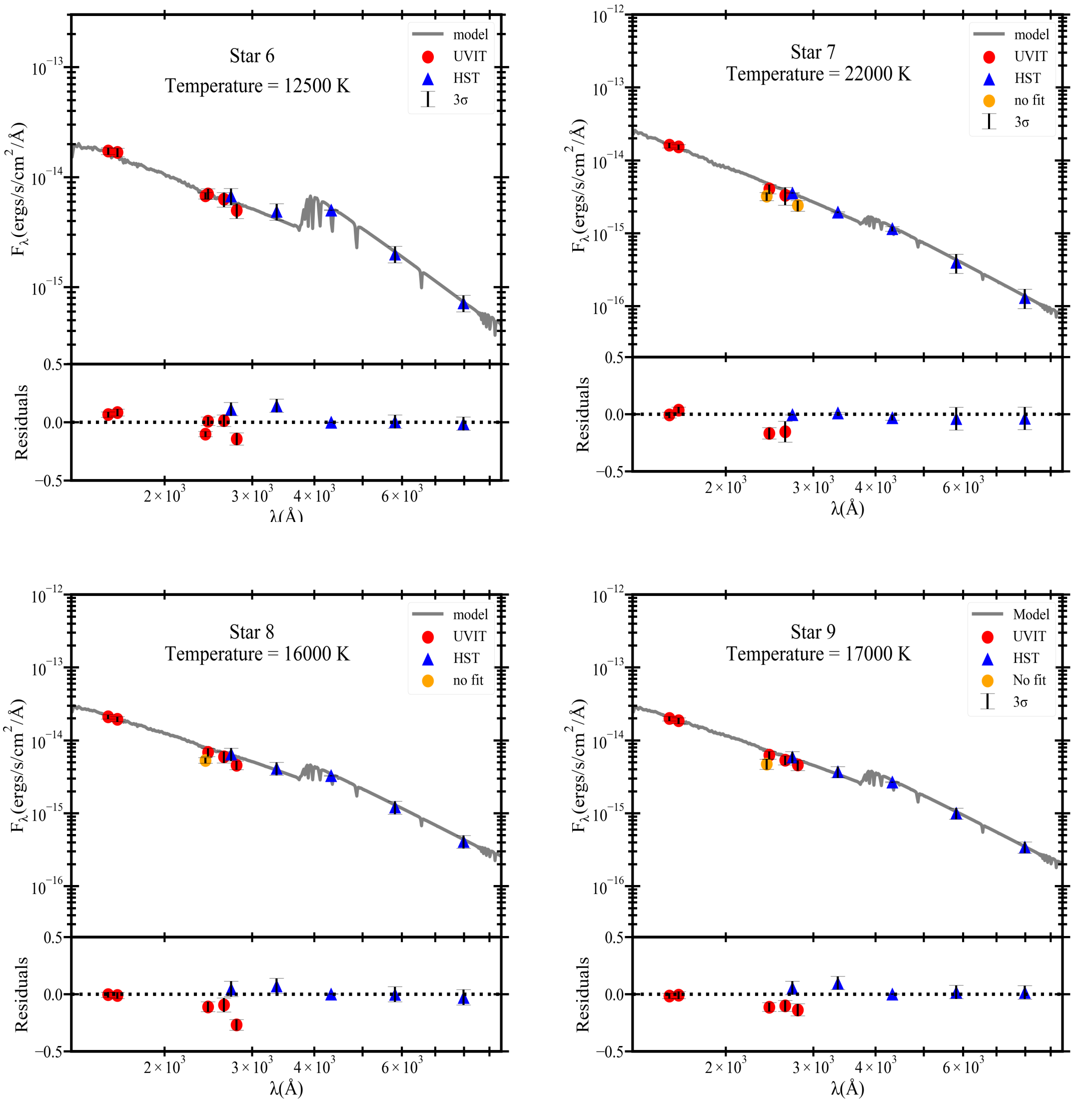

FIGURE 3.12: (continued.)

3.6 Evolutionary Status Of UV-Bright Stars

The luminosities and temperatures derived from SED analysis were used to assess the evolutionary status of the observed UV-bright stars using the H-R diagram. The pHB evolutionary tracks from Moehler et al. (2019), based on the calculations of Miller Bertolami (2016), were employed. The tracks correspond to [M/H] = −1 dex, and zero-age main-sequence (ZAMS) mass of $M_{ZAMS} = 0.85\ M_\odot$ (age = 12

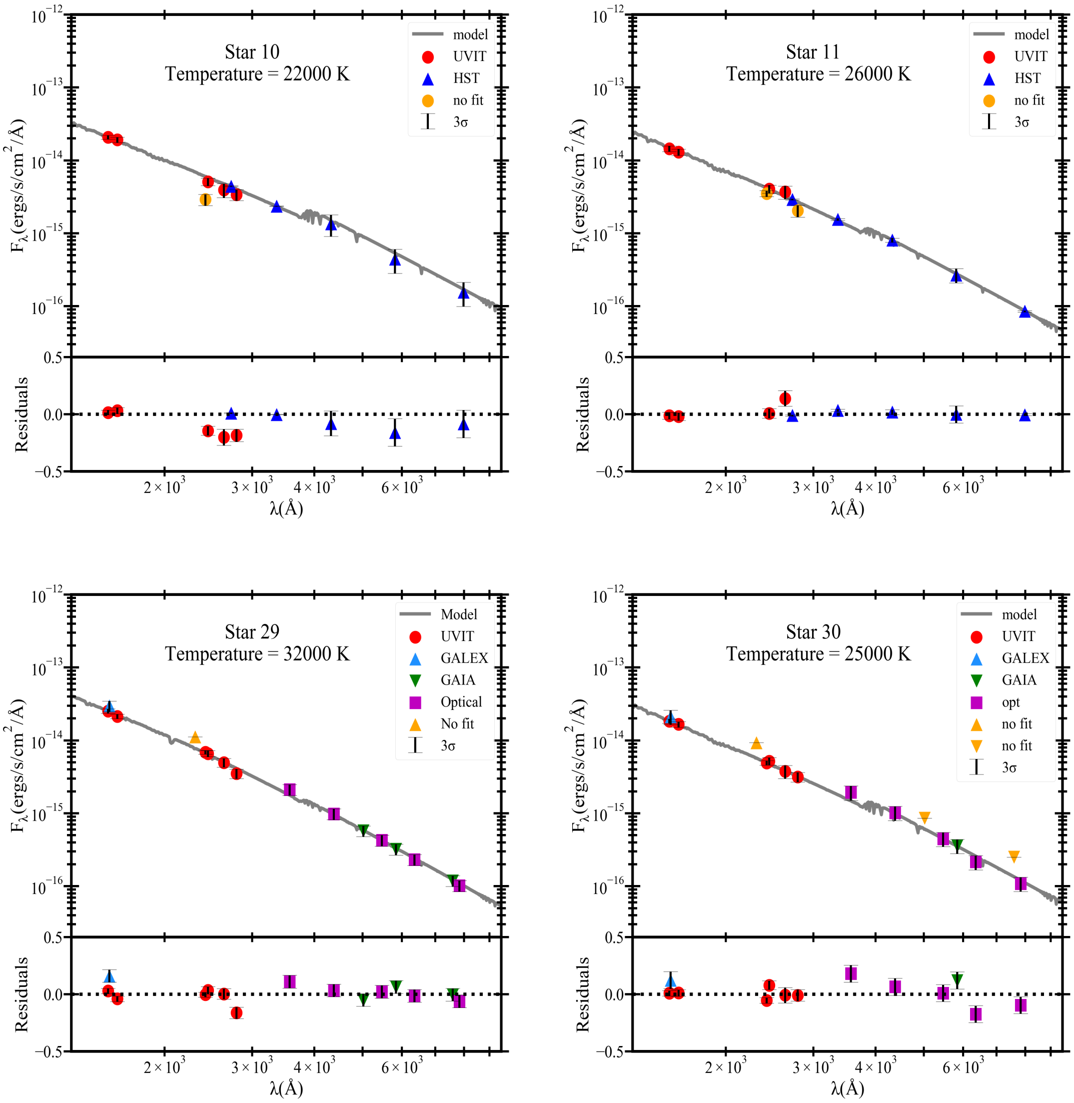

FIGURE 3.12: (continued.)

Gyr) assuming scaled-solar metallicity with initial abundances $Z_{ZAMS} = 0.00172$, $Y_{ZAMS} = 0.24844$, and $X_{ZAMS} = 0.74984$. In the models, the RHB, BHB, and EHB sequences were populated by regulating the mass-loss on the RGB phase.

Figure 3.15 shows the observed UV-bright stars in black (inner region) and magenta (outer region) inverted triangles plotted over the evolutionary tracks. It is evident from this figure that all the UV-bright stars, except the three most luminous ones, have evolutionary masses $< 0.53\ M_\odot$. Most of these stars are observed

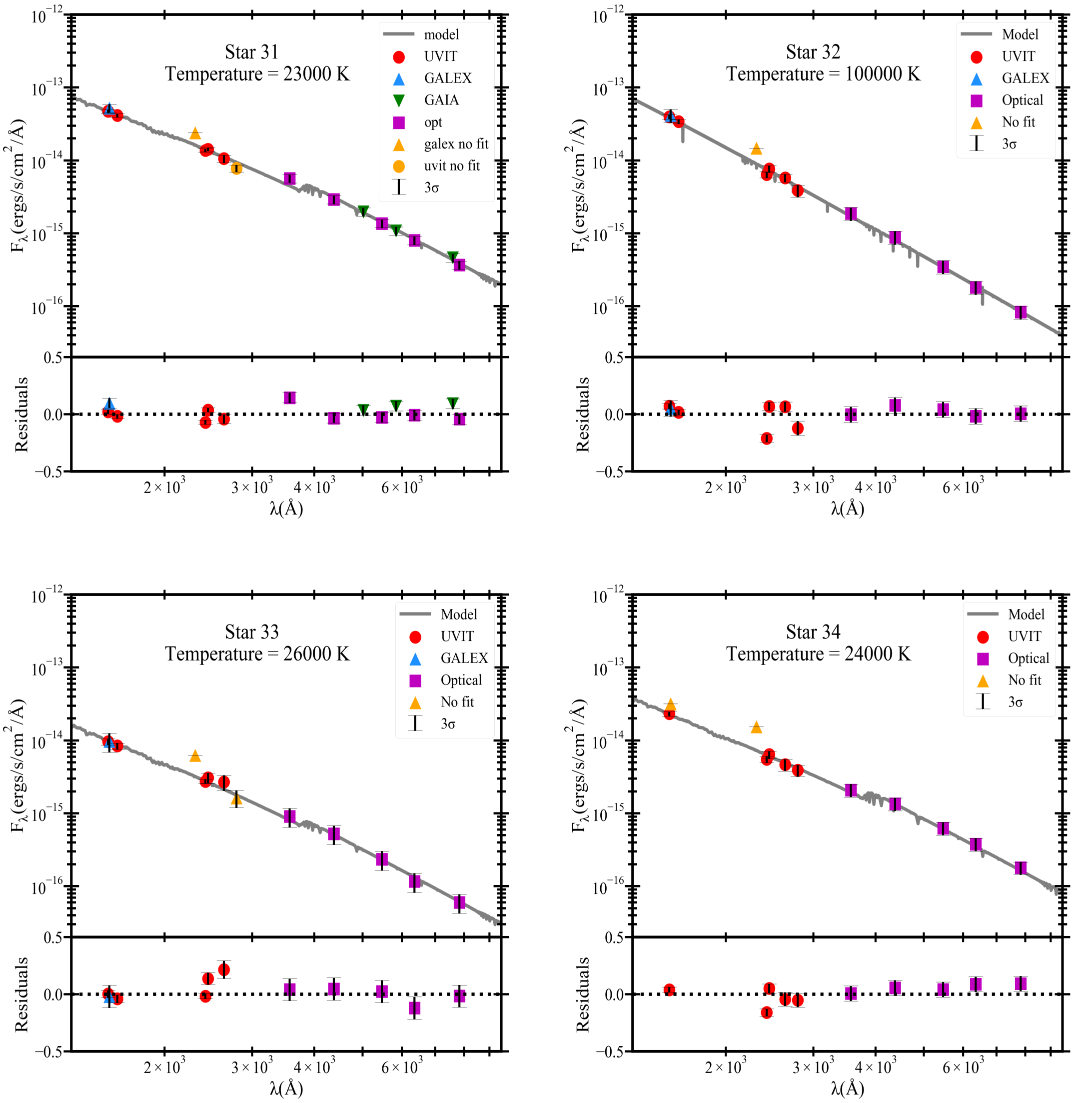

FIGURE 3.12: (continued.)

to lie along/near the sequence with $M_{ZAHB} = 0.5\ M_\odot$, which is a track evolving from the EHB phase. These are likely to be AGB-manqué stars, which directly descend the WD cooling sequence after core-He exhaustion. The hottest and the most luminous UV-bright star (Star 32 in Table 3.4) is located between the tracks with $M_{ZAHB} = 0.75\ M_\odot$ and $0.85\ M_\odot$. Star 3, with slightly lower luminosity and T_{eff}, lies at the intersection of two post-RHB sequences with $M_{ZAHB} = 0.65\ M_\odot$ and $0.75\ M_\odot$. From the models, the mass of this star then ranges from $0.527\ M_\odot$ to $0.544\ M_\odot$. Two stars (Star 23 and Star 24) are found to be located outside the

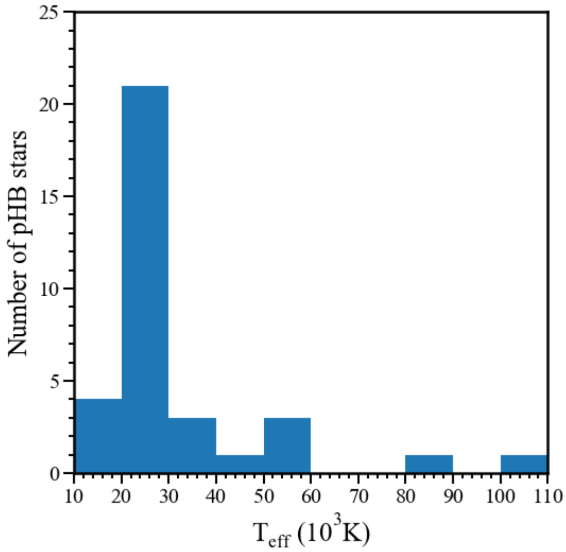

FIGURE 3.13: Histogram showing the temperature distribution of UV-bright stars in NGC 2808

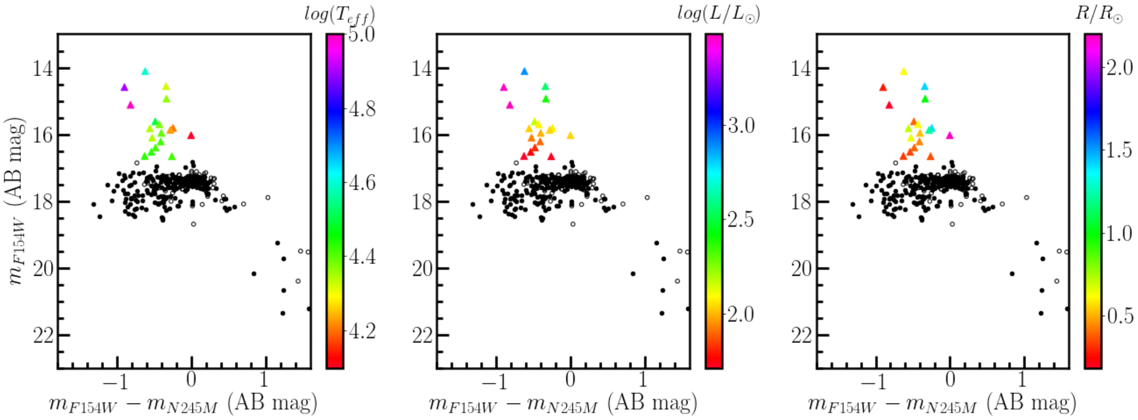

FIGURE 3.14: The trends in the best-fit parameters (effective temperature, bolometric luminosity, and radius) of the 18 UV-bright stars having UVIT photometry shown in the $m_{F154W} - m_{N245M}$ vs m_{F154W} CMD.

range of the model tracks.

Moehler et al. (2019) considered the area defined by $log(L/L_{\odot}) > 2.65$ and $4.9 > \log T_{eff} > 3.845$ in the H-R diagram (region shaded in gray in Figure 3.15) to be corresponding to hot UV-bright p(e)AGB stars. Going by their definition, from Figure 3.15, three stars can be seen to lie inside this region and one star on the

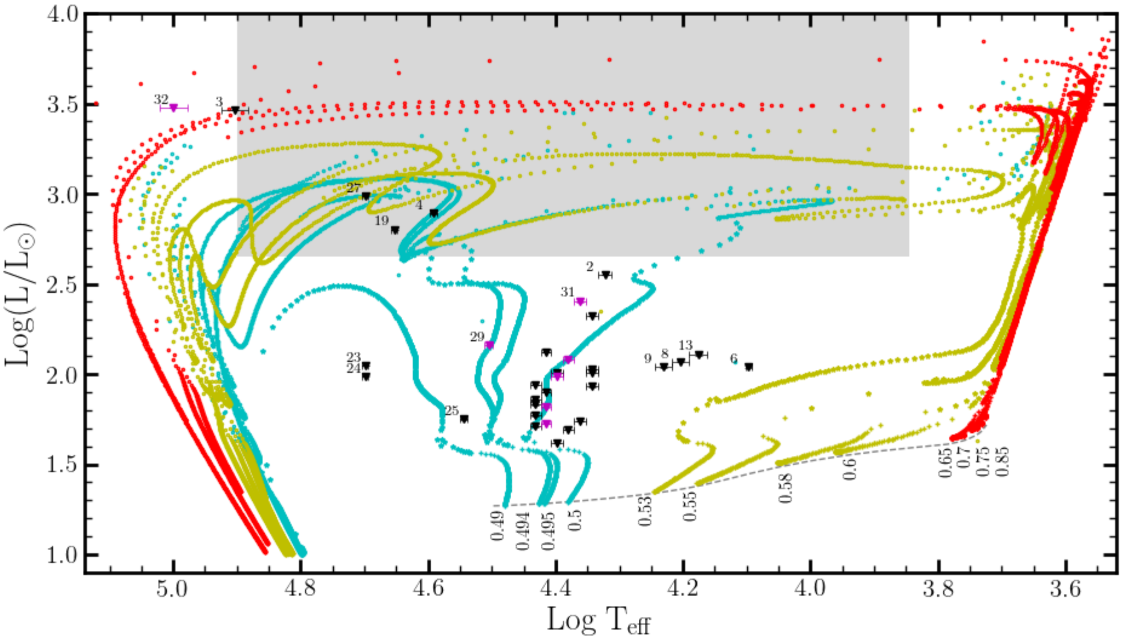

FIGURE 3.15: Stellar evolutionary tracks starting from ZAHB (Moehler et al. 2019). Red, olive green and cyan colors represent sequences evolving from the RHB, BHB, and EHB, respectively. The + symbol indicates HB location and is plotted after every 1 Myr. The stars and circles represent pHB evolution and are plotted with time steps of 0.1 Myr and 1 kyr, respectively. The value indicated below each sequence represents the mass at the ZAHB for the particular sequence, M_{ZAHB}, in units of $M_\odot$. The gray region marks the domain of hot p(e)AGB stars. The gray dashed line represents the BaSTI ZAHB model. The observed UV-bright stars are plotted with black (located within the inner region of the cluster) and magenta (outer region) symbols with error bars. The numbers marked close to some of the sparsely located stars indicate their IDs from Table 3.4.

high-temperature boundary. Among these three stars which are inside the gray-shaded region, two (Star 4 and Star 19) are quite unlikely to be p(e)AGB stars as they are located close to the evolutionary track with $M_{ZAHB} = 0.494\ M_\odot$. The remaining star (Star 27) occupies a position where post-EHB (cyan) and post-BHB (olive green) sequences overlap, making it difficult to distinguish. Hence, only the hot and luminous star (Star 3) seen on the boundary of the shaded region can be confirmed as a hot p(e)AGB star. In other words, the cluster has a maximum of 2 and a minimum of 1 detected hot p(e)AGB candidate as per the above definition. One star (star 32) hotter than the hot boundary of the shaded region is detected.

This star might have crossed the p(e)AGB stage and is probably evolving toward the WD stage.

3.6.1 Comparison Of Theoretically Expected And Observed Numbers Of Hot p(e)AGB Stars

Now, a comparison of the observed number of hot p(e)AGB stars with the number of such stars anticipated from theoretical predictions can be made. For this, the evolutionary flux method described in detail in Greggio & Renzini (2011) is applied. The following suppositions are made in this calculation: a) GCs are simple stellar populations (SSPs), b) the rate at which stars end up as remnants is equal to the rate at which stars leave the main sequence, c) the lifetimes of later stages of stellar evolution are considerably shorter than that of main-sequence evolution. Under this premise, the number of stars, N_i, in a particular stage of evolution, i, in a SSP is given by the relation,

$$N_i = B(t) \times L_{total} \times t_i \tag{3.2}$$

Here, *B(t)* is the specific evolutionary flux, which is the number of stars entering (or exiting) a certain phase of stellar evolution per year per luminosity ($L_\odot$) of the sampled population; L_{total} is the total luminosity of the stellar population and t_i is the duration of the evolutionary phase being analyzed. Assuming an age $\sim$ 10 Gyr for the cluster and Salpeter's IMF, an approximate value for specific evolutionary flux can be obtained empirically as $B \simeq 2 \times 10^{-11}$ stars per year per $L_\odot$ (See Greggio & Renzini 2011 for details).

In this analysis, stars in the hot p(e)AGB phase of evolution are considered, which corresponds to the gray-shaded region in Figure 3.15. Each evolutionary track spans a duration, t, in this region. In order to estimate the expected number of hot p(e)AGB stars from Eq. 3.2, the parameters for NGC 2808 listed in Table 3.5 are used. The anticipated number of p(e)AGB stars in a cluster depends on how frequently a particular evolutionary track is followed in that cluster, which in turn depends on the fraction of stars in various parts of the HB. The number of p(e)AGB stars evolving along all the evolutionary tracks starting from each branch of HB, i.e., N^{RHB}, N^{BHB} & N^{EHB} for stars evolving from RHB, BHB, and EHB respectively can be calculated using Eq. 3.2 (Moehler et al. 2019). For this, the fractions of RHB, BHB, and EHB stars with respect to the total number of HB stars in the cluster (f_{RHB}, f_{BHB} and f_{EHB}) are derived by combining the members from the HUGS and *Gaia DR2* catalogs for complete spatial coverage. The values thus obtained are $f_{RHB} = 0.47$, $f_{BHB} = 0.35$ and $f_{EHB} = 0.07$. The final expected number of hot p(e)AGB stars in the cluster is then,

$$N = (f_{RHB}.N^{RHB}) + (f_{BHB}.N^{BHB}) + (f_{EHB}.N^{EHB}) \tag{3.3}$$

A range for N is obtained since N^{RHB}, N^{BHB} and N^{EHB} take a range of values depending on the duration in the p(e)AGB phase along each evolutionary track. Thus, for NGC 2808, the expected number of hot p(e)AGB in the gray-shaded region of the H-R diagram is estimated as 1.27 to 3.80. The maximum observed number of p(e)AGB stars detected in this shaded region is 2, which is in good agreement with the expected number of such stars.

TABLE 3.5: Parameters for NGC 2808

Parameter	Value	Source
[Fe/H]	−1.14 dex	H96
Age	10.9 Gyr	Massari et al. (2016)
Integrated V magnitude, V_t	6.20 mag	H96
Distance modulus, $(m - M)_V$	15.59 mag	H96
Reddening, $E(B-V)$	0.22 mag	H96
Bolometric correction, BC_V	−0.45 mag	Worthey (1994)

3.7 Discussion

In this work, the identification and characterization of the sample of UV-bright member stars in NGC 2808 are carried out using the photometric data from the UVIT, in combination with *HST*, *Gaia DR2*, and ground observations. The detection of these stars is extremely important to build a statistically significant sample that can aid in understanding the late phases of evolution of low-mass stars and determining their contribution to the UV luminosity of old stellar systems. As highlighted earlier, observations in the UV wave bands are critical for this purpose. The UV−optical and UV CMDs constructed by combining the UVIT data with the *HST* (inner $2\mathrm{!}7 \times 2\mathrm{!}7$ region of the GC), *Gaia DR2* and ground-based optical data (outside *HST* FOV) reveal the sequences of hot members in the cluster. The UVIT data for stars within the innermost $1'$ diameter region is not used because of the possible effects of crowding. In the FUV filters, mainly the pHB, BHB, EHB, BHk, and BSS populations are detected, whereas, in the NUV filters, the cooler RHB stars can also be spotted additionally. The identification of HB location is supported by the overlaid ZAHB and TAHB models.

Brown et al. (2001) observed the central $\simeq 1750$ arcsec^2 region of NGC 2808 using *HST* STIS FUV/F25QTZ and NUV/F25CN270 filters. Although a direct comparison cannot be made between their and our UV CMDs (due to the differences in the filter characteristics and the FOV covered), some general features of the CMDs can be examined in detail. In their FUV−NUV vs. FUV CMD, a gap between BHB and EHB was found at FUV−NUV color ~ -1 mag. They also found a sparse sub-luminous population of stars below the end of canonical ZAHB and explained them by invoking the late-hot flasher (BHk) scenario, having enhanced He and C abundances due to flash mixing. The spread in the magnitudes of these stars was accounted for by the evolution of BHk stars to higher luminosities as the He-core burning progressed. A similar spread is found in the BHk magnitudes in the $m_{F154W} - m_{N245M}$ vs. m_{F154W} CMD shown in Figure 3.8. Brown et al. (2001, 2010a) noted that some of these BHk stars are unusually redder, i.e., redder than expected from the models for normal BHk or EHB stars. A similar dispersion in the color of BHk stars is observed in the FUV−NUV vs. FUV CMD. Brown et al. (2012) analyzed the UV spectra of two BHk stars with redder FUV−NUV colors and found that there is a large enhancement of Fe-peak elements in these stars, which could serve as an explanation for their observed colors.

Brown et al. (2012) also discussed the results from UV spectral analysis of 3 unclassified objects, U1, U2, and U3, which are hotter than their canonical HB model. Based on their spectra and locations in the UV CMD, the possibilities of them being evolving pAGB stars or WDs were disregarded. U1 and U2 were found to have implausible effective temperatures ($\sim$ 250,000 K) and U3 to have $T_{eff} =$ 50,000 K. These objects did not have any X-ray counterparts. The authors were unable to conclusively explain these unusually hot objects, although propositions such as the presence of accretion disk in the objects, change in extinction along the line of sight to the cluster, non-stellar source, etc., were put forth. These objects, located within $30''$ from the cluster center, are not resolved in the UVIT images. However, two of these objects, namely, U1 and U3, could be cross-matched with stars in the HUGS catalog having membership probability $> 90\%$. These are found in the BHk and EHB positions respectively in the $m_{F275W} - m_{F438W}$ vs. m_{F336W} CMD shown in Figure 3.3. Similar objects are detected in the UV CMDs in Figure 3.8 with bluer $m_{F154W} - m_{N245M}$ colors ($\lesssim -1$ mag) than the ZAHB model and roughly the same magnitudes as that of the HB.

The study by Schiavon et al. (2012) did not include the full sample of pHB stars in NGC 2808. There are 22 candidates in their list of UV-bright stars in NGC 2808. About 15 stars are found to be common between this sample and theirs.

The UV CMD presented in Brown et al. (2001) shows one pAGB candidate star with FUV magnitude 12.46 mag. This star is unresolved in the UVIT images and not included in the HUGS catalog as it is saturated in the WFC3/UVIS filters. Hence, the analysis does not include this star. Brown et al. (2001) also found 5 pHB candidates from the UV CMD, of which 4 stars are common with our catalog. The fifth pHB candidate is not included in the HUGS catalog, and hence, its membership cannot be assessed even though it is detected in the UVIT images (R.A. = 138.0235°, Decl. = −64.86531°).

In Table 3.6, the estimates of T_{eff} from this work are compared with the values available in the literature for three UV-bright stars in the cluster. Brown et al. (2012) derived the T_{eff} for the AGB-manqué star AGBM1 using the *HST* STIS UV spectrum. Moehler et al. (2019) estimated the T_{eff} values for the stars C4594 and C2946 using the medium-resolution optical spectra from the EFOSC2 instrument at the 2.2m MPI/ESO telescope. From the table, it is evident that the T_{eff} values derived through SED analysis are in close agreement with spectroscopic estimations.

Moehler et al. (2019) calculated the theoretically expected numbers of hot p(e)AGB

Table 3.6: Table showing the comparison of T_{eff} values derived by us through SED analysis with those available in the literature for 3 UV-bright stars. The errors quoted in the T_{eff} values are estimated as half the model grid step, around the best-fit value, during the SED fit. The first column shows the ID of the stars from Table 3.4.

ID	ID in literature	T_{eff} from literature (K)	T_{eff} from our analysis (K)	Reference
Star 13	AGBM1	14500	15500 ± 500	Brown et al. (2012)
Star 31	C4594	19900 ± 1600	23000 ± 500	Moehler et al. (2019)
Star 34	C2946	24900 ± 1800	24000 ± 500	Moehler et al. (2019)

stars in 17 galactic GCs (excluding NGC 2808) and compared them with the observed numbers. The numbers matched more or less in the case of 14 clusters. In the remaining 3 clusters, the observed numbers of p(e)AGB stars were larger than the predicted values. The massive and dense GC, NGC 5139 (ω Centauri), has the maximum number of observed p(e)AGB stars (5 stars), with the expected number in the range of 1.3 - 13.5. Here, the number of such stars is found to be between 1 and 3 (including the saturated pAGB candidate from Brown et al. (2001)), which agrees well with the expected number for NGC 2808.

The pHB stars identified in this study will provide a good sample to explore the stellar evolutionary properties in this phase. From Figure 3.9, it can be seen that there are seven member stars present in the outer extent of the cluster that are ideal candidates for further follow-up spectroscopic studies. These are identified from the *AstroSat*/UVIT images and are in relatively less crowded regions of the cluster. This GC is known to host populations with a wide range of main-sequence He abundances (Piotto et al. 2007; Milone et al. 2015). In addition, many of the UV-bright stars with $T_{eff} > 25{,}000$ K are likely to experience gravitational settling and/or weak winds, which may alter their surface helium (and metal) abundance (e.g., Dixon et al. (2017)). These abundance uncertainties call for a thorough spectroscopic investigation. Moreover, spectroscopy can provide accurate estimation of T_{eff}, log g, radial velocity and its variation (if any), detailed chemical abundance information on the signs of third dredge-up (which will help to distinguish between peAGB and pAGB phases clearly), and so on.

3.8 Summary

The results of this chapter are summarized below:

1. A comprehensive study of the UV-bright member stars in the GC NGC 2808 was performed using the *AstroSat*/UVIT, *HST*, *Gaia DR2*, and ground-based optical data. The identification and detailed study of these stars are important to create a statistically significant sample for two main reasons : (i) to throw light on the rapid evolution of late phases of low-mass stars such as pAGB, peAGB, and AGB-manqué phases, (ii) to assess the contribution of these stars to the total UV output of old stellar systems.

2. Member stars in the cluster were identified to create optical, UV-optical, and UV CMDs. The stars in the HB sequence were identified and compared with the ZAHB and TAHB models. Several hot HB stars were detected along with a FUV-bright BSS. These will be studied in detail in the future.

3. About 34 UV-bright stars were detected based on their locations in the UV CMDs. Among these, 27 stars were found to be located within the inner $2.'7 \times 2.'7$ region of the cluster and 7 stars in the outer region.

4. Stellar parameters such as $T_{\textit{eff}}$, $R/R_{\odot}$ and $L/L_{\odot}$ were estimated through SED fitting technique. Their effective temperatures range from 12500 K to 100,000 K, luminosities from $\sim$ 40 to 3000 $L_{\odot}$ and radii from 0.13 to 2.2 $R_{\odot}$. The $T_{\textit{eff}}$

estimations from SED fitting reported in this work were found to match well with the available spectroscopic estimations for a few stars from the literature.

5. By comparing the derived parameters with theoretical models available for evolved stellar populations, the evolutionary status of these stars was probed. Most UV-bright stars were observed to have evolved from EHB stars with M_{ZAHB} = 0.5 $M_{\odot}$, and these are in the AGB-manqué phase. From the theoretical models, it was observed that all except the three hottest and the most luminous UV-bright stars have HB progenitors with $M_{ZAHB} < 0.53$ $M_{\odot}$.

6. The expected number of hot p(e)AGB stars in NGC 2808 is estimated from stellar evolutionary models and is found to agree well with the observed number.

7. Seven pHB stars identified in the outer region are ideal for further spectroscopic follow-up studies. These stars are identified from the *AstroSat*/UVIT images. This work thus demonstrates the capability of the UVIT in detecting and characterizing UV-bright stars.

Chapter 4

UV Properties of Variable Extreme Horizontal Branch Stars in NGC 2808[†]

4.1 Introduction

A recent study by Momany et al. (2020) utilizing NUV and optical data led to the discovery of variable stars among the EHB population (vEHB) in three Galactic GCs, namely, NGC 2808, NGC 6752, and NGC 5139 (ω Centauri). Momany et al. (2020) reported two types of EHB variability, periodic (periodicity of ~ 2 to 50 days with $\Delta\ U_{Johnson} \approx 0.04$ to 0.22 mag) and aperiodic. This EHB variability was observed to be tightly connected with the photometric jump at $T_{eff} \sim$ 22,500 K (the Momany jump, Momany et al. (2002)), a feature observed in all GCs (Momany et al. 2004; Brown et al. 2016). Through appropriate analyses and arguments, binary evolution or pulsation were discarded as reasons for the variability.

[†] Results of this work are published in Prabhu et al. (2021b).

The origin of both modes of EHB variability was attributed to the α^2 Canum Venaticorum (α^2 CVn) phenomenon. In this scenario, chemical inhomogeneities on the stellar surface cause spatial variations in opacity, resulting in spots that are stabilized for a long time (several decades) by an underlying magnetic field. The projected rotation of these magnetic spots causes photometric/spectroscopic variability. The magnetic spots caused by the α^2 CVn phenomenon are expected to be dark in the FUV and bright in the optical wavebands (Mikulášek et al. 2019), resulting in the vEHBs being fainter in FUV, depending on the spot properties and showing higher variability in the FUV. Understanding the FUV properties of EHB stars as a function of their rotation will help in throwing more light on the above hypothesis for variability among EHB stars, in particular, and our overall understanding of EHB stars, in general. Moreover, observing such hot stars in the UV is advantageous because the contribution from cooler stellar populations, such as MS and RGB stars, gets suppressed, thereby considerably reducing the stellar crowding in the central regions of GCs, where many of the EHB stars are located.

This chapter deals with the FUV and NUV photometric analysis and SEDs of 12 vEHB stars and 3 vEHB candidates newly discovered in the GC NGC 2808 by Momany et al. (2020).

4.2 Spotted EHB Stars

The same datasets of NGC 2808 as in Chapter 3 were utilized for this work. The 12 vEHB stars and the 3 vEHB candidates (vEHB-C) from Momany et al. (2020) were cross-identified in the UV catalog. Note that some of these vEHB stars did not meet the membership-probability cut-off. Nevertheless, these were included in the study, as they are analyzed by Momany et al. (2020), and this is a follow-up study of their objects.[*] Figure 4.1 shows the spatial locations of these vEHBs (including candidates) marked over the UVIT F154W image. The stars within the inner region, covered by the *HST* WFC3/UVIS, are encircled in blue, and the other stars in red. It is important to note that only one of the vEHBs located in the inner region (vEHB-7) is affected by neighbor contamination in the UVIT images. Hence, the UVIT data are not used for further analysis of this star.

4.2.1 vEHBs In FUV-Optical CMD

Figure 4.2 shows the $m_{F154W} - m_{F606W}$ vs m_{F154W} CMD for the cross-matched stars. The HB sequence of the CMDs is overlaid with the updated BaSTI theoretical ZAHB and TAHB models from Hidalgo et al. (2018). These models correspond to metallicity [Fe/H] $= -0.9$ dex, He abundance $= 0.249$, solar scaled $[\alpha/\mathrm{Fe}] = 0.0$, and no convective overshoot. The models also account for the effects due to atomic diffusion. The different classes of HB stars (BHk, EHB, BHB), B gap objects, pHB stars, and the BSSs are indicated with distinct colors.

In the figure, the vEHB stars are shown with black star symbols and the candidates with red diamonds. Note that vEHB-7 is not included in this plot for the reason mentioned earlier. One vEHB (vEHB-10) is seen to be located just above the TAHB sequence. This star, along with vEHB-7 have been previously identified as pHB candidates by Prabhu et al. (2021a) with vEHB-7 corresponding to Star 21 and vEHB-10 corresponding to Star 33 in their catalog. One of these stars (vEHB-10) is also listed as an AGB-manqué star (NGC 2808-594) in the study by Schiavon et al. (2012).

---

[*] The study by Momany et al. (2020) did not include cluster membership consideration.

In the CMD, several EHB stars are observed to be sub-luminous with respect to the ZAHB. About half of the vEHB stars belong to this sub-luminous EHB population.

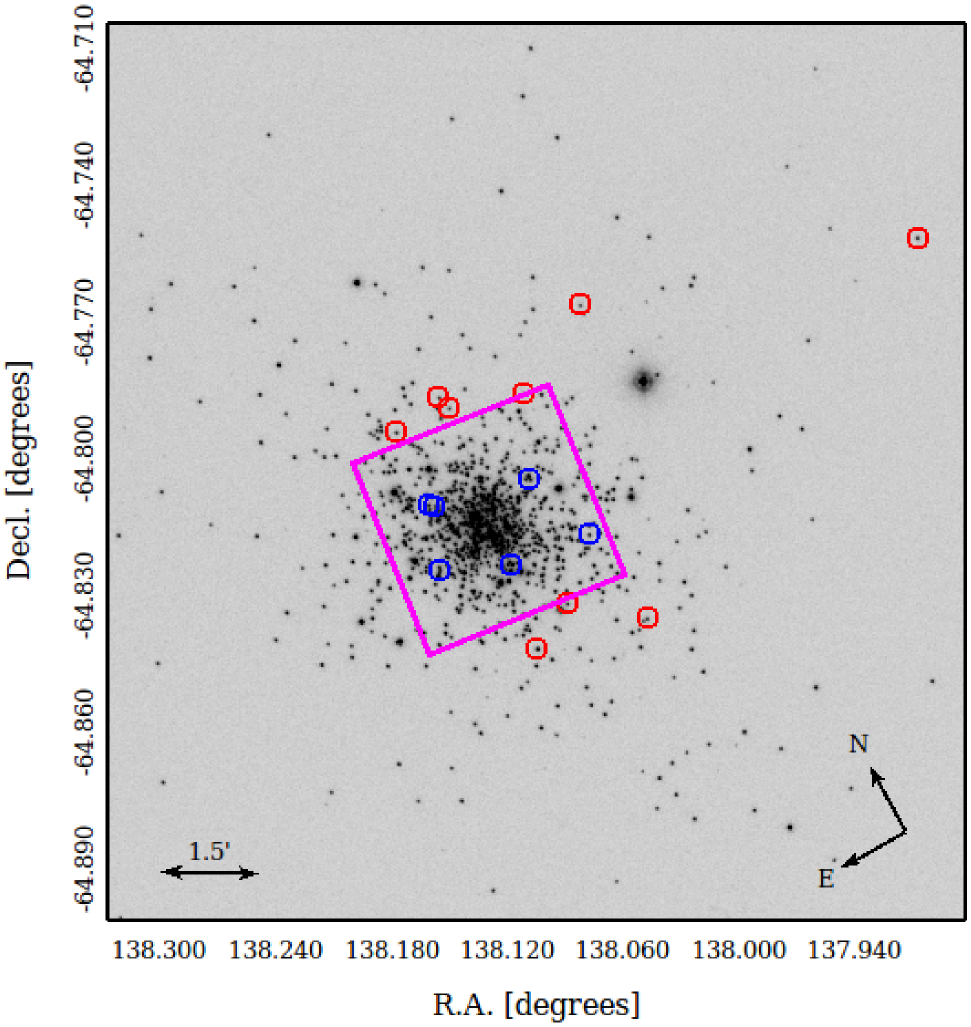

FIGURE 4.1: The vEHB stars marked over the UVIT F154W image of NGC 2808. The magenta region marks the central $\sim 2.7' \times 2.7'$ region (inner region) covered by *HST*, and the stars within this region are encircled in blue. The stars lying in the outer region are encircled in red.

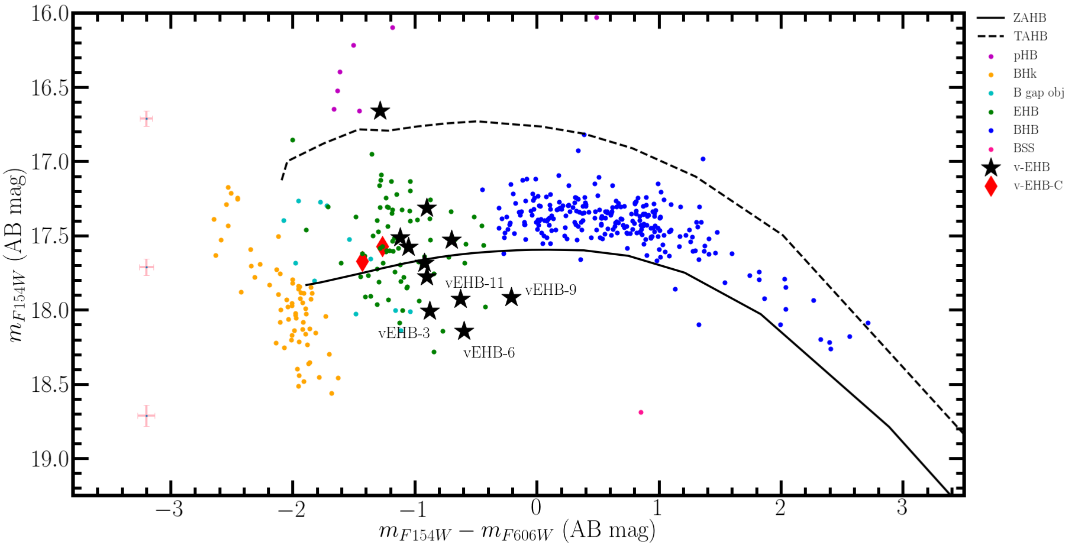

FIGURE 4.2: The $m_{F154W} - m_{F606W}$ vs. m_{F154W} CMD for the cluster member stars common in F154W UVIT filter and other catalogs (HUGS and ground-based optical data). The black solid and dashed lines represent the BaSTI ZAHB and TAHB models with [Fe/H] = −0.9 dex, respectively. The photometric errors in magnitude and color are also shown along the left side of the plot. The 4 faintest vEHB stars are annotated.

4.2.2 Correlation Between UV Magnitudes And Periods Of vEHBs

To check whether any correlation exists between the UV magnitudes and periods of these vEHBs, these quantities were plotted against each other in Figure 4.3. The periods of these stars are obtained from Momany et al. (2020). The following can be noted from the figure: in general, stars with the longest periods are fainter in the FUV and NUV. There is a tentative correlation between period and FUV magnitudes (F154W and F169M), and also within errors in the NUV magnitudes (N242W, N245M, N263M, and N279N) such that longer period stars are fainter in the UV, except for two stars, which deviate from this trend. That is, among the 4 stars that are UV faint and found below the ZAHB (vEHB-3, vEHB-6, vEHB-9, and vEHB-11), vEHB-3 and vEHB-6 have longer periods, whereas the other two have short periods. This is noticed in all the sub-plots shown in Figure 4.3.

Therefore, from the figures, even though a tentative correlation is noticeable, it is not appropriate to make a definite correlation.

In order to further understand this aspect and to explore the correlations (if any) between the fundamental parameters of vEHBs and their periods, their SEDs were generated as explained in the next section.

4.3 Spectral Energy Distributions

The available multi-wavelength photometric data for the vEHB stars were exploited to construct their SEDs and derive parameters such as T_{eff}, luminosity (L), and radius (R) as described in Chapter 2.

For the vEHB stars located within the central $\sim 2.7' \times 2.7'$ area of the cluster, the UVIT and HUGS data were utilized to generate the SEDs. In the case of stars located outside this region, the UVIT data were used in combination with $UBVRI$ photometry from Stetson et al. (2019) and other available VO photometric data from VOSA. The Kurucz models (CK03) were used to fit the SEDs. The free parameters in these models are: log g with a range 0.0 to 5.0 dex, [Fe/H] with a range -2.5 to 0.5 dex and T_{eff} ranging from 3500 to 50 000 K. In order to fit the SEDs with these models, the value of [Fe/H] was fixed at -1.0 dex, close to the value for the cluster. The best-fit parameters derived from the SED analysis for these stars are tabulated in Table 4.1. The parameter errors quoted in the table were derived as half of the step size of the grid around the value of best-fit. The best-fit log g values are not tabulated as SED analysis does not give accurate values of this parameter. Figure 4.4 shows examples of SED fits for vEHB-1 and vEHB-6 with fit residuals.

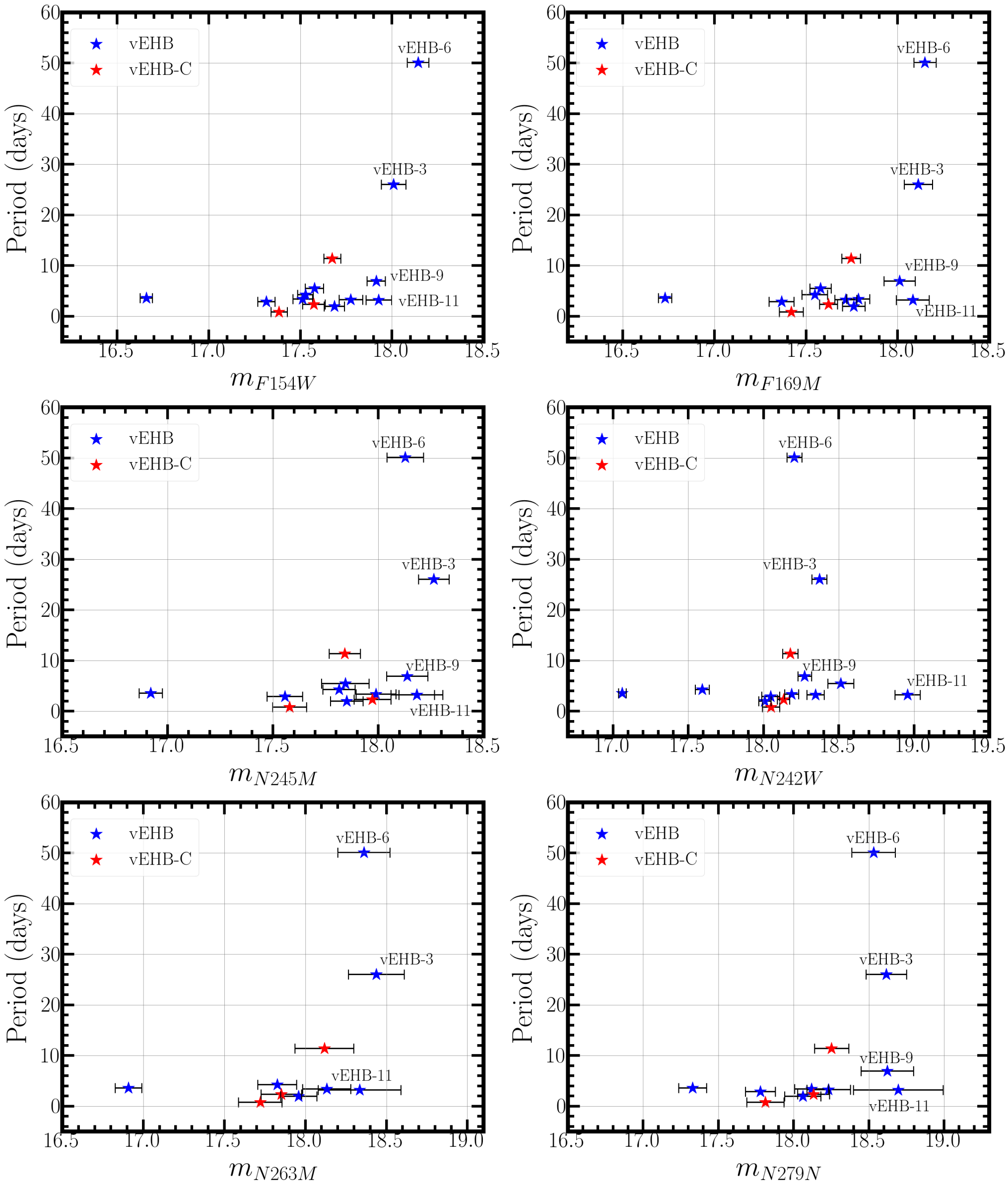

FIGURE 4.3: The magnitudes (extinction corrected) of vEHB stars, along with their photometric errors in different UVIT filters, plotted against their periods from Momany et al. (2020). In the filters N263M and N279N, not all vEHBs are detected. The star vEHB-7 is excluded because it is affected by neighbor contamination. The IDs of the four stars with the faintest UV magnitudes are marked.

Table 4.1: Table with the results of SED fitting procedure for the 15 vEHBs in the cluster. The second last column shows the spatial location (S.L.) of the stars where 'inner' stands for the star lying within the HST FOV and 'outer' stands for the star lying outside this region. The membership probability (M.P.) of each star is indicated in the last column.

ID$^{(a)}$	Period$^{(a)}$ (days)	T_{eff} (K)	$\frac{L}{L_\odot}$	$\frac{R}{R_\odot}$	χ^2_{red}	N_{fit}	S.L.	M.P. (%)
vEHB-1	3.38683880	21000 ± 500	20.56 ± 0.19	0.34 ± 0.02	7.05	8	I	97.3
vEHB-2	5.47704961	22000 ± 500	22.11± 0.11	0.32 ± 0.01	2.09	8	I	97.3
vEHB-3	26.01823489	21000 ± 500	13.44 ± 0.21	0.28 ± 0.01	4.09	12	O	0
vEHB-4	1.97628738	23000 ± 500	22.15 ± 0.22	0.30 ± 0.01	9.57	10	O	0
vEHB-5	3.23990003	22000 ± 500	18.92 ± 0.11	0.30 ± 0.01	5.10	8	O	—
vEHB-6	50.10395158	19000 ± 500	12.54 ± 0.21	0.32 ± 0.02	4.20	12	O	98.9
vEHB-7*	3.02583807	24000 ± 500	49.30 ± 0.08	0.41 ± 0.02	3.75	5	I	96.6
vEHB-8	2.89086189	21000 ± 500	28.77 ± 0.17	0.41 ± 0.02	3.06	9	I	98
vEHB-9	6.90595098	18000 ± 500	14.96 ± 0.25	0.40 ± 0.02	2.57	8	O	0
vEHB-10*	3.58179363	26000 ± 500	53.26 ± 0.51	0.36 ± 0.01	2.39	11	O	92.6
vEHB-11	3.19599005	17000 ± 500	16.35 ± 0.16	0.47 ± 0.03	1.75	7	I	59.4
vEHB-12	4.26386105	21000 ± 500	25.24 ± 0.48	0.38 ± 0.02	8.99	15	O	99.3
Candidate vEHBs								
vEHB-13	0.80305948	21000 ± 500	27.57 ± 0.17	0.40 ± 0.02	8.53	9	I	97.9
vEHB-14	11.37292900	24000 ± 500	18.75 ± 0.22	0.25 ± 0.01	4.00	11	O	0
vEHB-15	2.32221267	25000 ± 500	21.94 ± 0.16	0.25 ± 0.01	3.00	8	O	96.1

$^{(a)}$ From Momany et al. (2020). $^{(*)}$ These stars are classified as pHB stars by Prabhu et al. (2021a). vEHB-10 is categorized as a pHB star also by Schiavon et al. (2012).

The derived fundamental parameters, L and T_{eff}, are plotted against the periods of the vEHB stars in Figure 4.5. From the right panel, hardly any correlation can be observed between the T_{eff} and period. The left panel shows the same tentative trend that was observed earlier, that the vEHBs with the longest periods have the smallest bolometric luminosities. The two stars which slightly deviate from the trend are also the same. Therefore, it can be concluded there is a tentative correlation between the luminosity and period among the EHB stars.

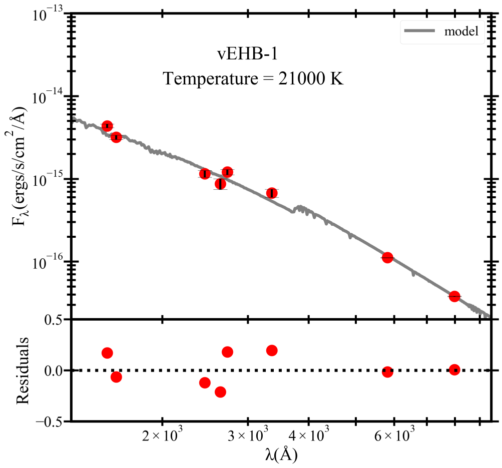

Figure 4.4: The SEDs for two of the vEHBs, namely vEHB-1 and vEHB-6, after extinction correction. The gray line shows the model spectrum. The residuals of the SED fit are shown in the bottom panels of both plots.

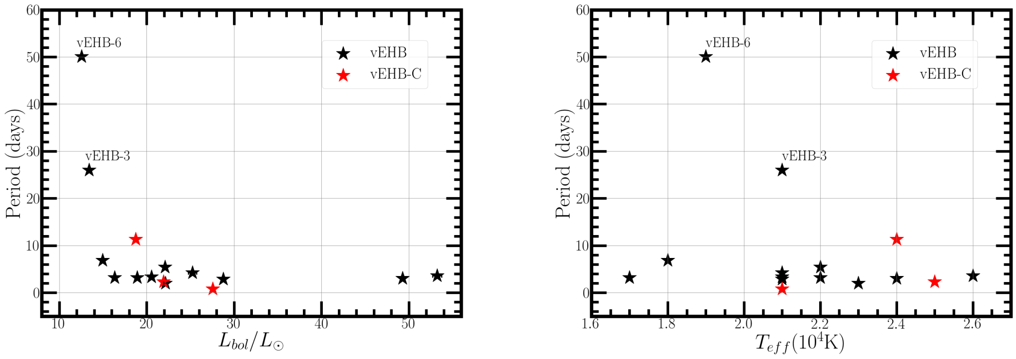

Figure 4.5: The $L/L_\odot$ and T_{eff} derived from SED fitting technique, plotted against the periods of all the vEHB stars. The longest period variables are marked in the plots.

4.4 Discussion

The UV follow-up study of the newly discovered spotted EHB stars in the GC NGC 2808 is presented here. The UVIT data is used in combination with the data from the HUGS catalog and the ground-based optical photometric catalog. From the $m_{F154W} - m_{F606W}$ vs. m_{F154W} CMD, it can be found that about half of the vEHB stars belong to the EHB population, which is sub-luminous with reference to the theoretical ZAHB model. The faintest among these stars (vEHB-6 and vEHB-3) are those with the longest periods. However, the location of these stars in the CMD may not be an effect of their rotation as two other stars are detected with shorter periods that have similar F154W magnitudes within errors.

The SED analysis of vEHB stars leads to an inference that the slowest rotators also have the smallest bolometric luminosities. It can also be seen that two of the vEHBs have very high luminosities (vEHB-7 and vEHB-10). These stars have been classified as AGB-manqué stars in the works of Schiavon et al. (2012) and Prabhu et al. (2021a). Also, since the amplitude of variability of all the vEHB stars is very small ($\Delta U_{Johnson} \sim 0.04 - 0.22$ mag), it is highly improbable that the results obtained in this study are significantly affected due to the variability.

Recio-Blanco et al. (2002) obtained the rotational velocities of hot HB stars in this GC. Their analysis showed that about 20% of the HB stars hotter than T_{eff} $\sim$ 11,500 K are slow rotators with v sin i less than 2 km s^{-1}, which corresponds to the rotational velocity of the Sun. The catalog of these slow-rotating hot HB stars will be availed from the authors in the future. It will be useful to check if any of these slow-rotators are also vEHBs and to confirm if rotation influences the UV magnitudes of these stars.

The population of vEHBs found to be sub-luminous in the FUV bands in this study could be indicative of the α^2 CVn mechanism at play as sizeable surface magnetic spots can result in fainter FUV magnitudes of the sources. However, a detailed analysis of the NUV and FUV light curves of these spotted stars is required for firmer conclusions. We plan to carry out such variability studies using UVIT in the future.

4.5 Summary

To sum up, the results of this chapter are as follows:

1. The *AstroSat*/UVIT photometric analysis of the vEHB stars in the GC NGC 2808 is presented here. The UVIT data are used in combination with the data from HUGS and ground-based optical photometry catalogs. The UV study of these objects is crucial because the α^2 CVn mechanism, which is suggested to be responsible for the detected variability in EHB stars, results in fainter UV magnitude depending on spot properties and higher variability in the UV wavebands than in the optical.

2. The FUV-optical CMD of the UV-bright cluster members, along with all the reported vEHB stars, is shown. The location of the HB sequence is compared with the theoretical ZAHB and TAHB models. It is found that about half of the vEHB stars belong to the EHB population that is sub-luminous in comparison with the theoretical ZAHB, as expected from the suggested α^2 CVn mechanism.

3. A plot of the UV magnitudes versus the periods of the vEHB stars shows that the two longest period variables (vEHB-6 and vEHB-3) are the faintest in the two FUV wavebands and within errors in the four NUV wavebands.

4. SED fitting technique was adopted to estimate parameters such as T_{eff}, $R/R_{\odot}$, and $L/L_{\odot}$ of these stars. The plot of $L/L_{\odot}$ against the periods shows that the two longest period vEHBs also have the smallest bolometric luminosities among the sample.

5. A detailed study of the UV variability of these spotted stars using UVIT data will be carried out in the near future.

Chapter 5

The First Extensive Far-UV Investigation of Omega Centauri[†]

5.1 Introduction

Omega Centauri (ω Centauri; or NGC 5139) is the most massive GC in the Galaxy (mass $= 3.5 \times 10^6 M_\odot$; Baumgardt & Hilker 2018). It is located at a distance of 5.426 kpc (average distance from Baumgardt & Vasiliev (2021)).

ω Centauri has the most complex MSP scenario among GGCs. Along with light-element abundance variations and anti-correlations among stars, a wide range in metallicity ($-2.2 \lesssim$ [Fe/H] $\lesssim -$ 0.6 dex) has also been reported in this GC through spectroscopic measurements (Norris & Da Costa 1995; Suntzeff & Kraft 1996; Johnson & Pilachowski 2010; Latour et al. 2021, and references therein). Using HST photometry, Bedin et al. (2004) reported that the MS split into two main components, red MS (rMS) and blue MS (bMS). Through spectroscopic

---

[†] Results of this work are published in Prabhu et al. (2022).

measurements of stars along each sequence, Piotto et al. (2005) suggested that the bMS is more metal-rich (by ≈ 0.3 dex) compared to rMS, which was contrary to the expected relation of color with metallicity. To explain this, it was proposed that the bMS is also enhanced in He (with ΔY up to 0.15) compared to the rMS. Using the spectra of about 3000 MS stars from the Multi Unit Spectroscopic Explorer (MUSE) instrument at the Very Large Telescope (VLT), Latour et al. (2021) showed that the bMS is metal-rich by 0.1 dex and He-enhanced (ΔY = 0.08) compared to rMS stars. He-enhanced populations in ω Centauri have also been proposed from isochrone-fitting and population synthesis methods (Norris 2004; Lee et al. 2005; Joo & Lee 2013; Tailo et al. 2016, and references therein).

Pancino et al. (2000) and Calamida et al. (2017) studied the spatial distributions of the MSPs along the RGB and found that the higher metallicity red giants were centrally more concentrated and spatially extended than their metal-poor counterparts. The differences among the spatial distributions of MS subpopulations were studied by Bellini et al. (2009) and Calamida et al. (2020). The authors observed that the stars belonging to the bMS, which are supposedly metal-rich and He-enhanced, are centrally more concentrated than the rMS stars.

ω Centauri hosts the largest known population of very hot HB stars (D'Cruz et al. 2000). He-enhancement has been proposed as an explanation for the blue and extended HB morphology (Joo & Lee 2013; Tailo et al. 2016). Moehler et al. (2011) and Latour et al. (2014) suggested that the hottest HB stars are likely to have experienced a delayed He-flash. In this instance, the stars lose substantial mass during the RGB phase, which causes them to either have a late He-flash and become EHBs or completely evade the He-flash and become He-core WDs (Castellani et al. 2006). The findings of Calamida et al. (2008), who detected 6,500 WDs in ω Centauri using HST optical data, provided validation of this scenario. The authors compared the WD and MS star counts and found evidence for the existence of He-core WDs, confirming the theory that certain RGB stars bypass the He-flash and develop directly into WDs. Using HST NUV-optical data, Bellini et al. (2013) discovered a bifurcation along the WD sequence into two main components, the red and the blue WD sequences. The blue sequence was proposed to form from the end-products of the "He-normal" subpopulation (0.55 $M_{\odot}$ CO-core WDs), and the red sequence from those of the "He-enhanced" subpopulation (0.46 $M_{\odot}$ CO-core and He-core WDs).

Thus, it is puzzling how ω Centauri's numerous populations came to be. The two most popular theories among the many that have been put forth are (i) that ω Centauri is the core of a dwarf galaxy that underwent multiple star formation events before being accreted by the Milky Way (Ibata et al. 2019) or (ii) that ω Centauri resulted from two or more clusters merging together (Calamida et al. 2020, and references therein).

The previous FUV study of this cluster was conducted decades back using the UIT (Landsman et al. 1992; Whitney et al. 1994, 1998) and the HST (D'Cruz et al. 2000). However, these datasets are incomplete due to the limited spatial resolution of UIT ($\sim 3''$) and FOV of HST/WFPC2.

This chapter presents the first comprehensive FUV investigation of ω Centauri extending from its center to $\sim$ 28% of the tidal radius, $r_t = 48'$ (Harris 1996, 2010 edition, hereafter H96), carried out using *AstroSat*/UVIT. For the first time, populations of HBs and WDs are detected which are anomalously fainter in the FUV band as compared to theoretical models as well as their counterparts in another massive GC, M13.

5.2 Observations And Data Reduction

ω Centauri was observed as a part of the Globular Cluster UVIT Legacy Survey (GlobULeS, Sahu et al. 2022) on 24 January 2021 in two FUV filters, F148W, and F169M, covering the entire 28′ diameter FOV of the instrument. The CCDLAB software package (Postma & Leahy 2017) was used to create the science-ready images, as described in Chapter 2, with exposure times of 6310.95 s (F148W) and 6268.10 s (F169M). The astrometric calibration was performed using GALEX NUV image (Bianchi et al. 2017) and the *Gaia EDR3* data (Gaia Collaboration et al. 2021) as references, and the final accuracy was $\sim 0\farcs5$.

PSF photometry on these images is performed as detailed in Chapter 2. The source catalog was refined by removing three visibly saturated stars and those lying at the edge of the UVIT FOV. The final catalog contains only the stars with PSF-fit errors less than 0.25 mag and those detected in both the filters (N = 3697; obtained by matching the coordinates within a maximum match radius of 1″). The UVIT image of the cluster in the F148W filter and the magnitude vs. photometric error plots are shown in Fig. 5.1.

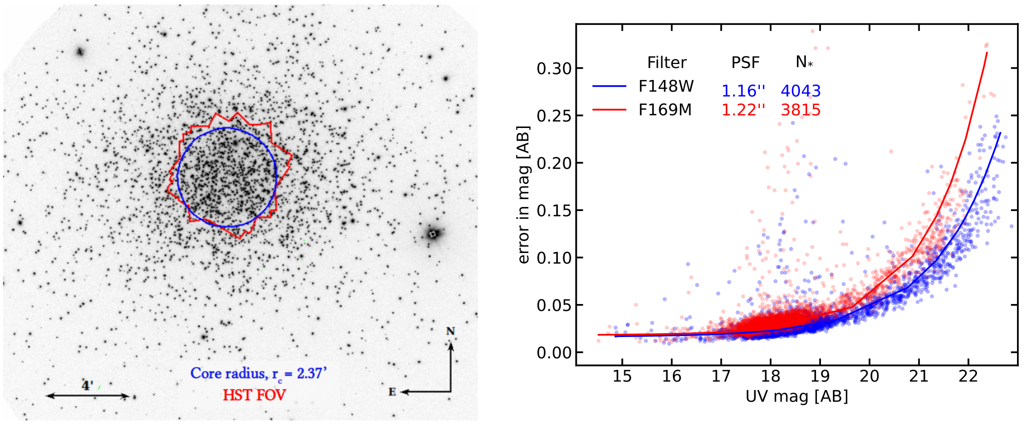

FIGURE 5.1: Left: UVIT/F148W image of ω Centauri. Right: Plot of PSF-fit errors vs. magnitudes (not corrected for extinction) in the two filters. The filter names, FWHM of the PSF, and number of detections with fit error < 0.25 mag (N*) are indicated. The line indicates the median error in each filter.

The magnitudes were corrected for extinction by adopting $E(B-V)_{avg} = 0.12$ mag (H96), $R_V = 3.1$, and the Fitzpatrick reddening law (Fitzpatrick 1999). The extinction coefficient values are 0.98 mag and 0.93 mag, respectively, for the F148W and F169M filters[*].

5.3 Cross-Match Of UVIT Detections With Different Catalogs

5.3.1 UVIT-*HST* Cross-Match

The optical counterparts of the FUV detections were identified by cross-matching those within the core radius of the cluster ($r_c = 2\farcm37$) with the HST dataset from Bellini et al. (2017a). This astrophotometric dataset was available in 18 WFC3/UVIS bands and 8 WFC3/IR bands for 478,477 stars. However, only the WFC3/UVIS data were used since the IR photometry did not include the information on the saturated stars, many of which belonged to the HB. The saturated stars also did not have proper motion (PM) measurements in the catalog. Hence, a filtering of the sources based on cluster membership was not performed. A direct cross-match of the UVIT and HST catalogs would result in many spurious identifications because of the differences in spatial resolution and astrometric accuracy. Hence, a subset of stars from the HST dataset was chosen, which included only the UV-bright stellar populations such as HB, pHB, BSSs, and WDs. The HST photometry in Bellini et al. (2017a) was measured with three methods, each of which worked best in different magnitude regimes. Following the same selection criteria as the authors, the results of method 1 photometry for HB, pHB, and BSS stars and those of method 2 for WDs were used. The UV color-magnitude plane

---

[*] Calculated using the York Extinction Solver (McCall 2004)

$m_{F275W} - m_{F336W}$ vs. m_{F275W} was used to select the HB, pHB, and BSS stars, and the WDs were selected from the $m_{F438W} - m_{F606W}$ vs. m_{F438W} plane. This HST subset was cross-matched with the UVIT catalog with a maximum match radius of $0\farcs7$, using TOPCAT, and about 963 stars were found to have unique counterparts. The accuracy of the cross-identifications was also manually verified. A counterpart could not be identified correctly for one star at R.A. = 201.64700° and Decl. = −47.50401° in the UVIT catalog (it is not included in the HST catalog, although it is visible in the F555W image). So, this star is excluded.

5.3.2 UVIT-Ground Data-Gaia EDR3 Cross-Match

There were several UV-bright stars lying outside the HST FOV. In order to analyze these stars and plot them in the UV-optical CMD, the ground-based optical dataset in the $UBVRI$ filters from Stetson et al. (2019) and the *Gaia EDR3*-based catalog from Vasiliev & Baumgardt (2021) were used. For the cross-match, at first, a subset of stars from the ground-based catalog was created by selecting only the population expected to be bright in UV. This subset was matched with the UVIT detections with a maximum cross-match radius of $0\farcs7$. The number of stars common in both was about 2725. In order to identify the cluster members among them, this set was matched further with the *Gaia EDR3*-based catalog of Vasiliev & Baumgardt (2021). About 1771 stars were found to have a membership probability of more than 0.5. However, there were about 803 UV-bright stars that were not included in the *Gaia EDR3* catalog. Hence, their membership status is unknown. Finally, to plot all the sources in the similar color-magnitude plane, the Johnson-Cousins B, V, and I magnitudes of the stars in the outer region were transformed to the corresponding HST WFC3/UVIS filters (namely, $F438W$, $F606W$, and $F814W$), using the equations from Harris (2018).

5.4 Color-Magnitude Diagrams

The UV-optical CMD of the cluster was constructed by identifying the optical counterparts of the 3689 (out of a total of 3697) FUV-detected sources using the HST-based catalog of Bellini et al. (2017a) (for $r <$ core radius $r_c = 2\rlap{.}'37$, hereafter inner region) and the catalogs of Stetson et al. (2019) and Vasiliev & Baumgardt (2021) (for $2\rlap{.}'37 < r < 13\rlap{.}'5$; outer region) as described in Section 5.3. The optical magnitudes were converted from Vega to AB system using appropriate conversion factors.

Fig. 5.2 shows the optical and FUV-optical CMDs of the cluster along with various models and isochrone. For the HB, the BaSTI (Pietrinferni et al. 2021) theoretical ZAHB and TAHB models were used, which had $[\alpha/\mathrm{Fe}]$ =+0.4 dex, and mass-loss parameter $\eta = 0.3$, where, overshooting is not applied, and atomic diffusion effects are included. Three models with the following metallicity and He abundance values were chosen: [Fe/H] $= -2.2$ dex, Y $= 0.247$ (metal-poor, He-normal); [Fe/H] $= -0.6$ dex, Y $= 0.257$ (metal-intermediate, He-normal) and [Fe/H] $= 0.06$ dex, Y $=$ 0.320 (metal-rich, He-enhanced). These choices were based on the values reported in the literature and as per the availability in the database. For the BSS sequence, the BaSTI ZAMS isochrone of age = 0.5 Gyr, with initial mass range $\sim$ 0.5 - 1.5 $M_\odot$ corresponding $[\mathrm{Fe/H}]_{avg} = -1.55$ dex and primordial Y value was used. For the WD population, two DA spectral type models with pure H grid and thick H layers with masses 0.5 $M_\odot$ and 0.6 $M_\odot$ were adopted (private comm. with Pierre Bergeron).

The locations of the HBs, BSSs, and WDs in the optical CMDs match well with the model predictions (left panels of Fig. 5.2). In the FUV-optical CMDs (right panels), the RHB and BSS sequences lie at the locations expected from the models. It is well known that the hottest HBs, known as BHk stars, appear fainter than canonical ZAHB models in CMDs (Whitney et al. 1998; D'Cruz et al. 2000).

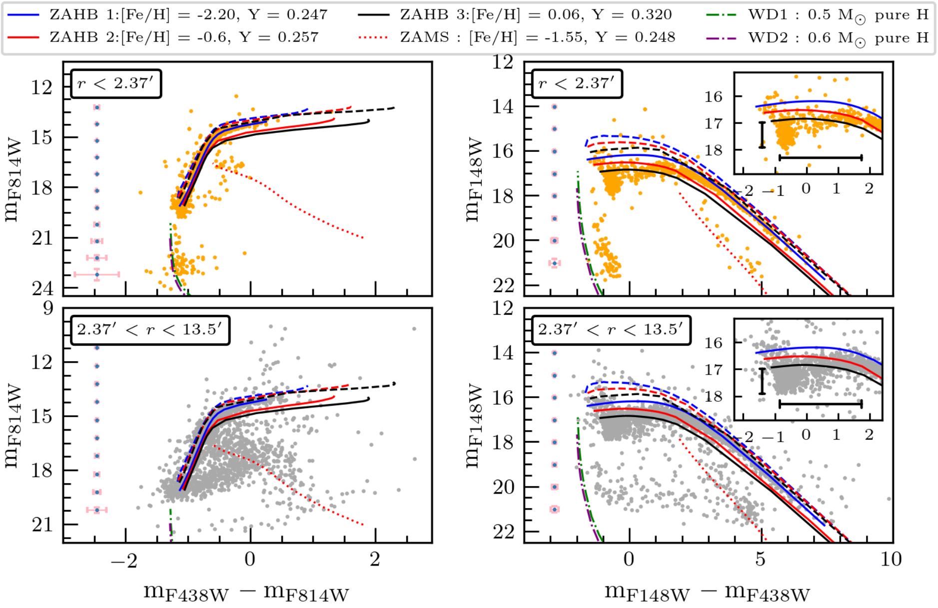

FIGURE 5.2: Theoretical stellar evolutionary models overplotted on the optical and FUV-optical CMDs. The BaSTI ZAHB and TAHB models for different metallicities and He abundances are shown with continuous and dashed lines, respectively. The dotted lines represent the BaSTI ZAMS isochrone. The dash-dotted lines represent WD cooling sequences. The parameters corresponding to all the models are indicated on the top panel of the figure.

However, all hot HBs (hHBs) with $m_{F148W} - m_{F438W} \lesssim 2.0$ mag are found to be fainter in the F148W band by about ~ 0.5 mag whereas no anomaly is observed in optical CMDs. The WDs, too, are redder by a comparable magnitude only in the FUV-optical CMDs (implying fainter FUV magnitudes). A similar behavior is observed in the UVIT F169M filter (not shown here). We checked for possible effects on the estimated magnitude due to the instrument calibration or analysis procedure as described in the following section.

5.4.1 Possible Causes For The Difference Between Observation And Models In The FUV-Optical CMDs

Checks were performed for various aspects that could possibly result in the bias observed in the FUV-optical CMDs. Firstly, effects due to UVIT instrument-related aspects, such as changes in calibration, sensitivity, and the slope of the transmission window, were inspected. These were ruled out as magnitudes obtained from the recent observations of FUV-bright sources in the secondary calibration source, open cluster NGC 188, and a previously studied GC NGC 2808, were consistent with earlier estimates. Next, the effects due to data reduction and analysis procedures were examined. Similar magnitudes (within ~ 0.1 mag) were obtained with science-ready images produced using CCDLAB and the official UVIT L2 pipeline, ruling out any issue due to the data-reduction pipeline. Photometric analysis with IRAF was checked independently and found to be consistent. Lastly, any possible changes introduced due to the transformation of optical magnitudes from the Vega to AB system were looked for. The bias was found even when the filter with the smallest transformation factor (F606W) was used, ruling out this possibility.

In the top panels of Figure 5.3, the CMDs constructed using the UVIT F148W and the HST F275W (NUV) and F336W (UV wide) filters are shown, consisting of the 963 UVIT-HST common detections. It can be observed that the hHBs and WDs show a deviation from model predictions in these CMDs also. Additionally, the CMD constructed using only the HST filters F275W and F336W, with the data from Bellini et al. (2017a), also shows the deviation, supporting this work (bottom left panel of Fig. 5.3). In the bottom right panel of Fig 5.3, the CMD with sources detected in both the UVIT FUV filters is shown. Based on the above, we conclude that the deviation between the observation and the models is likely to be real and unlikely due to instrumental or procedural issues.

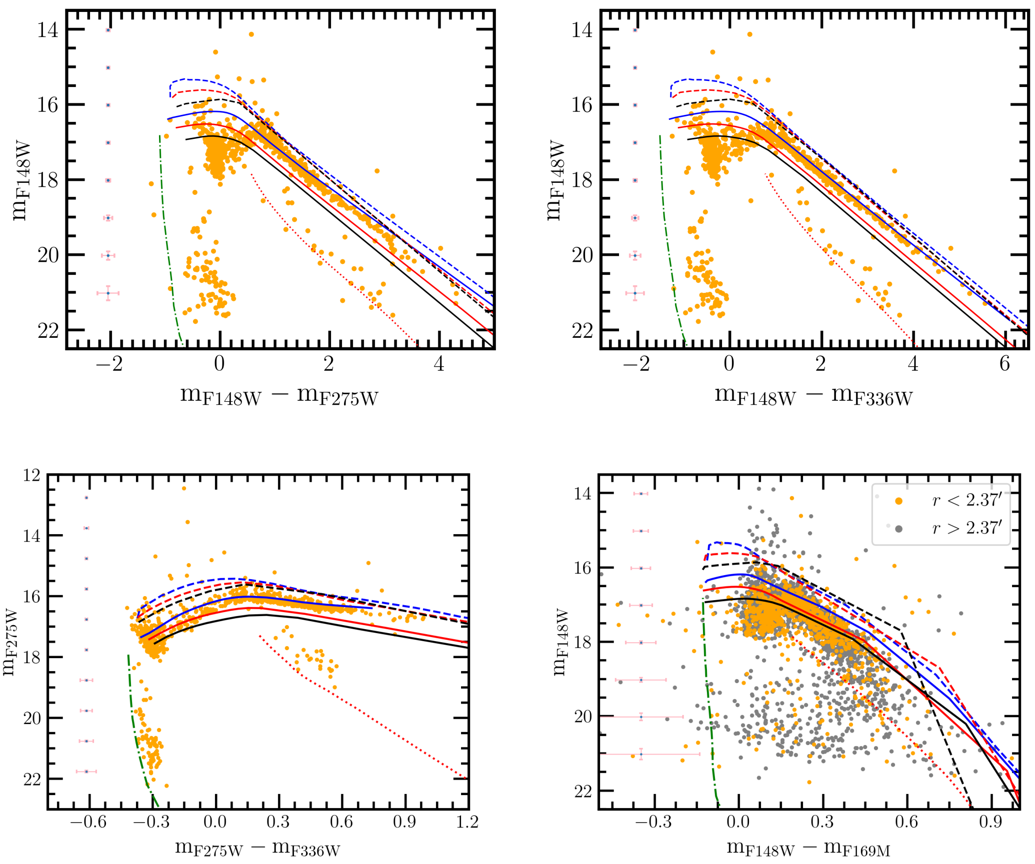

FIGURE 5.3: Top panels: The UVIT/F148W−HST/F275W vs HST/F275W and UVIT/F148W−HST/F336W vs HST/F336W CMDs showing the UVIT-HST common detections (963 stars), along with the theoretical stellar evolutionary models shown in Fig. 5.2. Bottom left: The F275W−F336W vs. F275W CMD with the same 963 stars as above is shown. Bottom right: The CMD that consists of all the sources detected in both the UVIT F148W and F169M filters, along with evolutionary models.

5.5 HB Simulations

To check if the observed HB distribution originated from the extreme enhancement in He, synthetic CMDs shown in Figure 5.4 were produced. Generally, the synthetic/simulated CMD should simultaneously reproduce both the HB morphology and the MS to RGB stars. Reliable stellar parameters and subpopulations' ratios can be derived based on this. However, due to the observational limitations on MS to RGB stars in the FUV regime, the CMD synthesis was carried out only for HBs by referring to the stellar parameters of Joo & Lee (2013) for ω Centauri who reproduced both sequences simultaneously. Three stellar parameters $\mathrm{Y_{ini}}$, age, and [Fe/H] were adjusted to find the best match to the observations. The value of Reimers' mass-loss efficiency parameter (Reimers 1977), η was adopted as 0.5 as per the calibration by Chung et al. (2017). This parameter appears in the Reimers' empirical formula for the mass-loss along the RGB (Reimers 1977), given by the relation, $dM/dt \propto \eta(L/gR)$, where L, g, and R are the luminosity, gravity, and radius of the star, respectively. The detailed descriptions for other parameters and the simulation are summarized in Chung et al. (2017). Note that the evolved phase of HBs (i.e., AGB manqué phase) was not included in the model to avoid the highly uncertain stellar evolution tracks after the He-core depletion.

Five subpopulations were assumed to reproduce HB morphologies in two observed CMDs. From G1 to G5, the stellar parameters for each subpopulation are indicated above Figure 5.4. The He-normal G1 ($\mathrm{Y_{ini}} = 0.23$) and slightly He-rich G2 ($\mathrm{Y_{ini}} = 0.28$) show reasonable agreements with the observed blue HBs. In the simulation, the extremely hot HBs mainly originated from G3 and G4 populations with $\mathrm{Y_{ini}} = 0.43$ and 0.38, respectively. If $\mathrm{Y_{ini}}$ is not changed, other values of age or metallicity (i.e., extremely old or metal-poor populations) cannot reproduce those HBs. In addition, as Figure 6 of Joo & Lee (2013) shows, ω Centauri hosts at least one extreme metal-rich MS to RGB sequence. To explain this population, the G5 population with $[\mathrm{Fe/H}] = -0.4$ dex and $\mathrm{Y_{ini}} = 0.38$ was added, and this subpopulation matches HBs around $(F148W - F438W) \simeq 0.0$ as well. The fractions of the simulated subpopulations from G1 to G5, adopted based on Joo & Lee (2013), are 0.49, 0.27, 0.10, 0.07, and 0.07, respectively.

The FUV-optical CMD and the radial distribution of the HB stars belonging to different subpopulations are shown in Figure 5.5. Here, the older, He-normal subpopulations G1 and G2 were grouped together (purple symbols in the bottom left panel), and the younger, He-rich G3, G4, and G5 were combined as another sample (olive symbols). The He-rich, second-generation HB stars clearly appear more segregated. The Kolmogorov-Smirnov test returned a *p*-value of $\sim 1 \times 10^{-5}$, indicating that the two subpopulations are not drawn from the same distribution.

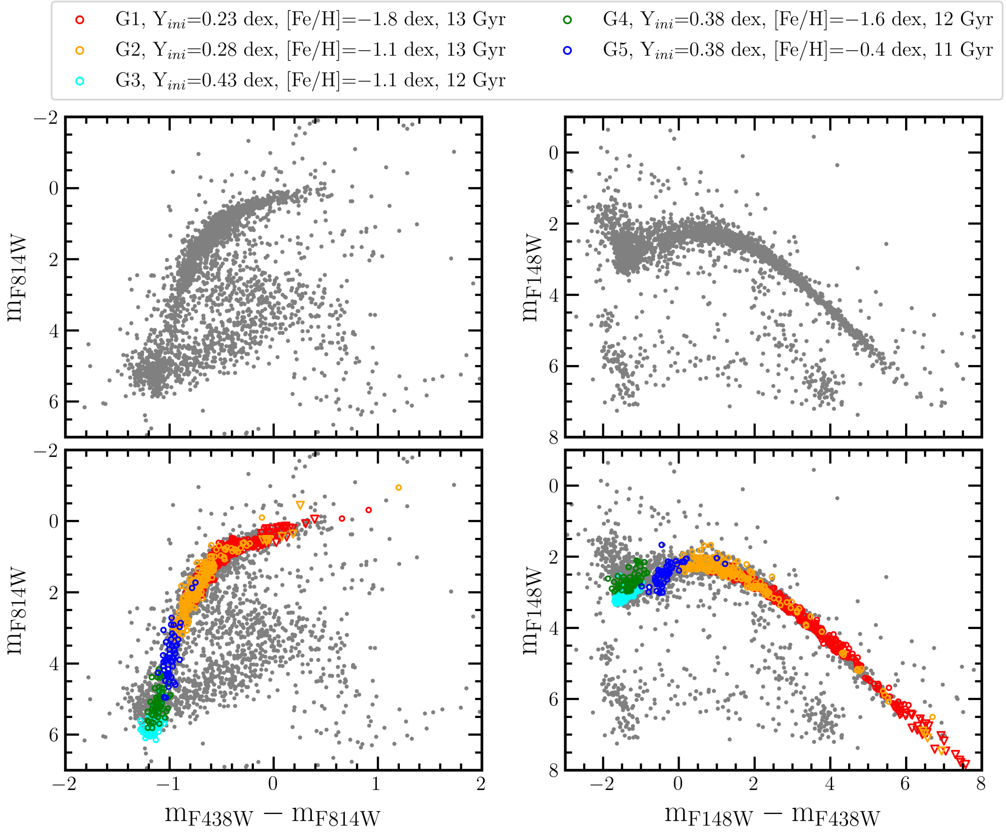

FIGURE 5.4: HB simulations of the subpopulations: The top panels show the observed optical and FUV-optical CMDs, and the bottom panels show the simulated HB CMDs overplotted on the observed. Parameters suggested from our best-fit simulation for subpopulations from G1 to G5 are indicated in the legend above. The triangles in the bottom panels denote the simulated RR Lyrae stars. The distance modulus and reddening adopted to reproduce the observed CMDs are $(m-M)_{F148W} = 15.5$ mag, $E(F148W - F438W) = 1.2$ mag, and $(m-M)_{F814W} = 14.1$ mag, $E(F438W - F814W) = 0.3$ mag, respectively.

5.6 Characterization Of Hot Populations

The SED-fitting technique was adopted to characterize the hot stars that showed a departure from the BaSTI tracks. The SEDs were constructed and fitted with

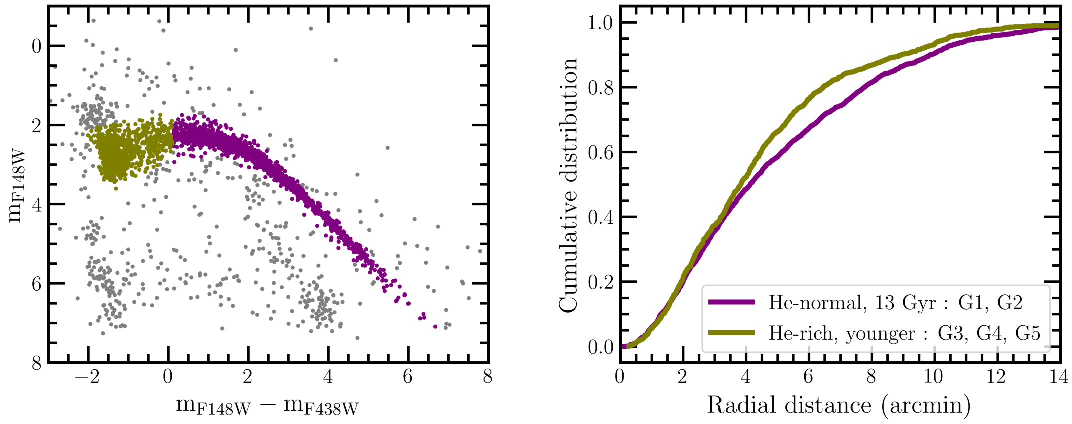

FIGURE 5.5: The radial distributions of the HB subpopulations are shown. Here, G1 and G2 subpopulations are considered as a single group and G3, G4, and G5 as another, indicated with purple and olive symbols, respectively, in the left panel.

appropriate models using VOSA as described in Chapter 2.

5.6.1 Hot HB Stars

The SEDs of hHBs were fitted using six appropriate models whose parameters and available ranges are tabulated in Table 5.1. Three approaches were adopted, aiming to test different aspects. In the first approach, the SEDs were fitted adopting the values listed in the last column of Table 5.1 and by fixing the value of A_V to 0.372 mag for $E(B-V)_{avg} = 0.12$ mag. In the next approach, to check for the effects due to radiative levitation observed in HBs hotter than the Grundahl-jump ($T_{\rm eff} \sim 11\,500$ K; Grundahl et al. 1999), the metallicity parameter was allowed to vary up to the solar value keeping A_V and the other parameter ranges unchanged. The final approach was meant to check for the effect of differential reddening reported in the cluster (Calamida et al. 2005; Bellini et al. 2017b) wherein A_V was included as a fit parameter with a range 0.279 - 0.775 mag corresponding to $E(B-V) = 0.09$ - 0.25 mag, keeping all other parameter ranges as in the last column of Table 5.1.

TABLE 5.1: Models and parameter ranges adopted to fit the SEDs of hot HB stars and WDs

Model	Parameter	Available range	Adopted range
		Hot HB stars	
Kurucz ODFNEW/NOVER[a]	$T_{\rm eff}$	3 500 to 50 000 K	10 000 to 50 000 K
	$\log g$	0 to 5 dex	3 to 5 dex
	[Fe/H]	−4.0 to 0.5 dex	−2.5 to −0.5 dex
TMAP Grid 2[b]	$T_{\rm eff}$	20 000 to 150 000 K	20 000 to 100 000 K
	$\log g$	4 to 9 dex	4 to 5.5 dex
TMAP Grid 4[b]	$T_{\rm eff}$	20 000 to 150 000 K	20 000 to 100 000 K
	$\log g$	4 to 9 dex	4 to 5.5 dex
	H mass fraction	0 to 1	0 to 1
TMAP Tübingen[b]	$T_{\rm eff}$	30 000 to 1 000 000 K	30 000 to 100 000 K
	$\log g$	3.8 to 9 dex	3.8 to 5.5 dex
	H mass fraction	0 to 1	full range
	He mass fraction	0 to 1	full range
Pacheco et al. (2021)	$T_{\rm eff}$	10 000 to 65 000 K	full range
	$\log g$	4.5 to 6.5 dex	4.5 to 5.5 dex
	[Fe/H]	−1.5 to 0.0 dex	−1.5 dex
	$\log\,(\mathrm{n}_{He}/\mathrm{n}_H)$	−4.98 to 3.62	full range
Husfeld et al. (1989)	$T_{\rm eff}$	35 000 to 80 000 K	full range
	$\log g$	4.0 to 7.0 dex	4.0 to 5.5 dex
	Y_{He}	0.0 to 0.7	full range
		WDs	
Koester[c]	$T_{\rm eff}$	5 000 to 80 000 K	full range
	$\log g$	6.5 to 9.5 dex	full range
Levenhagen[d]	$T_{\rm eff}$	17 000 to 100 000 K	full range
	$\log g$	7.0 to 9.5 dex	full range

[a] [α/Fe] = 0.4 dex; Castelli & Kurucz (2003)

[b] Werner & Dreizler (1999); Werner et al. (2003); Rauch & Deetjen (2003)

[c] Koester (2010)

[d] Levenhagen et al. (2017)

The top left panel of Fig. 5.7 shows the FUV-optical CMD highlighting the sample of hHBs analyzed. Among the inner region stars, all the 421 HBs bluer than the knee point in the CMD (at color $\sim$ 2.0 mag) were chosen, which are shown with red circles and denoted as OC hHB-I. For these stars, the UVIT photometry in two filters was combined with the photometric data in 18 HST WFC3/UVIS filters from Bellini et al. (2017a). Among the outer sources, the 150 EHB stars with confirmed cluster membership obtained through a cross-match with the sample of Latour et al. (2018) (shown with blue circles and denoted as OC EHB-O) were selected. The SEDs of these stars were constructed by complementing the UVIT photometry with the data in five optical filters from the catalog of Stetson et al. (2019). Thus, the physical parameters for a total of 571 hHBs were derived using the three approaches mentioned above. Fig 5.6 shows the histograms of the parameters derived using the three approaches. Since the results were found not to differ much, the discussions below are based on the first approach.

Good fits, with $Vgf_b < 15$ (Rebassa-Mansergas et al. 2021), were achieved for about 97% of the hHBs. The middle left panel of Fig 5.7 shows the H-R diagram for these stars along with the same ZAHB models as in Fig. 5.2, EHF & LHF models (Cassisi et al. 2003) and a 0.44 $M_{\odot}$ He-core DA-type WD model with Y_{ini} = 0.4, Z = 0.0005 progenitor (Althaus et al. 2017). Most of the stars cooler than log $T_{\rm eff}$ $\sim$ 4.2 lie within the range of the ZAHB models. A significant fraction within log $T_{\rm eff}$ $\sim$ 4.2 to 4.5 are fainter than any of the ZAHB models. Their luminosity decreases with $T_{\rm eff}$ reaching a minimum at log $T_{\rm eff}$ $\sim$ 4.4, which then increases further. The hHBs within the log $T_{\rm eff}$ $\sim$ 4.5 to 4.65 are lying on the EHF and LHF tracks. The ones hotter than log $T_{\rm eff}$ $\sim$ 4.6 follow the 0.44 $M_{\odot}$ WD model. In the bottom left panel, the log (R/R$_{\odot}$) of hHBs are plotted as a function of the log $T_{\rm eff}$, where the low-luminous hHBs of ω Centauri are also found to be smaller in size.

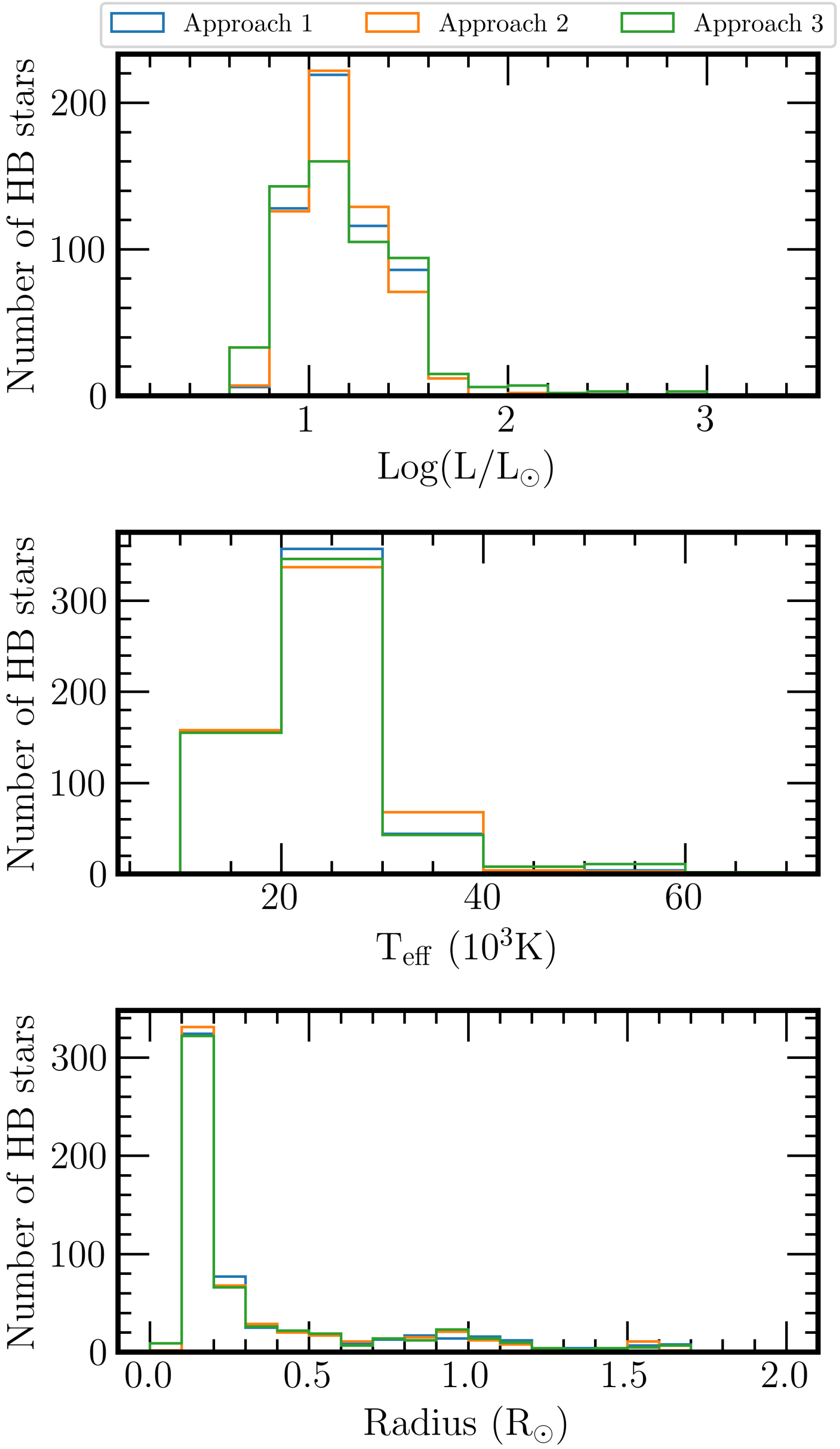

FIGURE 5.6: Plot showing the histograms of bolometric luminosity, effective temperature, and radius for EHB stars derived using three approaches described in the text.

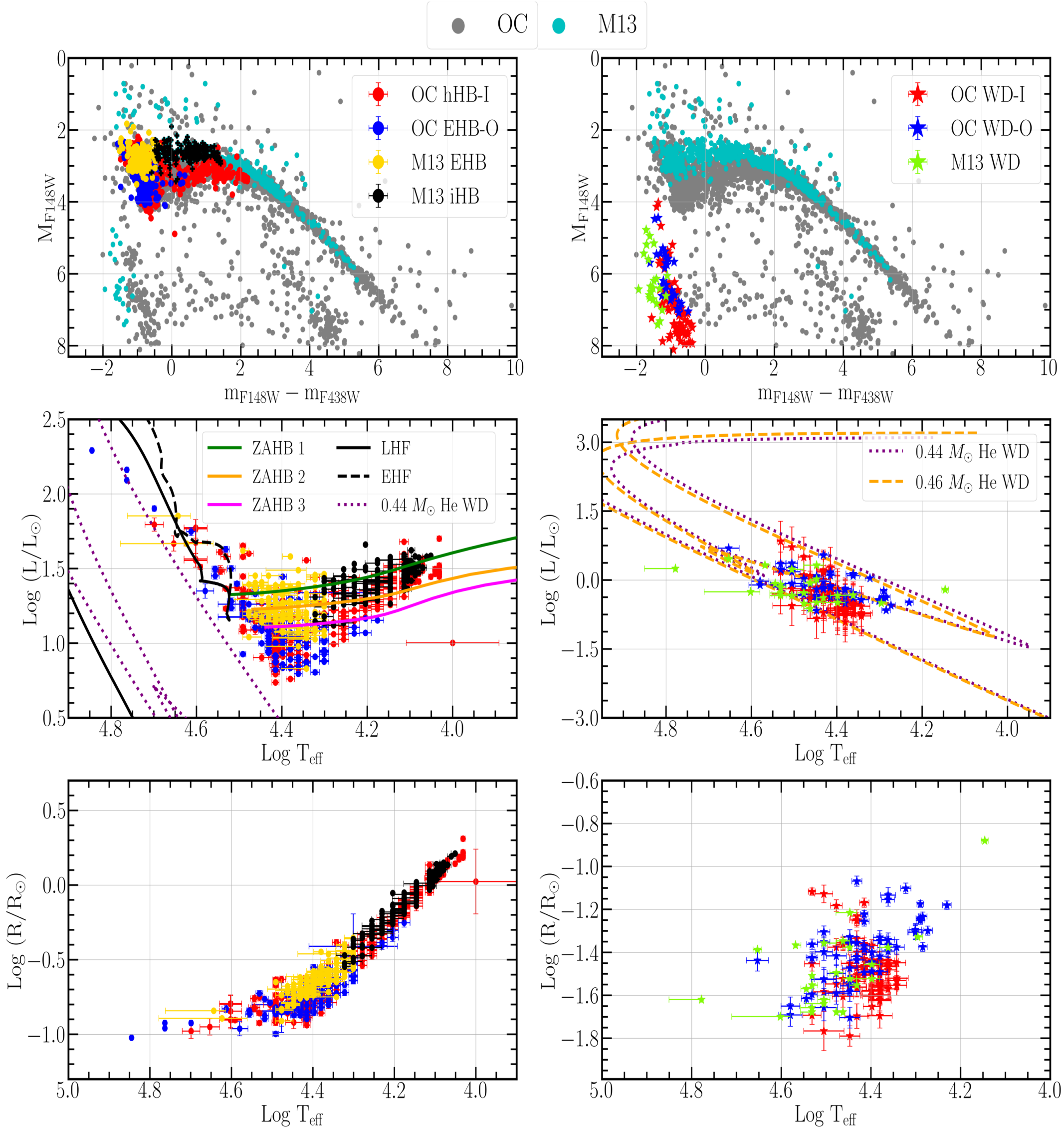

FIGURE 5.7: Comparison of the FUV-optical CMD, H-R diagram, log $T_{\rm eff}$ vs log $(R/R_\odot)$ plots for ω Centauri (OC) and M13 with focus on the hHB population and WDs. The -I (-O) denotes stars within the inner (outer) region. The parameters corresponding to ZAHB models in the middle left panel are as follows - ZAHB 1: [Fe/H] $= -2.20$ dex, Y $= 0.247$; ZAHB 2: [Fe/H] $= -0.6$ dex, Y $= 0.257$; and ZAHB 3 $=$ [Fe/H] $= 0.06$ dex, Y $= 0.32$. LHF is a late hot flasher model with [M/H]$=-1.018$ dex, Y $= 0.250$, M$_{ZAHB}$ $= 0.490\,M_\odot$ and EHF is an early hot flasher model with [M/H] $= -1.90$ dex, Y $= 0.247$ and M$_{ZAHB}$ $= 0.502\,M_\odot$.

5.6.2 WDs

The top right panel of Fig. 5.7 shows the FUV-optical CMD highlighting the WD sample chosen for SED-fitting. There are 77 (68) WD candidates from the inner (outer) region represented by red (blue) star symbols and denoted as OC WD-I (OC WD-O), whose SEDs were fitted using models and parameters tabulated in Table 5.1. While inspecting the SEDs, it was found that about 8 outer WDs showed UV-excess. Their SEDs could not be fitted with a single WD model and, hence, were not considered further. The fits with $Vgf_b > 15$ were also excluded. The SED parameters for the rest of the sample (135 stars) are shown in the H-R diagram on the middle right panel of Fig 5.7 along with two He-core models of masses 0.44 $M_\odot$ and 0.46 $M_\odot$ with He-rich ($Y_{ini} = 0.4$), $Z = 0.0005$ progenitors (Althaus et al. 2017). Most stars lie in between the range of the models. The bottom right panel shows the (log $R/R_\odot$) of the WDs as a function of the log T_{eff}, where the two populations of the WDs match well, except for a small number of cooler and larger WDs in the outer ω Centauri.

5.7 Comparison Of Hot Populations In Omega Centauri And M13

To further understand the peculiarities seen in the properties of hot stellar populations of ω Centauri, they were compared with those of another massive GC, M13 (or NGC 6205). M13 has [Fe/H] = −1.53 dex (H96) similar to the average [Fe/H] of ω Centauri with $\Delta Y_{max} \sim 0.05$ (Dalessandro et al. 2013; Milone et al. 2018) and age ≈ 13 Gyr (Denissenkov et al. 2017). M13 was also observed using UVIT as part of GlobULeS, and the detailed study has been carried out by Kumar et al. (2023). The final photometric data and the SED-fit results of HBs (in the range 11 500 K $\leq T_{\text{eff}} \leq$ 20 000 K; iHBs) and WDs were obtained from the authors. These are highlighted in yellow, black, and light green symbols among the rest of the M13 FUV sources (cyan) on the FUV-optical CMDs (top panels of Fig. 5.7). The ω Centauri populations with $m_{F148W} - m_{F438W} \lesssim 2$ are clearly fainter in the FUV when compared to those of M13, whereas the locations of redder stars match well.

The ω Centauri hHBs are, on average, less luminous than their counterparts in M13, and the latter also fall within the range of the ZAHB models as seen in the left middle panel. In the log T_{eff} vs. log $(R/R_{\odot})$ plot, a few of the ω Centauri hHBs (mostly near log $T_{\text{eff}} \sim 4.4$) are found to have smaller radii than their M13 counterparts. This could explain their lower luminosities. The above may also imply that a fraction of hHBs in ω Centauri are less massive than those of M13. The WDs in both clusters occupy similar positions in the H-R diagram and the log T_{eff} vs. log $(R/R_{\odot})$ plot on the middle and bottom right panels, respectively.

5.8 Discussion

In the FUV-optical CMDs, the HBs bluer than the knee point, and the WDs have fainter FUV magnitudes by about ~ 0.5 mag than canonical expectations. This is also observed in the absolute CMD plane when compared with the populations of another cluster having similar properties, namely, M13. Moni Bidin et al. (2012), by deriving color-temperature relations, found analogous results for ω Centauri hHBs wherein these objects were found to be fainter than canonical expectations in the U band while the B and V band observations matched well with the theoretical predictions. This anomaly, however, was not found in NGC 6752, the other cluster that the authors studied. The authors were unable to account for this peculiarity of ω Centauri.

A fraction of the FUV-faint hHBs could be EHB stars with magnetic spots that are dark in the FUV bands, discovered by Momany et al. (2020).

From HB simulations, it is found that at least five subpopulations with three He-rich ones are needed to explain the observed HB CMDs. As well known, it would be challenging to determine metallicity and age using HB CMDs only. However, in terms of HB morphology, it can be concluded that a considerable amount of He-enhancement is inevitable to explain the hHBs in FUV and optical CMDs. The fainter FUV magnitudes of hHBs could be thus due to the sensitivity of FUV bands to the Y_{ini} range (Chung et al. 2017). The derived parameters of the subpopulations are also comparable to the studies by Joo & Lee (2013). The He-rich younger subpopulations ($\sim 24\%$) are found to be radially more segregated than the He-normal older subpopulations ($\sim 76\%$), which is expected if the second-generation stars form from the ejecta of intermediate-mass AGB stars (D'Ercole et al. 2008). Similar results were reported by Bellini et al. (2009) for supposedly He-rich MS stars. The ranges in age, metallicity, and He content that are needed to fit the observed HB distribution provide constraints on the ω Centauri formation models.

The SED-fitting technique was employed to characterize the hot stellar populations that showed deviations in the CMDs. On the H-R diagram, most of the hHBs cooler than log $T_{\rm eff} \sim 4.2$ were found to lie within the range of the ZAHB models. A significant fraction within log $T_{\rm eff} \sim 4.2$ to 4.5 was found to be fainter than any of the ZAHB models used. These stars were also found to be less luminous than their counterparts in M13. In the log $T_{\rm eff}$ vs. log $(\mathrm{R}/\mathrm{R}_\odot)$ plot, some of the hHBs of ω Centauri were also found to have smaller radii compared to the M13 sample while spanning the same $T_{\rm eff}$ range. The above may also imply that a fraction of hHBs in ω Centauri are less massive than those of M13. Through spectroscopic measurements, Moni Bidin et al. (2011) and Latour et al. (2018) reported a mean mass lower than canonical expectations for EHB stars in ω Centauri ($0.38\,\mathrm{M}_\odot$)

and could not explain this conundrum.

On the H-R diagram, the ω Centauri WDs were found to lie in between the ranges of two He-core WD models[†] of masses 0.44 $M_{\odot}$ and 0.46 $M_{\odot}$ evolving from He-rich ($Y_{ini} = 0.4$ dex), $Z = 0.0005$ dex progenitors (Althaus et al. 2017). The M13 WDs were also found to occupy similar positions in the H-R diagram and the log $T_{\rm eff}$ vs. log radplot. However, unlike ω Centauri, M13 is not known to host extreme He-rich stars that can form He-core WDs from single stellar evolution. Chen et al. (2021) suggested that the bright WDs in M13 are the result of slow cooling due to the residual hydrogen burning on the CO WD surface. Hence, there is a possibility that some of the FUV-detected ω Centauri WDs are such slowly cooling CO WDs. Observations of WD pulsations in the future can shed more light in this direction (Althaus et al. 2017).

5.9 Summary

The key results from this chapter are summarized below :

1. This is the first extensive FUV study of ω Centauri extending from the cluster center to nearly 28% of its tidal radius. The investigation revealed that the HBs bluer than the knee point (hHBs) in the FUV-optical CMD, and the WDs were fainter in the FUV by about $\sim 0.5\,$mag than canonical models. However, the cooler populations, such as the red HB and BSSs, were found to match the model predictions in the FUV. The hHBs and WDs were also fainter in the FUV when compared to their counterparts in another cluster having similar properties, namely, M13. Some of the fainter hHBs could be spotted EHBs proposed by Momany et al. (2020).

[†] Note that the adopted He-core WD models do not result from binary evolution. See Althaus et al. (2017) for details.

2. To shed light on the peculiar HB populations and to estimate He-enhancements, metallicities, and ages of subpopulations, HB morphologies in the optical and FUV-optical planes were simulated. At least five subpopulations with three He-rich ones were required to explain the observed HB CMDs. The fainter FUV magnitudes of hHBs could also be due to the sensitivity of FUV bands to the Y_{ini} range (Chung et al. 2017) or due to the presence of surface chemical inhomogeneities (Momany et al. 2020). This work helps to provide constraints on the formation models of ω Centauri based on the estimated range in age, [Fe/H], and Y (in particular) for the HB stars.

3. The radial distributions of the subpopulations were examined, and the He-rich younger subpopulations ($\sim 24\%$) were found to be radially more segregated than the He-normal older subpopulations ($\sim 76\%$). A similar result was obtained in the case of He-rich MS stars in the work of Bellini et al. (2009). Such segregation of the younger subpopulations is anticipated if the second-generation stars originate from the ejecta of intermediate-mass asymptotic giant branch stars (D'Ercole et al. 2008).

4. The peculiar hot populations were characterized using the SED-fitting technique. The properties of hHBs in ω Centauri, when compared with those in M13, were found to be similar except for a fraction of low luminous ones with smaller radii in ω Centauri.

5. The WDs in ω Centauri and M13 were found to have similar physical parameters. They occupied the parameter space between two He-core WD models of masses 0.44 $M_{\odot}$ and 0.46 $M_{\odot}$ evolving from He-rich ($Y_{ini} = 0.4$ dex), $Z = 0.0005$ dex progenitors (Althaus et al. 2017). However, it is possible that some of the FUV-detected WDs in ω Centauri are slowly cooling CO WDs reported in M13 by Chen et al. (2021). This can be unveiled with photometric observations of WD pulsations in the future (Althaus et al. 2017).

6. This study presented a detailed characterization of the peculiar hot stellar population of ω Centauri using the excellent FUV imaging capabilities of *AstroSat*/UVIT.

Chapter 6

UVIT View of the Core-Collapsed Globular Cluster NGC 6397

6.1 Introduction

NGC 6397, located at a distance of 2.3 kpc (Harris 1996, 2010 edition, hereafter H96), is the second closest GC to us. This is a 12.6 Gyr old (Correnti et al. 2018), metal-poor system with [Fe/H] $= -2.02$ dex (H96). It has undergone core-collapse (Djorgovski & King 1986) and exhibits mass segregation (King et al. 1998; De Marchi et al. 2000; Andreuzzi et al. 2004).

NGC 6397 is a treasure trove of stellar exotica. *Chandra* X-ray observations by Grindlay et al. (2001) and Bogdanov et al. (2010) led to the detection of 79 X-ray sources within the half-mass radius of the cluster. Shara et al. (2005) using the WFPC2 and STIS UV imaging detected dwarf nova eruptions in two cataclysmic variables[*] (CVs) within the cluster. Strickler et al. (2009) suggested the presence of at least 24 He-core WDs in the central region of the cluster, in addition to the CO WD population. Dieball et al. (2017) studied the core region of the cluster (25″ × 25″) in the FUV using the *HST*/STIS FUV-MAMA detector and the F25QTZ filter and in the NUV (FOV of 162″ × 162″) using the WFC3 UVIS/F225W filter. Their study focused on the BSSs, WDs, and CVs and found that BSSs and CVs are the most centrally concentrated populations.

In this chapter, the FUV observations of NGC 6397 carried out using UVIT are presented, along with an analysis of UV-bright members of this cluster. The observations cover almost the entire tidal radius of the GC (15.8′; Harris 1996, 2010 edition).

6.2 Observations And Data Reduction

NGC 6397 was observed using UVIT under the GlobUleS program on 6 July 2021 in two FUV filters, F148W and F169M. The science-ready images (L2 products) downloaded from the ISSDC webpage were used in this work. The details of the UVIT observations are given in Table 6.1. The astrometric calibration of the UVIT images was carried out as explained in Chapter 2. Figure 6.1 shows the image of the cluster in the UVIT F169M filter. The UVIT imaging covers the sources within almost the entire tidal radius of NGC 6397.

---

[*] Interacting binaries consisting of a WD primary accreting material from a low-mass secondary star.

TABLE 6.1: UVIT observation details

Filter	λ_{mean} (Å)	$\Delta\lambda$ (Å)	Zero point (mag)	Exp. time (s)
F148W	1481	500	18.097	3265.3
F169M	1608	290	17.410	3156.9

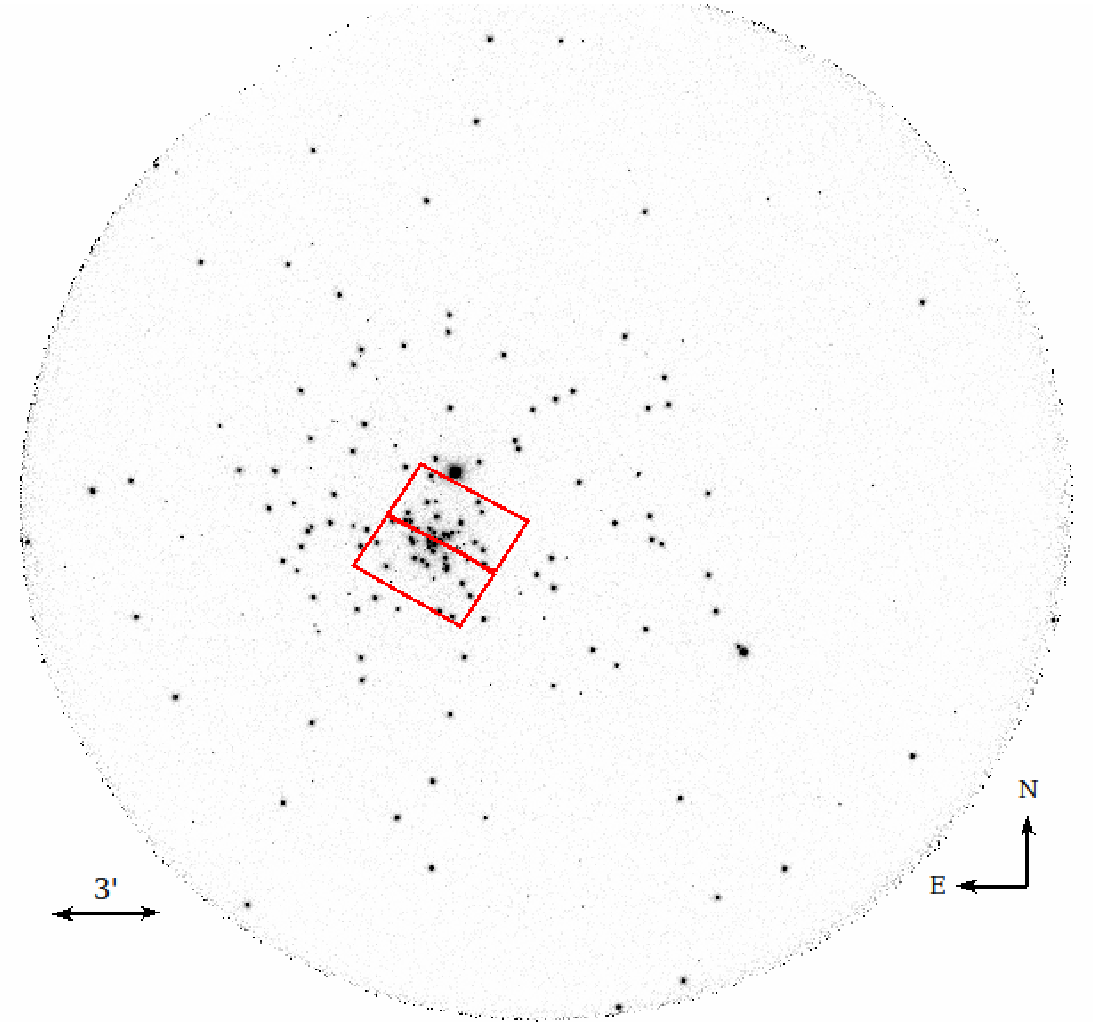

FIGURE 6.1: The UVIT image of NGC 6397 in the F169M filter. The FOV covered by the *HST* ACS/WFC ($\sim 3\rlap{.}'4 \times 3\rlap{.}'4$) is shown in red color.

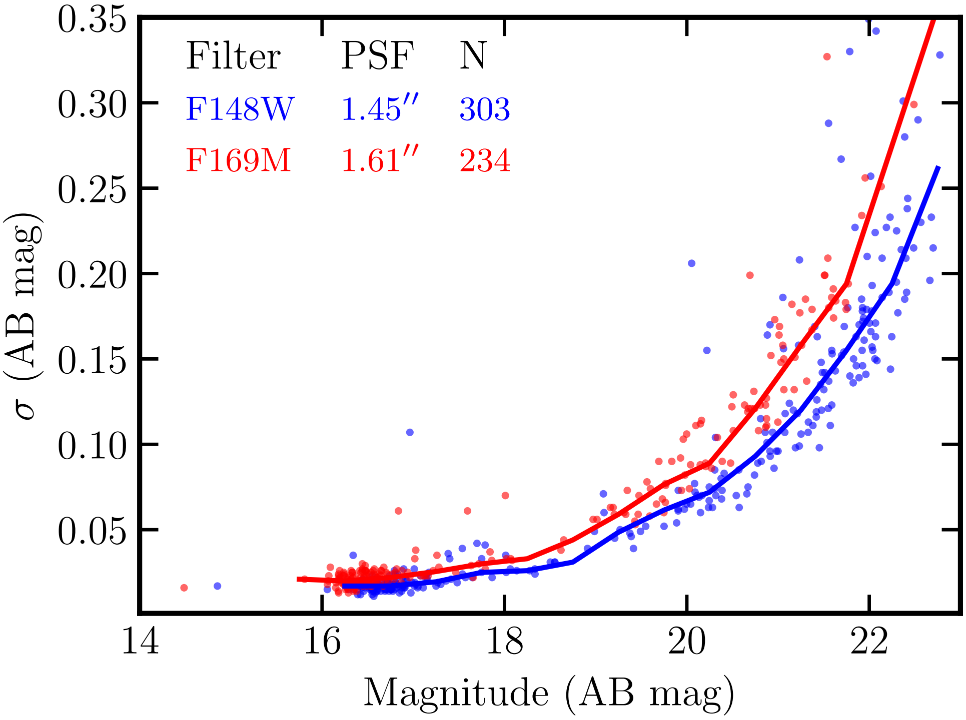

FIGURE 6.2: The PSF-fit errors vs. magnitudes (not corrected for extinction) for the UVIT observations of NGC 6397 in two FUV filters. The filter names, FWHM of the PSF, and the number of stars detected in each filter are indicated in the figure. The line represents the median error in each filter.

6.2.1 Photometry

The photometric analysis was undertaken on the UVIT images as described in Chapter 2. The catalogs were refined by removing one visibly saturated star at R. A. = 265.1601°, Decl. = −53.6420°, and the objects lying at the edge of the instrument FOV. The saturated star is identified to be the post-AGB star ROB 162 (Caloi et al. 1982; Heber & Kudritzki 1986). Fig. 6.2 shows a plot of how the PSF-fit errors vary with the magnitude in both UVIT filters. The filter names, the FWHM of the PSF, and the number of stars detected are also indicated in the figure. About 221 sources were found to be common among the two FUV filters.

6.2.2 Extinction Correction

The magnitudes were corrected for extinction by adopting the reddening value of $E(B-V) = 0.18$ mag (Harris 1996, 2010 edition) and $R_V = 3.1$. The extinction coefficients in the UVIT filters were obtained assuming the Fitzpatrick reddening law (Fitzpatrick 1999), using the York Extinction Solver (McCall 2004). The values are $\mathrm{A}_{F148W} = 1.47$ mag and $\mathrm{A}_{F169M} = 1.40$ mag.

6.3 Identification Of Optical Counterparts Of UVIT Detections

6.3.1 UVIT-*HST* cross-match

For identifying the optical counterparts of the sources detected in the UVIT images, at first, a cross-match with the HUGS catalog (Nardiello et al. 2018; Piotto et al. 2015) was performed. This catalog covers the inner region of the cluster (within $\sim 3\farcm4 \times 3\farcm4$). A subset of stars that are expected to be bright in the UV, such as the HB, WDs, and BSSs, were chosen from the HUGS photometry (method 1) for cross-match. This HST subset was matched with the UVIT catalog with a maximum match radius of $0\farcs7$, using TOPCAT, and about 73 stars were found to have unique counterparts. Although for some of the sources, the membership probability value was unknown (assigned as -1.0), these were not excluded from the catalog. Only one source, which had membership probability = 0.0, was excluded.

6.3.2 UVIT-Ground Data-Gaia EDR3 Cross-Match

In order to identify the optical counterparts of UV-bright sources outside the *HST* FOV (hereafter, outer region), the ground-based optical dataset from Stetson et al. (2019) and the *Gaia* EDR3-based catalog from Vasiliev & Baumgardt (2021) were used. The number of stars common between UVIT and ground-based catalogs was about 188. For selecting the cluster members among them, this set was matched further with the *Gaia* EDR3-based catalog of Vasiliev & Baumgardt (2021). About 104 stars were found to have a membership probability of more than 0.5. There were about 21 UV-bright stars that were not present in the *Gaia* EDR3 catalog and hence with unknown membership status. The remaining 63 were found to be non-members (membership probability $\simeq 0.0$) and were excluded from the catalog. Thus, the final UVIT catalog for the outer region includes 125 possible member stars.

6.4 Color-Magnitude Diagrams

From the previous steps, the optical counterparts of a total of 197 FUV sources from the UVIT catalog were identified. Out of these, 72 were located within HST FOV (hereafter, inner region), and 125 objects were outside. In order to plot all these sources in similar color-magnitude planes, the Johnson-Cousins B, V, and I magnitudes of the stars in the outer region were transformed to the corresponding HST filters (namely, $F438W$, $F606W$, and $F814W$), using the transformation equations from Sirianni et al. (2005) and Harris (2018).

The optical and FUV-optical CMDs of the 197 FUV sources that are possible cluster members are shown in Fig. 6.3. The F438W magnitudes used here have been converted to the AB system from the Vega system. The top panels of the

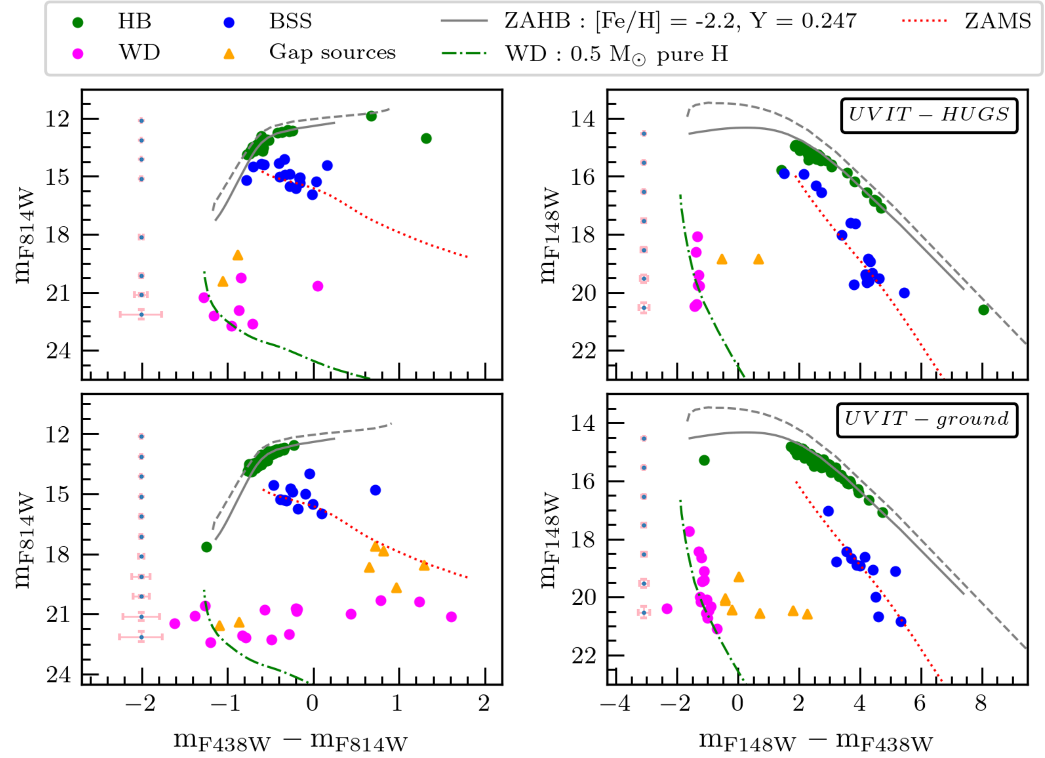

FIGURE 6.3: The optical and FUV-optical CMDs for the 197 possible cluster members. The stars matched with the HUGS dataset are shown in the top panels. The bottom panels show the CMDs for stars lying in the outer region. The median photometric errors in each magnitude bin are also shown along the left side of each plot.

figure show the UVIT detections matched with the HUGS dataset, and the bottom panels show the CMDs for the sources outside the HST FOV, which were cross-identified using the ground-based optical catalog of Stetson et al. (2019). The CMDs are overplotted with various models, and isochrone having parameters close to the value of the cluster to confirm the nature of different stellar sequences. They are briefly described below.

1. *BaSTI-IAC HB models*: For the sources along the HB sequence, the updated BaSTI-IAC (Pietrinferni et al. 2021) theoretical ZAHB and TAHB models downloaded from their webpage were used. The α-enhanced models with $[\alpha/Fe]$=+0.4 dex, [Fe/H] = −2.2 dex, Y = 0.247 were adopted. In these

models, the mass-loss parameter $\eta = 0.3$ and atomic diffusion effects were included, and overshooting was not applied.

2. *BaSTI-IAC isochrone*: In order to delineate the BSS sequence, the BaSTI-IAC ZAMS isochrone of age = 0.5 Gyr, with initial mass range $\sim$ 0.5-1.5 $M_{\odot}$ close to the cluster metallicity, [Fe/H]=-2.2 dex and primordial helium abundance was used.

3. *WD cooling models*: The DA spectral type WD model (Bergeron et al. 1995; Tremblay et al. 2011; Bédard et al. 2020) with pure hydrogen (H) grid and thick H layers of mass 0.5 $M_{\odot}$ was used (Pierre Bergeron, in private comm).

The observed stellar sequences are found to match well with the predictions of the theoretical models and isochrone. The main FUV-bright sources in the cluster are HB stars, BSSs, WDs, and a few gap objects (those lying between the BSS and the WD sequences in the FUV-optical CMDs). The sources in the gap region could be binary systems with WD and MS/giant companions (Knigge et al. 2002). Table 6.2 tabulates the number of stars belonging to different categories detected in each UVIT filter.

Figure 6.4 shows the FUV-optical CMD of all the UVIT detections, highlighting the sources cross-matched with other works from the literature. The stars in the inner region are represented with grey-filled circles, and those in the outer region are demarcated with red square boundaries. The effective temperatures derived through cubic spline interpolation of the (F148W-F438W) vs. T_{eff} relation from the BaSTI-IAC ZAHB models are shown above the HB tracks. The effective temperatures of WDs derived from the WD cooling track are also shown. The following section describes the details of the detected stellar populations and their cross-identification with other works from the literature.

Table 6.2: The number of HB stars, BSSs, WDs, and gap objects detected in the inner and outer regions of the cluster.

Category	Inner region	Outer region
HB	45	85
BSS	17	12
WD	8	21
Gap objects	2	7

6.5 Detected FUV Sources

- **HB stars**: A total of 130 HB stars were detected, out of which 45 are located in the inner region and 85 in the outer region. For the inner region, our number matches closely with the number reported by Dieball et al. (2017) based on HST/ACS observations. From the top right panel of Fig. 6.3, all of the inner HB stars are found to be located below the knee point in the FUV-optical CMD, which corresponds to an effective temperature of $\sim 11\,500\,\mathrm{K}$ from Fig. 6.4. From the bottom right panel of Fig. 6.3, all the outer HB stars, except one, are found to be located below the knee point in the FUV-optical CMD. There is one outer HB star at $T_{\mathrm{eff}} \sim 30\,000\,\mathrm{K}$ as can be seen from Fig. 6.4 and is most likely an EHB star. Lovisi et al. (2012) carried out the high-resolution (R $\sim$ 20 000 to 33 000) spectroscopic study of 42 HB stars in the cluster using the GIRAFFE spectrograph on VLT (λ range: 370-900 nm) and estimated rotational velocities and abundances of elements like iron, magnesium, and oxygen. The authors derived the atmospheric parameters photometrically by comparing the locations of these sources on the CMD with theoretical models. Out of these, 40 could be cross-matched with our sample.

- **BSSs**: About 29 FUV-bright BSS candidates were found in the sample. These sources span a significant range of FUV magnitudes, from 16 to 20.5 mag. The sample of Lovisi et al. (2012) also included 18 BSSs, out of which 14 were found to be common with our sample. These are indicated with blue star symbols in Fig. 6.4. Among these, 4 were found to be SX Phe variables and one similar to γ Doradus class of population I variables. These are demarcated with filled green circles in the figure. Their variability was also reported in the studies by Kaluzny & Thompson (2003); De Marco et al. (2005); Ahumada et al. (2021). Two BSSs were also found to have X-ray counterparts from the catalog published by Cohn et al. (2010), and these are highlighted with yellow-filled circles in Fig 6.4.

- **WDs and gap objects**: A total of 29 candidate WDs and 9 gap objects were detected. Among these, three He-core WD candidates were found through a cross-match with the catalog of Strickler et al. (2009), which are shown with orange square symbols in Fig 6.4 — two in the gap region which are also confirmed cluster members (UVIT_052 and UVIT_092) and one near the WD track with unknown membership status (UVIT_256). Spatially, these are located within the HST FOV. Out of the remaining 7 gap sources, 4 have a membership probability greater than 0.9, and the status of others is unknown. Among the 29 WD candidates, the cluster membership status of only 5 is confirmed with a probability greater than 0.9. The membership probability values of others are unavailable.

In order to understand the true nature of the FUV-bright sources in the CMD, their physical properties were derived as described in the next section.

6.6 Characterization Using SED-Fitting

The SED-fitting technique was utilized to characterize the FUV-detected stellar populations. The SEDs were constructed and fitted with appropriate models using VOSA (Bayo et al. 2008) as described in Chapter 2. For the sources in the inner

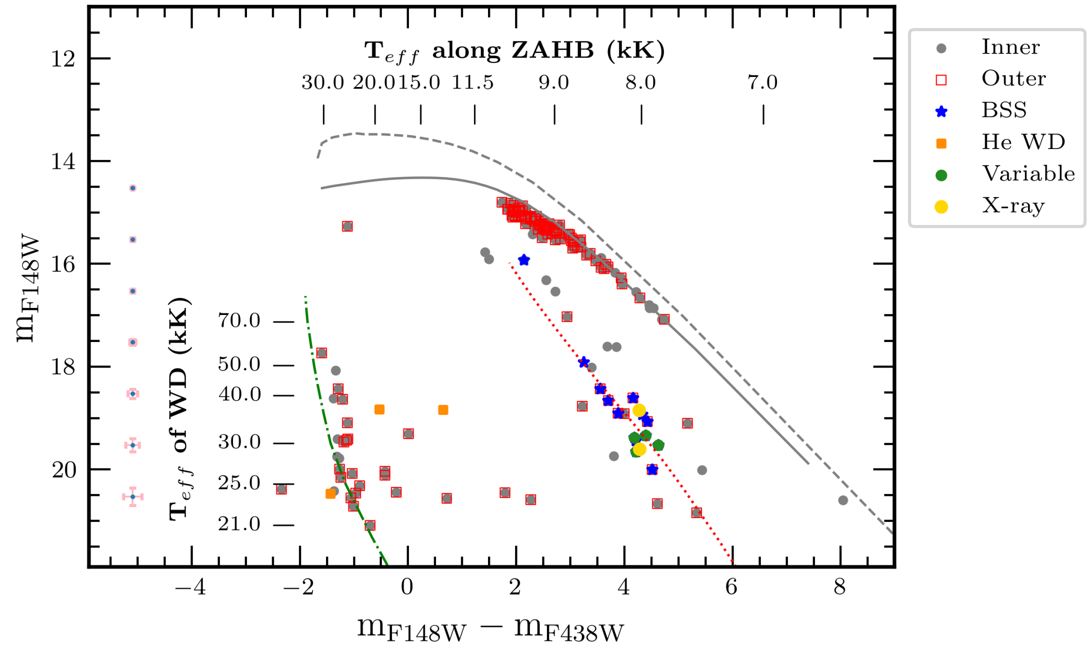

Figure 6.4: The FUV-optical CMD of the entire cluster region highlighting the exotic sources cross-identified from literature. The stars in the inner region of the cluster are represented with grey-filled circles, and those in the outer region are demarcated with red square boundaries. The effective temperatures of HB stars and WDs derived from theoretical models are also shown.

region, photometric data points from the UVIT and the HUGS catalog were used to construct the SEDs. For those in the outer region, SEDs were constructed using UVIT, the ground-based dataset from the catalog of Stetson et al. (2019), the public *GALEX* FUV dataset[†] and the available VO photometric values from VOSA. The data points that deviated considerably from the SED were excluded from the fit. Thus, for the sources within the inner (outer) region, the total number of data points ranged from 5 to 7 (5 to 94). The details of the SED models and the results for all the sources are described in the following subsections.

[†] Downloaded from the STScI MAST Archive

6.6.1 Properties Of HB Stars

The SEDs of HB stars were fitted by choosing the Kurucz stellar atmospheric models with $[\alpha/Fe] = 0.4\,\mathrm{dex}$ (Castelli & Kurucz 2003). The [Fe/H] parameter was fixed at -2.0 dex, $\log g$ value restricted within the range 2 to 5 dex, and the full range of T_{eff} values available was chosen. The fits were good, with $V_{gfb} < 15$ (Rebassa-Mansergas et al. 2021), for all the HB stars except one (ID: UVIT_071). The SED-fit parameters of HB stars were found to lie within the following ranges: T_{eff} from 6250 to 29 000 K with only one star having $T_{\mathrm{eff}} > 11\,000$ K; bolometric luminosity from $\sim$ 11 to 59 $L_{\odot}$ and radius from 0.13 to 6.55 $R_{\odot}$. As examples, the SED-fits for two HB stars are shown in Fig. 6.5. The median T_{eff} difference for the 40 HB stars common with the sample of Lovisi et al. (2012) is found to be $(T_{Lovisi} - T_{SED})_{median} = 532$ K.

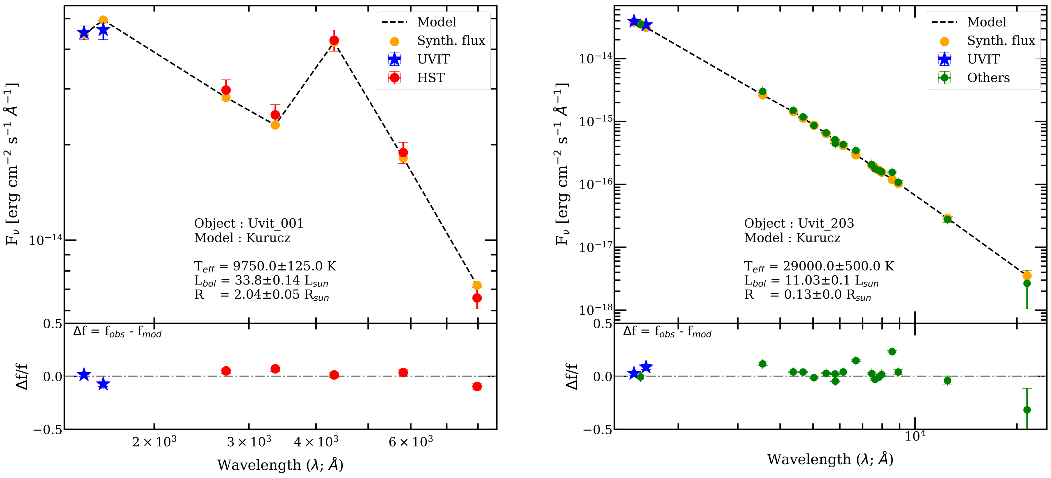

FIGURE 6.5: SEDs of two HB stars, UVIT_001 (located within the inner region) and UVIT_203 (EHB candidate located in the outer region). The 3-sigma error bars for each data point are also shown.

6.6.2 BSS Properties

Out of the 29 BSSs, SEDs were not constructed for the 5 known BSS variables as the multi-wavelength datasets were obtained at different epochs. The SEDs of the remaining 24 BSSs were first fitted with Kurucz models with $[\alpha/Fe] = 0.4$ dex (CK03). The [Fe/H] parameter was fixed at -2.0 dex, $\log g$ value restricted within the range 3 to 5 dex, and the full range of $T_{\rm eff}$ values available was chosen. The SEDs of 15 BSSs were fitted well with single-component models. The examples of two such sources (UVIT_061 and UVIT_089) are shown in Fig. 6.6, which also include the fractional residual ($[F_{obs} - F_{mod}]/F_{obs}$) corresponding to each data point in the bottom panel. The best-fit parameters of these sources are tabulated in Table 6.3.

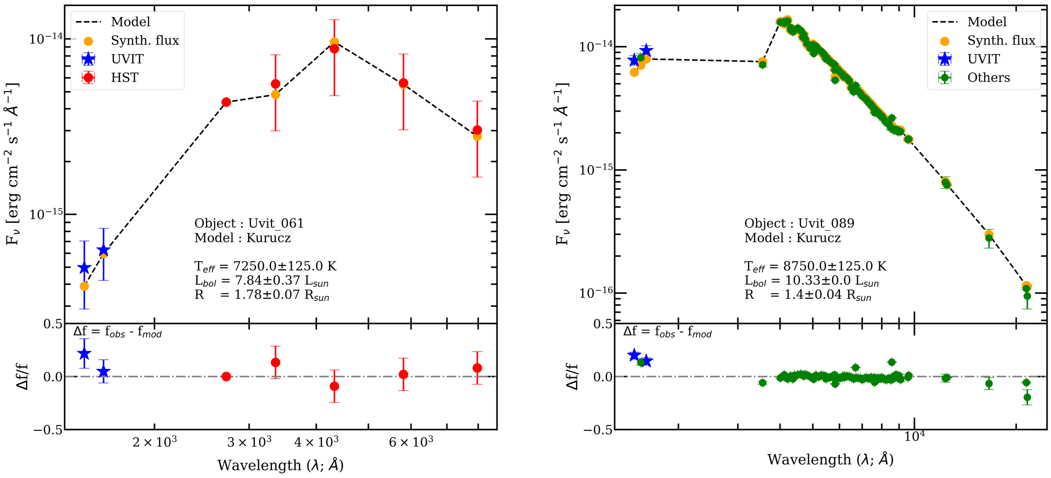

FIGURE 6.6: SEDs of the single-component fits for two BSS candidates, UVIT_061 (located within the inner region) and UVIT_089 (located in the outer region).

About 7 BSSs showed excess flux in the UV regime with residual > 0.5 in more than one FUV data point, indicating the need for double-component SED fits involving a combination of hot and cool models. The cool component was fitted using Kurucz models and the hot component using Koester WD models (Koester 2010) fixing the $\log g$ value at 7.75 dex and radii in the range 0.01 to 0.03 $R_\odot$. Good fits were achieved only for the two sources shown in Fig. 6.7. For these sources, the

Table 6.3: The best-fit SED parameters of single-component BSSs.

Object	R. A. (degrees)	Decl. (degrees)	S. L.	M. P.	$T_{\rm eff}$ (K)	e_$T_{\rm eff}$ (K)	$L_{\rm bol}$ ($L_\odot$)	e_$L_{\rm bol}$ ($L_\odot$)	Radius ($R_\odot$)	e_Radius ($R_\odot$)	Vgf	Vgf_b	N_{fit}	N_{tot}
Uvit_020	265.1757	-53.6722	I	0.98	8250	125.0	6.562	0.002	1.254	0.038	4.67	4.15	7	7
Uvit_023	265.1940	-53.6695	I	0.99	8000	125.0	3.602	0.003	0.988	0.031	8.25	3.98	7	7
Uvit_056	265.1757	-53.6746	I	0.94	10000	125.0	15.504	0.092	1.312	0.033	15.09	2.29	7	7
Uvit_061	265.1713	-53.6523	I	0.97	7250	125.0	7.844	0.372	1.775	0.074	1.00	1.00	7	7
Uvit_064	265.1689	-53.6843	I	0.97	8500	125.0	6.280	0.042	1.156	0.034	6.85	1.84	7	7
Uvit_065	265.1775	-53.6462	I	0.98	8250	125.0	6.448	0.041	1.243	0.038	13.85	5.29	7	7
Uvit_070	265.1772	-53.6756	I	0.97	9250	125.0	13.195	0.147	1.414	0.039	0.30	0.12	7	7
Uvit_090	265.1767	-53.6750	I	0.99	11750	125.0	11.230	0.109	0.809	0.018	8.68	2.82	7	7
Uvit_155	265.1749	-53.6738	I	0.96	8500	125.0	11.807	0.173	1.584	0.048	6.44	2.89	7	7
Uvit_252	265.1763	-53.6754	I	0.84	9500	125.0	14.319	0.107	1.397	0.037	1.19	0.21	6	6
Uvit_268	265.1752	-53.6741	I	0.99	8250	125.0	13.668	0.170	1.810	0.056	1.57	0.61	6	6
Uvit_089	265.2671	-53.7155	O	1.00	8750	125.0	10.331	0.001	1.399	0.040	2.93	0.21	89	89
Uvit_148	265.2285	-53.5721	O	1.00	7750	125.0	6.168	0.001	1.378	0.044	2.99	0.55	89	89
Uvit_162	265.0626	-53.8209	O	1.00	7750	125.0	5.359	0.001	1.284	0.041	3.00	0.69	89	89
Uvit_191	265.1031	-53.8374	O	1.00	7250	125.0	12.666	0.001	2.256	0.078	3.32	0.56	90	90

Notes. S. L. stands for spatial location, and I (O) indicates the inner (outer) region. M. P. is the cluster membership probability.

residuals for all the data points were minimal when using two-component fits. The reduced chi square (χ^2_{red}) value indicated in the plots is the Vgf value described in Chapter 2. The best-fit parameters for these sources are tabulated in Table 6.4.

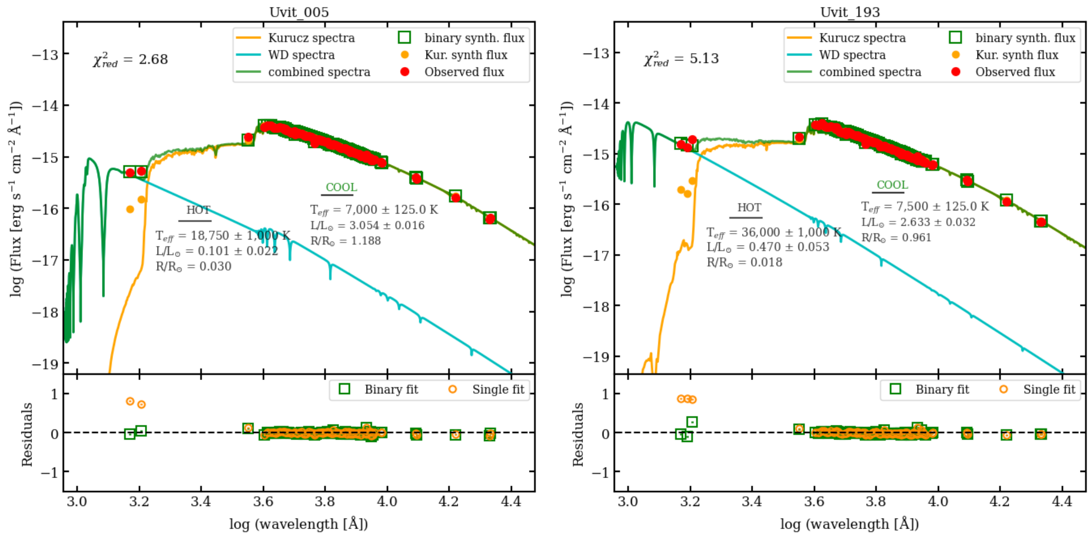

Figure 6.7: Two-component SED fits for the BSS sources UVIT_005 and UVIT_193.

Table 6.4: Parameters from the two-component SED fits for the BSS sources UVIT_005 and UVIT_193.

Source	Component	T_{eff} (K)	L_{bol} ($L_\odot$)	Radius ($R_\odot$)
UVIT_005	Hot	18 750 ± 1000	0.101 ± 0.022	0.03
	Cool	7000 ± 125	3.054 ± 0.016	1.188
UVIT_193	Hot	36 000 ± 1000	0.470 ± 0.053	0.018
	Cool	7500 ± 125	2.633 ± 0.032	0.961

Although two additional sources showed evidence of UV-excess, these could not be analyzed further as each had only one FUV data point.

6.6.3 Properties Of WD Candidates And Gap Sources

To fit the SEDs of WD candidates, Koester (Koester 2010) and Levenhagen (Levenhagen et al. 2017) models were used, employing the full ranges of T_{eff} and $\log g$ values available. Among the 29 candidates, 4 sources (UVIT_234, UVIT_238, UVIT_270, UVIT_275) did not have a sufficient number of photometric data points to fit the SEDs. The SED-fits of the remaining 25 sources were good (with Vgf_b < 15). The SEDs of two WDs that are confirmed cluster members are shown in Fig. 6.8. The parameters of all the sources with good fits are tabulated in Table 6.5.

The SEDs of the He-WD candidates that are cluster members and located in the gap region of the CMD (UVIT_052 and UVIT_092) were also fitted by choosing the Koester and Levenhagen models. The SEDs of these sources, along with the other He-WD candidate, UVIT_256, are shown in Fig. 6.9. One of the FUV photometric points is found to match with the model within errors in all the three cases.

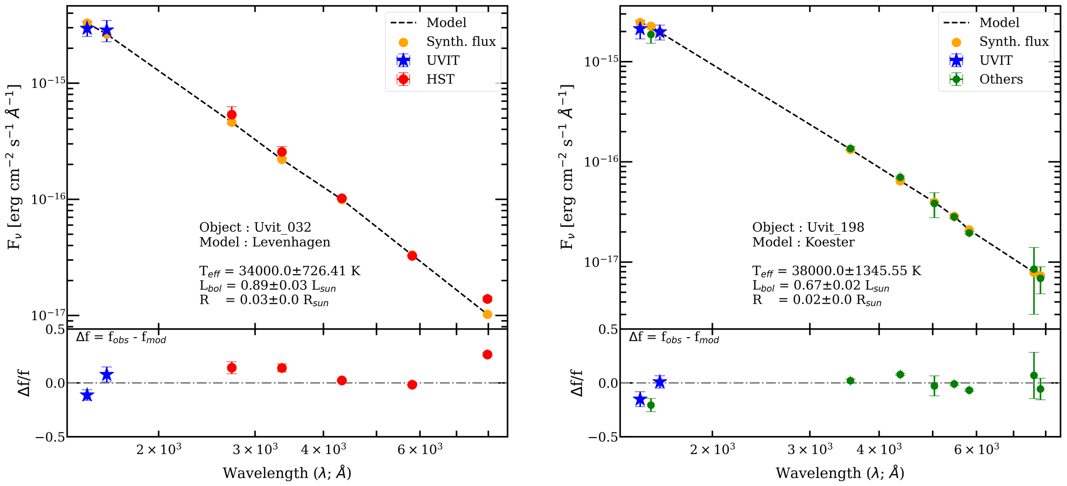

FIGURE 6.8: SEDs of WDs UVIT_032 and UVIT_198 that are confirmed cluster members. The former is located in the inner region of the cluster and the latter in the outer region.

However, the other FUV data point appears fainter than the models as evident in the cases of UVIT_052 and UVIT_092. Hence, the physical properties derived from the SED-fit of these sources are to be considered with caution. We require more data points in the UV regime to conclude firmly whether the mismatch with models is due to any physical reason.

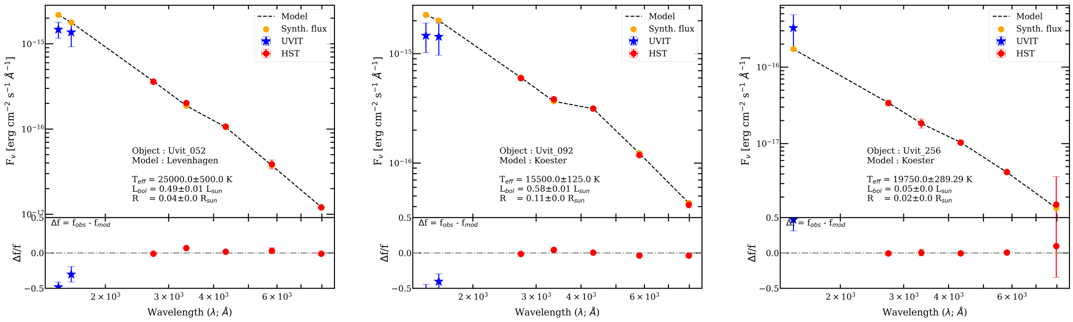

FIGURE 6.9: SEDs of the three He-core WD candidates identified using the catalog of Strickler et al. (2009).

Since gap sources could be binaries consisting of MS/giant and WD components, to fit the SEDs of the 4 remaining ones that are cluster members, we first used Kurucz models. The [Fe/H] was fixed to -2.0 dex, and the full ranges of $T_{\rm eff}$ and $\log g$ parameters were employed. The SEDs of all 4 sources showed UV-excess. However, there was only one FUV data point each in the case of 3 sources and

TABLE 6.5: The best-fit SED parameters of candidate WDs.

Object	R. A.	Decl.	S. L.	M. P.	Model	$T_{\rm eff}$	e_$T_{\rm eff}$	$L_{\rm bol}$	e_$L_{\rm bol}$	Radius	e_Radius	Vgf	Vgf_b	N$_{fit}$	N$_{tot}$
	(degrees)	(degrees)				(K)	(K)	(L$_\odot$)	(L$_\odot$)	(R$_\odot$)	(R$_\odot$)				
Uvit_032	265.1588	-53.6765	I	0.97	L	34000	726	0.885	0.025	0.027	0.001	50.41	3.19	7	7
Uvit_099	265.1534	-53.6755	I	–	L	44000	1237	0.595	0.008	0.013	0.001	18.26	7.33	7	7
Uvit_123	265.2067	-53.6877	I	–	K	30000	750	0.168	0.002	0.015	0.001	3.43	3.39	6	6
Uvit_223	265.1990	-53.6565	I	–	L	30000	1079	0.142	0.007	0.014	0.001	0.58	0.56	6	6
Uvit_228	265.1568	-53.6637	I	–	L	30000	698	0.148	0.006	0.014	0.001	4.05	0.70	6	6
Uvit_241	265.2121	-53.6816	I	–	K	22000	1397	0.055	0.003	0.016	0.002	3.07	2.94	6	6
Uvit_256	265.2047	-53.6772	I	–	K	19750	289	0.049	0.001	0.019	0.001	2.98	2.91	6	6
Uvit_269	265.1745	-53.6734	I	0.97	K	32000	1982	0.246	0.006	0.016	0.002	1.02	0.46	5	6
Uvit_048	265.0359	-53.6135	O	–	K	21000	1241	0.051	0.004	0.017	0.002	1.23	1.19	7	7
Uvit_073	265.1333	-53.5695	O	–	K	24000	1218	0.099	0.008	0.018	0.002	0.70	0.69	7	7
Uvit_082	265.1715	-53.6253	O	–	K	22000	836	0.172	0.008	0.029	0.002	2.09	0.62	5	6
Uvit_103	265.1097	-53.6979	O	1.00	K	50000	4844	1.216	0.051	0.015	0.003	5.80	1.16	7	7
Uvit_108	265.3413	-53.6347	O	–	K	23000	764	0.164	0.007	0.025	0.002	0.73	0.23	6	7
Uvit_141	265.0464	-53.6598	O	–	K	32000	1768	0.380	0.019	0.020	0.002	13.64	4.19	6	6
Uvit_147	265.2336	-53.5884	O	–	K	35000	783	0.521	0.010	0.020	0.001	12.24	1.39	7	7
Uvit_164	265.3577	-53.6712	O	–	K	23000	907	0.173	0.009	0.026	0.002	2.61	1.98	6	7
Uvit_184	265.1138	-53.8068	O	–	L	29000	1333	0.098	0.007	0.012	0.001	0.50	0.50	6	7
Uvit_198	265.2493	-53.4777	O	0.99	K	38000	1346	0.671	0.016	0.019	0.001	6.37	1.17	10	10
Uvit_230	265.0680	-53.5724	O	1.00	K	21000	978	0.092	0.006	0.023	0.002	1.67	0.35	5	5
Uvit_231	264.9472	-53.5241	O	–	K	26000	1181	0.112	0.007	0.016	0.002	1.79	1.20	5	5
Uvit_237	265.2136	-53.7783	O	–	K	19000	419	0.039	0.001	0.018	0.001	0.90	0.88	5	5
Uvit_239	264.8821	-53.7424	O	–	L	27000	1476	0.078	0.006	0.013	0.001	0.36	0.33	5	5
Uvit_258	265.0632	-53.4957	O	–	K	25000	1373	0.074	0.006	0.015	0.002	0.51	0.50	5	5
Uvit_262	265.2537	-53.5568	O	–	K	24000	1374	0.084	0.007	0.017	0.002	0.31	0.26	4	5
Uvit_263	265.3021	-53.8129	O	–	L	25000	764	0.056	0.002	0.013	0.001	0.86	0.86	5	5

Notes. In the column 'Model', K stands for Koester and L for Levenhagen.

hence could not be fit with two-component models. For the remaining gap source, although there were 3 FUV data points available (including *GALEX* FUV), a satisfactory result could not be achieved using double-component fitting.

6.7 H-R Diagram And Evolutionary Status

Fig. 6.10 shows the comparison of BSS and WD properties derived from SED-fitting with available theoretical evolutionary sequences on the H-R diagram. The dash-dotted lines represent WD cooling tracks for the various masses as indicated above each track. The 0.54 $M_\odot$ track corresponds to a CO-core DA WD having $Z = 0.000$ dex obtained from the BASTI-IAC database (Salaris et al. 2022). The others are low-mass He-core WD tracks (without diffusion and rotation effects) from Istrate et al. (2016), corresponding to $Z = 0.0002$ dex. The solid sequences represent the BASTI-IAC isochrones of different ages ranging from 2-12.6 Gyr with $[\alpha/Fe] = 0.4$ dex, [Fe/H] $= -2.2$ dex and $Y = 0.247$ (Pietrinferni et al. 2021).

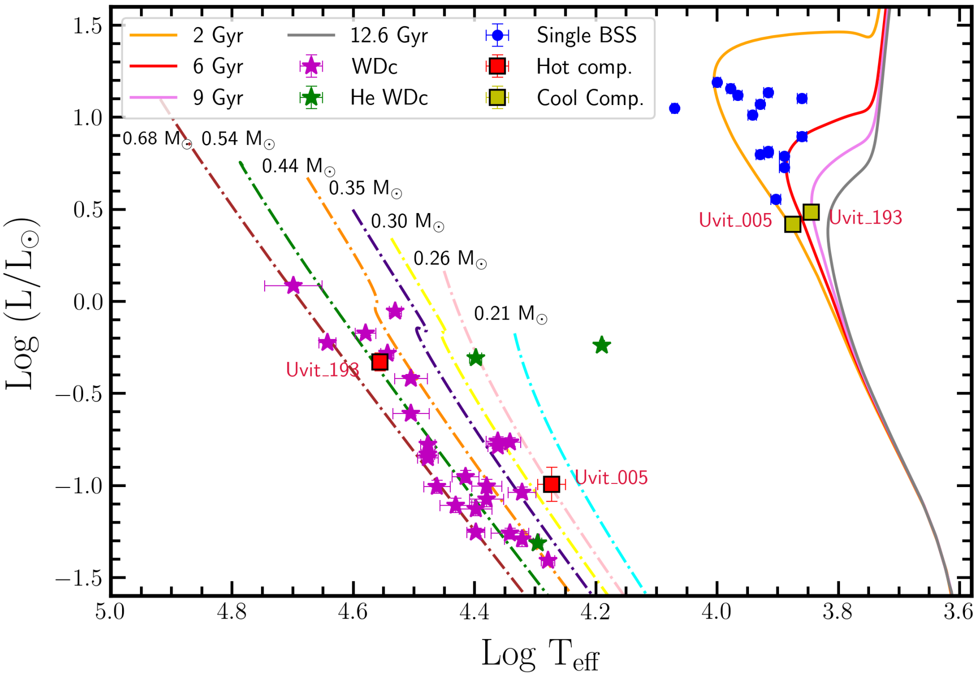

FIGURE 6.10: H-R diagram showing the comparison of BSS and WD properties derived from SED-fitting with available theoretical evolutionary sequences. The dash-dotted lines represent the CO-core (0.54 $M_\odot$, 0.68 $M_\odot$) and He-core WD cooling tracks with the corresponding masses indicated above each track. The solid sequences represent the BASTI-IAC isochrones of different ages as indicated in the legend. The hot and cool components of the BSSs with double-component SED fits are shown in red and yellow squares, respectively.

The BSSs with single-component SED fits are marked with blue squares. They are found to be located above the MSTO with ages ranging from 2-6 Gyrs based on their positions on the isochrones. The masses of these sources, based on the isochrones, range from 0.96-1.3 $M_\odot$. There is one BSS that lies outside the range of the isochrones.

The BSSs with double-component SED fits are shown using yellow square symbols, along with their IDs, and their hot companions are shown using red squares. UVIT_005 is a BSS with age $\sim$ 9 Gyr having a mass of 0.83 $M_\odot$ whose companion is found to be a low-mass WD with mass $\sim$ 0.26 $M_\odot$. UVIT_193 has an age of 3 Gyr with mass $\sim$ 0.98 $M_\odot$. Its companion is a CO-core WD of mass $\sim$ 0.5 $M_\odot$.

The candidate WDs are depicted using magenta star symbols. A majority are located in the mass range between 0.44-0.68 $M_\odot$. Some are probable low-mass He-core WDs with masses in the range $\sim$ 0.2-0.44 $M_\odot$. The three He-core WD candidates cross-identified from the catalog of Strickler et al. (2009) are marked using green star symbols. Two of these are found to lie along the 0.21 $M_\odot$ and 0.44 $M_\odot$ He-WD tracks from Istrate et al. (2016). One is found to be cooler than the parameter space of the WD tracks. However, caution is to be exercised in the interpretation of these sources as their SED-fits showed considerable fractional residuals in the UV regime.

6.8 Discussion

Dieball et al. (2017) presented the first FUV$-$NUV CMD of NGC 6397 using HST STIS FUV imaging, complemented by WFC3 NUV and ACS optical data. The FUV field, however, covered only the $25'' \times 25''$ central region of the cluster. BSSs were found to be the most centrally concentrated population, followed by CVs, whereas HB stars were found to be the least concentrated. However, the complete catalog of FUV sources was not published and hence could not be cross-matched with our sample.

High-resolution spectroscopic studies of significant samples of HB stars (~ 40 sources) in this cluster were carried out by Lovisi et al. (2012) and Mucciarelli et al. (2014). Rotational velocities and abundances of chemical elements such as Fe, Mg, O, and He were measured from the spectra, whereas the atmospheric parameters (such as $T_{\rm eff}$, $\log g$) were estimated photometrically. Our $T_{\rm eff}$ estimates from SED-fitting were found to agree reasonably well with values reported by Lovisi et al. (2012) (with a median difference of ~ 530 K) for the 40 stars common in both samples. Mucciarelli et al. (2014) calculated the He mass fraction, Y, to be 0.241±0.004 and did not find HB stars with significant He-enhancement.

In our sample, we identified one EHB candidate with a membership probability of 0.9, present in the cluster's outer extent, from the optical and FUV-optical CMDs, which has not been reported in previous studies. The $T_{\rm eff}$ of the source from the SED-fit confirms that it is hotter than the M-jump at $\sim 20\,000$ K.

Among the BSSs, the SEDs of 15 could be fit with single-component models. About 73% of these are located within the inner region of the cluster and could have formed through the collisional scenario. There were 7 BSSs that showed UV-excess in their SEDs. Through double-component SED-fits, we detected two BSSs having hot WD companions – UVIT_005 with a mass of 0.83 $M_\odot$ having a candidate He-core WD of mass ~ 0.26 $M_\odot$ as a companion and UVIT_193 with a mass of 0.98 $M_\odot$ having a CO-core WD of mass ~ 0.5 $M_\odot$ as companion. UVIT_005 corresponds to source 75241 in the catalog of Lovisi et al. (2012) and is not known to exhibit any variation in radial velocity. Both these BSS sources are located in the outer region of the cluster and could have formed through the MT channel. Similar binary BSS systems have been reported in the outer regions of other GCs such as NGC 5466 (Sahu et al. 2019), NGC 362 (Dattatrey et al. 2023) and in OpCs (e.g., Sindhu et al. 2019; Pandey et al. 2021; Jadhav et al. 2021). Spectroscopic studies in the future are required to constrain the parameters of these sources further and identify the MT mechanism.

Strickler et al. (2009) identified 24 He-core WD candidates in the cluster by comparing the positions of these sources on optical CMDs and from the $H_\alpha - R_{625}$ color. We were able to detect 3 of these sources, among which two were cluster members located in the gap region of the FUV-optical CMD. The SEDs of these sources were fitted with single-component models but showed considerable residuals in the UV regime. Nevertheless, the parameters derived from SED-fit fall within the range of low-mass He-core WD tracks from Istrate et al. (2016). However, these sources are most likely to have undetected companions as He-core WDs cannot form from single stellar evolution within the Hubble time (Brown et al. 2010b). Pichardo Marcano et al. (2023) reported the presence of a He-core WD candidate with magnetic spots in the cluster, the first of its kind in any GC. This source, however, was undetectable in our study.

This cluster is known to be a post-core-collapse cluster, and the presence of a large number of X-ray sources is probably connected with this. On the other hand, we do not detect a large number of binary BSSs, though a couple of them are known to be variables. Till now, there is no evidence of distinct BSS sequences in the CMDs of this cluster arising out of contributions from the collisional and MT pathways of formation, as reported in other core-collapsed clusters such as NGC 362 (Dalessandro et al. 2013; Dattatrey et al. 2023) and NGC 6256 (Cadelano et al. 2022). The existence of several He-core WDs and gap sources certainly indicates the presence of evolved binaries. We speculate that the cluster went through the core collapse sometime ago, resulting in the formation of binaries that evolved to form the above sources, including the X-ray sources.

6.9 Summary

The findings from this chapter are summarized below:

1. The FUV investigation of nearby, core-collapsed cluster NGC 6397 was undertaken using AstroSat/UVIT, covering the region from the cluster center up to the tidal radius. The optical counterparts of the UV sources and the cluster members were identified using cataloged data from *HST*, *Gaia EDR3*, and ground telescopes.

2. Out of the 197 FUV-bright probable cluster members with optical counterparts, 130 HB, 29 BSS, 29 WD candidates, and 9 gap sources were identified based on their locations on the UV-optical and optical CMDs. Among the BSSs, 5 variables and 2 X-ray sources were found through cross-match with other studies in the literature. Three candidate He-core WDs from the catalog of Strickler et al. (2009) were also found in the sample.

3. The fundamental parameters of most of the detected FUV-bright sources were derived through SED-fitting. All the HB stars except one were found to have $T_{\rm eff}$ $\lesssim$ 11 000 K. An EHB star candidate with $T_{\rm eff}$ = 29 000 K was detected in the outer region of the cluster.

4. The SEDs of 15 BSSs were fitted with single-component models. The ranges of derived parameters such as effective temperature, luminosity, and radius were 7250-11 750 K, 3.6-15.5 $L_\odot$ and 0.8-2.2 $R_\odot$ respectively. By comparing their positions on the H-R diagram with theoretical isochrones, the masses and ages of these sources were found to be ranging from $\sim$ 0.9-1.3 $M_\odot$ and 2-6 Gyrs, respectively.

5. About 7 BSSs showed UV-excess in their SEDs. Two of these could be successfully fitted with double-component models. By comparing the derived properties of the components on the H-R diagram with theoretical models, one of the BSSs (UVIT_005, with mass of 0.83 $M_\odot$) was found to have a low-mass WD companion (0.26 $M_\odot$) and another (UVIT_193, with mass of 0.98 $M_\odot$) to have a 0.5 $M_\odot$ CO-core WD companion. These systems were found to be located in the outer region

of the cluster and could have been formed through MT. Spectroscopic investigation of these exotic sources in the future can help achieve better constraints on their physical parameters and give clues on the type of MT mechanism.

6. The effective temperature, luminosity, and radius of the 25 WD candidates which had good SED-fits ranged from 19 000-50 000 K, 0.04-1.22 $L_{\odot}$ and 0.01-0.03 $R_{\odot}$, respectively. By comparing with theoretical models on the H-R diagram, the masses of these sources were found to range from 0.2-0.68 $M_{\odot}$ implying that some of these could be He-core WD candidates. The SED-fit parameters of 2 sources previously suggested to be He-core WD candidates by Strickler et al. (2009) were found to fall within the parameter space of low-mass He-WD models.

7. The study highlights the advantage of UV observations from a facility such as UVIT in the detection and characterization of exotic sources in GCs.

Chapter 7

Conclusions and Future Work

The stellar populations of GGCs have been thoroughly investigated in optical wavebands over the years. However, comprehensive photometric studies in the UV regime, especially in the FUV passbands covering regions of the cluster beyond the central core, have been limited due to the lack of suitable observational facilities. In this thesis, we present the detection and detailed analysis of the UV-bright stellar populations in three GGCs, mainly using UVIT onboard *AstroSat*. In order to identify their counterparts in the optical for generating CMDs and to separate cluster members from non-members, we used cataloged datasets based on *HST*, *Gaia* and ground-based telescopes. The primary goals were to characterize the relatively fast-paced, late evolutionary stages of low-mass stars in GGCs and understand the formation and evolution of non-canonical objects like BSSs. The GGC sample consisted of two massive and dense clusters, NGC 2808 and ω Centauri, which are also known to host stellar populations with significant He-enhancement. Additionally, one nearby, core-collapsed GC, NGC 6397, was chosen to explore exotic UV-bright stars. This chapter presents a summary of the important results from the thesis and the conclusions drawn from the work. In the end, a discussion on the projects planned to be carried out in the future is also included.

7.1 Summary And Conclusions

1. The rapidly progressing penultimate evolutionary stages of low-mass single stars were explored in Chapter 3 using the populations of the GGC NGC 2808 as a sample. A complete census of the pHB stars was carried out for the first time using UV imaging. FUV-optical and FUV-NUV CMDs were crucial in the identification of hot pHB stars. Using multi-wavelength photometry from UVIT and other published catalogs, the identified pHB stars were characterized through SED-fitting. As a test, SEDs were also fitted by excluding the available FUV data points. The results were found to significantly change for stars hotter than 40 000 K, highlighting the importance of FUV photometry in characterizing such objects. The $T_{\rm eff}$ values from SED-fit matched well with the available spectroscopic estimations for a few stars from the literature. On comparison of the estimated properties of these sources with theoretical pHB models, many of them were found to be AGB-manqué stars that have evolved from EHB progenitors. These are sources that have bypassed the AGB phase altogether after core-He-burning and are expected to progress directly to the WD stage. All except three of the hottest and the most luminous pHB stars were evolutionary products of HB stars with $\mathrm{M}_{ZAHB} < 0.53\ \mathrm{M}_{\odot}$. The maximum observed number of p(e)AGB stars detected in the cluster is in good agreement with the number expected from single-stellar evolutionary theory. The results from this study also have implications for understanding the properties of WDs in the cluster. The progeny of AGB-manqué and peAGB stars are suggested to be a new WD subclass known as “slow WDs” that have longer cooling times due to residual envelope hydrogen burning (Chen et al. 2021, 2022). Therefore, the detected AGB-manqué stars are excellent targets for future detailed studies regarding structure, evolution, and atmospheric properties.

2. The EHB stars, which were thought to have stable luminosities, were reported to be variables for the first time by Momany et al. (2020) using optical/U-band observations of three GGCs with different properties, NGC 2808, ω Centauri and NGC 6752. This variability was attributed to the α^2 CVn phenomenon wherein magnitude variations are caused by the projected rotation of surface spots (chemical inhomogeneities caused by atmospheric effects such as diffusion) stabilized by magnetic fields with low-strengths (about 100 G) generated by sub-surface HeII convective layer. Theory predicts that these spots will be dark in the FUV and bright in the optical, resulting in fainter FUV magnitudes. The main goal of the work presented in Chapter 4 was to analyze the UV properties of vEHBs in NGC 2808. In the FUV-optical CMD, about half of the vEHB stars were found to be sub-luminous compared to the theoretical ZAHB model. This finding is in agreement with the expectations from the suggested α^2 CVn mechanism. The vEHBs with the longest period were found to be the faintest in FUV and NUV, suggesting a tentative correlation between the UV magnitudes and the rotation periods reported by Momany et al. (2020). From the SED analysis of these sources, the slowest rotators were also found to have the smallest bolometric luminosities. However, these trends need further verification with a statistically significant sample of vEHBs from multiple GGCs.

3. ω Centauri, the most massive and complex GGC system, has been investigated in many works. Although this target has abundant space- and ground-based optical observations, its FUV data are scarce. Chapter 5 presents the first comprehensive investigation of this GGC in the FUV, extending from the cluster center to nearly 28% of its tidal radius. In the FUV-optical CMD, the bluest HB stars and the WDs exhibited peculiarities. These populations were fainter in the FUV by about 0.5 mag when compared to canonical models and in comparison with their counterparts in another GGC with similar overall properties, namely, M13. To shed light on the peculiar HB populations, HB morphologies were simulated simultaneously in the optical and FUV-optical planes adopting [Fe/H], age, and

Y as parameters. MSPs with at least five subpopulations, including three He-rich groups, were required to explain the observed HB distribution. The He-rich, younger subpopulations were found to be more centrally concentrated than the He-normal, older ones. These observations point to the origin of the second-generation stars in the system from the ejecta of intermediate-mass AGB stars. Physical parameters such as $T_{\rm eff}$, $L_{\rm bol}$, and radius were derived by fitting the multi-wavelength SEDs of 571 hot HB stars and 145 WDs. These were compared with the properties of similar sources in M13 on the H-R diagram, along with theoretical models. A fraction of the HB stars were found to have anomalously low luminosities and smaller radii, for which we currently do not have an explanation. The WDs' properties indicate that a fraction could be He-core WDs with masses in the range 0.44-0.46 $M_{\odot}$ that have evolved from He-enhanced progenitors, and some could be "slowly cooling" CO WDs evolved from EHB stars. The study demonstrates that multi-wavelength SED-fitting proves to be a useful tool to characterize sizable samples of stars in dense GCs where spectroscopic observations can be expensive in terms of time and accessibility.

4. In Chapter 6, the exotic FUV-bright stellar populations in the nearest core-collapsed GC, NGC 6397, were explored, covering almost the entire tidal radius. The major FUV-emitting cluster members were found to be HB stars, BSSs, WDs, and gap sources. By cross-matching with published catalogs, exotic sources such as SX Phe variables, counterparts to X-ray sources, and He-core WD candidates were identified. Most of the stellar populations were analyzed using SED fitting. All except one HB star was found to have $T_{\rm eff} < 11\,000$ K. An EHB star candidate with $T_{\rm eff}$ of $\sim 29\,000$ K was discovered in the cluster's outer extent for the first time. The SEDs of the majority of the BSSs could be fit with single-component models. A few BSSs were found to exhibit UV-excess. Among these, two sources in the outer region were found to have CO-core and He-core WD candidates as binary companions through double-component SED-fitting. These could have likely

formed via the MT scenario and needs to be confirmed from spectroscopic observations in the future. A fraction of FUV-bright WD candidates in the cluster were found to have masses ranging from 0.2-0.44 $M_{\odot}$, implying that these could be He-core WD candidates. It is important to carry out UV observations of more core-collapsed GCs to shed light on the properties and formation pathways of stellar exotica and their connection with the core-collapse process.

7.2 Future Directions

The works carried out in this thesis have naturally led to the following newer exciting projects for the future. I briefly discuss some of them below:

1. To widen our understanding of pHB evolution, there is a need for the detection and characterization of a number of such objects from a large GGC sample. As seen earlier, UV observations are crucial to obtain the complete census of hot pHB objects and to characterize them. The catalog of UV-bright stars in 11 GGCs observed under the GlobULeS program is currently available (Sahu et al. 2022), and a few more clusters have been proposed for observations in the future as part of the collaboration. A comparative study of the number statistics and properties of pHB stars in clusters with different HB morphologies can shed light on the possible correlation. It is also important to obtain the optical spectra of a significant number of bright pHB stars, which can be resolved using ground-based facilities such as the VLT in order to constrain their atmospheric parameters better. Spectroscopy can also help to look for signatures of third dredge-up which are pivotal in distinguishing pAGB stars from peAGB stars. In NGC 2808, 7 candidates in the outer region of the cluster have been identified that are ideal for spectroscopic follow-up. Chen et al. (2021, 2022) attributed the genesis of "slow WDs" to progenitors that do not undergo the third dredge-up, namely the

AGB-manqué and peAGB populations. A thorough investigation of pHB and WD populations in a large GC sample can thus also help shed light on the link between HB morphology and WD demographics.

2. In Chapter 4, the UV properties of the newly discovered vEHB stars in NGC 2808 were explored. However, the cadence of the data was insufficient to generate UV light curves and detect variability with a good S/N ratio. Hence, monitoring observations of this GC using UVIT (Proposal ID: A11_037) were proposed on 5 occasions, each with 5ks, separated by 15 days. The analysis of the first dataset is complete, and the remaining will be carried out in the near future. If FUV variability is detected, it will be an invaluable dataset to investigate the properties of the chemical spots suggested to be causing the variability and probe the role of surface magnetic fields in stabilizing these spots. It can also thus help clarify the importance of magnetic fields in the genesis and evolution of EHB stars.

3. In the study of ω Centauri presented in Chapter 5, the UVIT coverage was limited to only 28% of the cluster's tidal radius. However, there are a significant number of hot stars in the region outside the present FoV. Hence, observations of the outskirts of ω Centauri (extending up to $35'$ from the cluster center) with UVIT were proposed in the A13 cycle. This dataset will be combined with ground-based DECam optical catalog and *Gaia* DR3 data to identify optical counterparts and to select cluster members. The main goal is to map the spatial distribution of various subpopulations of ω Centauri and stars in different evolutionary phases, which can yield clues on the origin of the GC. We also plan to study the FUV properties of the vEHB stars in this cluster and compare them with those in NGC 2808.

Bibliography

Adamo, A., Zeidler, P., Kruijssen, J. M. D., et al. 2020, *Space Sci. Rev.*, 216, 69

Ahumada, J. A., Arellano Ferro, A., Bustos Fierro, I. H., et al. 2021, *New Astronomy*, 88, 101607

Althaus, L. G., De Gerónimo, F., Córsico, A., Torres, S., & García-Berro, E. 2017, *Astron. Astrophys.*, 597, A67

Anderson, J., Sarajedini, A., Bedin, L. R., et al. 2008, *Astron. J.*, 135, 2055

Andreuzzi, G., Testa, V., Marconi, G., et al. 2004, *Astron. Astrophys.*, 425, 509

Arellano Ferro, A., Ahumada, J. A., Bustos Fierro, I. H., Calderón, J. H., & Morrell, N. I. 2018, Astronomische Nachrichten, 339, 183

Arp, H. C. & Hartwick, F. D. A. 1971, *Astrophys. J.*, 167, 499

Bailyn, C. D. 1995, *Ann. Rev. Astron. Astrophys.*, 33, 133

Bastian, N. & Lardo, C. 2018, *Ann. Rev. Astron. Astrophys.*, 56, 83

Baumgardt, H. & Hilker, M. 2018, *Mon. Not. Roy. Astron. Soc.*, 478, 1520

Baumgardt, H. & Vasiliev, E. 2021, *Mon. Not. Roy. Astron. Soc.*, 505, 5957

Bayo, A., Rodrigo, C., Barrado Y Navascués, D., et al. 2008, *Astron. Astrophys.*, 492, 277

Bédard, A., Bergeron, P., Brassard, P., & Fontaine, G. 2020, *Astrophys. J.*, 901, 93

Bedin, L. R., Piotto, G., Anderson, J., et al. 2004, *Astrophys. J. Lett.*, 605, L125

Bedin, L. R., Piotto, G., Zoccali, M., et al. 2000, *Astron. Astrophys.*, 363, 159

Bellini, A., Anderson, J., Bedin, L. R., et al. 2017a, *Astrophys. J.*, 842, 6

Bellini, A., Anderson, J., Salaris, M., et al. 2013, *Astrophys. J. Lett.*, 769, L32

Bellini, A., Anderson, J., van der Marel, R. P., et al. 2017b, *Astrophys. J.*, 842, 7

Bellini, A., Piotto, G., Bedin, L. R., et al. 2009, *Astron. Astrophys.*, 507, 1393

Bergeron, P., Wesemael, F., & Beauchamp, A. 1995, *Pub. Astron. Soc. Pac.*, 107, 1047

Bianchi, L., Shiao, B., & Thilker, D. 2017, *Astrophys. J. Suppl.*, 230, 24

Binney, J. & Tremaine, S. 2008, Galactic Dynamics: Second Edition (Princeton University Press)

Boffin, H.M.J., C. G. & G., B., eds. 2015, Astrophysics and Space Science Library, Vol. 413, Ecology of Blue Straggler Stars

Bogdanov, S., van den Berg, M., Heinke, C. O., et al. 2010, *Astrophys. J.*, 709, 241

Bonnarel, F., Fernique, P., Bienaymé, O., et al. 2000, *Astron. Astrophys. Suppl.*, 143, 33

Brocato, E., Matteucci, F., Mazzitelli, I., & Tornambe, A. 1990, *Astrophys. J.*, 349, 458

Brown, T. M., Cassisi, S., D'Antona, F., et al. 2016, *Astrophys. J.*, 822, 44

Brown, T. M., Lanz, T., Sweigart, A. V., et al. 2012, *Astrophys. J.*, 748, 85

Brown, T. M., Sweigart, A. V., Lanz, T., Landsman, W. B., & Hubeny, I. 2001, *Astrophys. J.*, 562, 368

Brown, T. M., Sweigart, A. V., Lanz, T., et al. 2010a, *Astrophys. J.*, 718, 1332

Brown, W. R., Kilic, M., Allende Prieto, C., & Kenyon, S. J. 2010b, *Astrophys. J.*, 723, 1072

Burbidge, E. M. & Sandage, A. 1958, *Astrophys. J.*, 128, 174

Burstein, D., Bertola, F., Buson, L. M., Faber, S. M., & Lauer, T. R. 1988, *Astrophys. J.*, 328, 440

Cadelano, M., Chen, J., Pallanca, C., et al. 2020, *Astrophys. J.*, 905, 63

Cadelano, M., Ferraro, F. R., Dalessandro, E., et al. 2022, *Astrophys. J.*, 941, 69

Cadelano, M., Ferraro, F. R., Istrate, A. G., et al. 2019, *Astrophys. J.*, 875, 25

Calamida, A., Corsi, C. E., Bono, G., et al. 2008, *Astrophys. J. Lett.*, 673, L29

Calamida, A., Stetson, P. B., Bono, G., et al. 2005, *Astrophys. J. Lett.*, 634, L69

Calamida, A., Strampelli, G., Rest, A., et al. 2017, *Astron. J.*, 153, 175

Calamida, A., Zocchi, A., Bono, G., et al. 2020, *Astrophys. J.*, 891, 167

Caloi, V., Castellani, V., & Panagia, N. 1982, *Astron. Astrophys.*, 107, 145

Cardelli, J. A., Clayton, G. C., & Mathis, J. S. 1989, *Astrophys. J.*, 345, 245

Carretta, E., Bragaglia, A., Gratton, R. G., et al. 2010, *Astron. Astrophys.*, 516, A55

Carroll, B. W. & Ostlie, D. A. 2017, An introduction to modern astrophysics, Second Edition

Cassisi, S., Salaris, M., & Irwin, A. W. 2003, *Astrophys. J.*, 588, 862

Castellani, M. & Castellani, V. 1993, *Astrophys. J.*, 407, 649

Castellani, M., Castellani, V., & Prada Moroni, P. G. 2006, *Astron. Astrophys.*, 457, 569

Castelli, F., Gratton, R. G., & Kurucz, R. L. 1997, *Astron. Astrophys.*, 318, 841

Castelli, F. & Kurucz, R. L. 2003, in Modelling of Stellar Atmospheres, ed. N. Piskunov, W. W. Weiss, & D. F. Gray, Vol. 210, A20

Catelan, M. 2009, Astrophysics and Space Science, 320, 261

Catelan, M. 2013, in European Physical Journal Web of Conferences, Vol. 43, European Physical Journal Web of Conferences, 01001

Charpinet, S., Van Grootel, V., Fontaine, G., et al. 2011, *Astron. Astrophys.*, 530, A3

Chayer, P., Dixon, W. V., Fullerton, A. W., Ooghe-Tabanou, B., & Reid, I. N. 2015, *Mon. Not. Roy. Astron. Soc.*, 452, 2292

Chen, J., Cadelano, M., Pallanca, C., et al. 2023, *Astrophys. J.*, 948, 84

Chen, J., Ferraro, F. R., Cadelano, M., et al. 2022, *Astrophys. J.*, 934, 93

Chen, J., Ferraro, F. R., Cadelano, M., et al. 2021, Nature Astronomy, 5, 1170

Chung, C., Yoon, S.-J., & Lee, Y.-W. 2017, *Astrophys. J.*, 842, 91

Cohen, R. E. & Sarajedini, A. 2012, *Mon. Not. Roy. Astron. Soc.*, 419, 342

Cohn, H. N., Lugger, P. M., Couch, S. M., et al. 2010, *Astrophys. J.*, 722, 20

Constantino, T., Campbell, S. W., Christensen-Dalsgaard, J., Lattanzio, J. C., & Stello, D. 2015, *Mon. Not. Roy. Astron. Soc.*, 452, 123

Correnti, M., Gennaro, M., Kalirai, J. S., Cohen, R. E., & Brown, T. M. 2018, *Astrophys. J.*, 864, 147

Dalessandro, E., Ferraro, F. R., Massari, D., et al. 2013, *Astrophys. J.*, 778, 135

Dalessandro, E., Salaris, M., Ferraro, F. R., Mucciarelli, A., & Cassisi, S. 2013, Monthly Notices of the Royal Astronomical Society, 430, 459

D'Antona, F., Caloi, V., & Ventura, P. 2010, *Mon. Not. Roy. Astron. Soc.*, 405, 2295

Dattatrey, A. K., Yadav, R. K. S., Rani, S., et al. 2023, *Astrophys. J.*, 943, 130

D'Cruz, N. L., Dorman, B., Rood, R. T., & O'Connell, R. W. 1996, *Astrophys. J.*, 466, 359

D'Cruz, N. L., O'Connell, R. W., Rood, R. T., et al. 2000, *Astrophys. J.*, 530, 352

De Marchi, G., Paresce, F., & Pulone, L. 2000, *Astrophys. J.*, 530, 342

De Marco, O., Shara, M. M., Zurek, D., et al. 2005, *Astrophys. J.*, 632, 894

Denissenkov, P. A., VandenBerg, D. A., Kopacki, G., & Ferguson, J. W. 2017, *Astrophys. J.*, 849, 159

D'Ercole, A., Vesperini, E., D'Antona, F., McMillan, S. L. W., & Recchi, S. 2008, *Mon. Not. Roy. Astron. Soc.*, 391, 825

Dieball, A., Rasekh, A., Knigge, C., Shara, M., & Zurek, D. 2017, *Mon. Not. Roy. Astron. Soc.*, 469, 267

Dixon, W. V., Chayer, P., Latour, M., Miller Bertolami, M. M., & Benjamin, R. A. 2017, *Astron. J.*, 154, 126

Dixon, W. V., Chayer, P., Reid, I. N., & Miller Bertolami, M. M. 2019, *Astron. J.*, 157, 147

Djorgovski, S. & King, I. R. 1986, *Astrophys. J. Lett.*, 305, L61

Dorman, B., O'Connell, R. W., & Rood, R. T. 1995, *Astrophys. J.*, 442, 105

Dorman, B., Rood, R. T., & O'Connell, R. W. 1993, *Astrophys. J.*, 419, 596

Ferraro, F. R., Beccari, G., Dalessandro, E., et al. 2009, *Nature*, 462, 1028

Ferraro, F. R., Paltrinieri, B., & Cacciari, C. 1999, *Mem. Societa Astronomica Italiana*, 70, 599

Fiorentino, G., Marconi, M., Bono, G., et al. 2015, *Astrophys. J.*, 810, 15

Fitzpatrick, E. L. 1999, *Pub. Astron. Soc. Pac.*, 111, 63

Gaia Collaboration, Brown, A. G. A., Vallenari, A., et al. 2021, *Astron. Astrophys.*, 649, A1

Gaia Collaboration, Helmi, A., van Leeuwen, F., et al. 2018, *Astron. Astrophys.*, 616, A12

Gaia Collaboration, Prusti, T., de Bruijne, J. H. J., et al. 2016, *Astron. Astrophys.*, 595, A1

Ghosh, S. K., Tandon, S. N., Singh, S. K., et al. 2022, Journal of Astrophysics and Astronomy, 43, 77

Gieles, M. & Portegies Zwart, S. F. 2011, *Mon. Not. Roy. Astron. Soc.*, 410, L6

Gratton, R., Bragaglia, A., Carretta, E., et al. 2019, *Astron. Astrophys. Rev.*, 27, 8

Gratton, R. G., Carretta, E., Bragaglia, A., Lucatello, S., & D'Orazi, V. 2010, *Astron. Astrophys.*, 517, A81

Greggio, L. & Renzini, A. 1990, *Astrophys. J.*, 364, 35

Greggio, L. & Renzini, A. 1999, *Mem. Societa Astronomica Italiana*, 70, 691

Greggio, L. & Renzini, A. 2011, The Fundamentals of Evolutionary Population Synthesis (John Wiley & Sons, Ltd), 35–59

Grindlay, J. E., Heinke, C. O., Edmonds, P. D., Murray, S. S., & Cool, A. M. 2001, *Astrophys. J. Lett.*, 563, L53

Grundahl, F., Catelan, M., Landsman, W. B., Stetson, P. B., & Andersen, M. I. 1999, *Astrophys. J.*, 524, 242

Grundahl, F., VandenBerg, D. A., & Andersen, M. I. 1998, *Astrophys. J. Lett.*, 500, L179

Harris, W. E. 1996, *Astron. J.*, 112, 1487

Harris, W. E. 2018, *Astron. J.*, 156, 296

Heber, U. & Kudritzki, R. P. 1986, *Astron. Astrophys.*, 169, 244

Hidalgo, S. L., Pietrinferni, A., Cassisi, S., et al. 2018, *Astrophys. J.*, 856, 125

Hills, J. G. & Day, C. A. 1976, *Astrophysical Letters*, 17, 87

Husfeld, D., Butler, K., Heber, U., & Drilling, J. S. 1989, *Astron. Astrophys.*, 222, 150

Hutchings, J. B., Postma, J., Asquin, D., & Leahy, D. 2007, *Pub. Astron. Soc. Pac.*, 119, 1152

Ibata, R. A., Bellazzini, M., Malhan, K., Martin, N., & Bianchini, P. 2019, Nature Astronomy, 3, 667

Iben, I., J. & Renzini, A. 1983, *Ann. Rev. Astron. Astrophys.*, 21, 271

Iben, Icko, J. 1967, *Ann. Rev. Astron. Astrophys.*, 5, 571

Iben, Icko, J. 1991, *Astrophys. J. Suppl.*, 76, 55

Iben, Icko, J. & Rood, R. T. 1970, *Astrophys. J.*, 161, 587

Istrate, A. G., Marchant, P., Tauris, T. M., et al. 2016, *Astron. Astrophys.*, 595, A35

Jadhav, V. V., Pandey, S., Subramaniam, A., & Sagar, R. 2021, Journal of Astrophysics and Astronomy, 42, 89

Jain, R., Vig, S., & Ghosh, S. K. 2019, *Mon. Not. Roy. Astron. Soc.*, 485, 2877

Johnson, C. I. & Pilachowski, C. A. 2010, *Astrophys. J.*, 722, 1373

Johnson, H. L. & Sandage, A. R. 1955, *Astrophys. J.*, 121, 616

Joo, S.-J. & Lee, Y.-W. 2013, *Astrophys. J.*, 762, 36

Kalirai, J. S., Saul Davis, D., Richer, H. B., et al. 2009, *Astrophys. J.*, 705, 408

Kaluzny, J. & Thompson, I. B. 2003, *Astron. J.*, 125, 2534

Kharchenko, N. V., Piskunov, A. E., Schilbach, E., Röser, S., & Scholz, R. D. 2013, *Astron. Astrophys.*, 558, A53

King, I. R., Anderson, J., Cool, A. M., & Piotto, G. 1998, *Astrophys. J. Lett.*, 492, L37

Knigge, C., Zurek, D. R., Shara, M. M., & Long, K. S. 2002, *Astrophys. J.*, 579, 752

Koester, D. 2010, *Mem. Societa Astronomica Italiana*, 81, 921

Krause, M. G. H., Offner, S. S. R., Charbonnel, C., et al. 2020, *Space Sci. Rev.*, 216, 64

Krauss, L. M. & Chaboyer, B. 2003, Science, 299, 65

Kumar, A., Ghosh, S. K., Hutchings, J., et al. 2012, in Society of Photo-Optical Instrumentation Engineers (SPIE) Conference Series, Vol. 8443, Space Telescopes and Instrumentation 2012: Ultraviolet to Gamma Ray, ed. T. Takahashi, S. S. Murray, & J.-W. A. den Herder, 84431N

Kumar, R., Pradhan, A. C., Sahu, S., et al. 2023, *Mon. Not. Roy. Astron. Soc.*, 522, 847

Kunder, A., Stetson, P. B., Catelan, M., Walker, A. R., & Amigo, P. 2013, *Astron. J.*, 145, 33

Kurucz, R. L. 1970, SAO Special Report, 309

Landsman, W. B., O'Connell, R. W., Whitney, J. H., et al. 1992, *Astrophys. J. Lett.*, 395, L21

Latour, M., Calamida, A., Husser, T. O., et al. 2021, *Astron. Astrophys.*, 653, L8

Latour, M., Randall, S. K., Calamida, A., Geier, S., & Moehler, S. 2018, *Astron. Astrophys.*, 618, A15

Latour, M., Randall, S. K., Fontaine, G., et al. 2014, *Astrophys. J.*, 795, 106

Lee, Y.-W., Joo, S.-J., Han, S.-I., et al. 2005, *Astrophys. J. Lett.*, 621, L57

Levenhagen, R. S., Diaz, M. P., Coelho, P. R. T., & Hubeny, I. 2017, *Astrophys. J. Suppl.*, 231, 1

Lovisi, L., Mucciarelli, A., Lanzoni, B., et al. 2012, *Astrophys. J.*, 754, 91

Marino, A. F., Milone, A. P., Yong, D., et al. 2017, *Astrophys. J.*, 843, 66

Massari, D., Fiorentino, G., McConnachie, A., et al. 2016, *Astron. Astrophys.*, 586, A51

McCall, M. L. 2004, *Astron. J.*, 128, 2144

McCrea, W. H. 1964, *Mon. Not. Roy. Astron. Soc.*, 128, 147

McDonald, I. & Zijlstra, A. A. 2015, *Mon. Not. Roy. Astron. Soc.*, 448, 502

Mestel, L. 1952, *Mon. Not. Roy. Astron. Soc.*, 112, 598

Mikulášek, Z., Paunzen, E., Hümmerich, S., et al. 2019, in Astronomical Society of the Pacific Conference Series, Vol. 518, Physics of Magnetic Stars, ed. D. O. Kudryavtsev, I. I. Romanyuk, & I. A. Yakunin, 117

Miller Bertolami, M. M. 2016, *Astron. Astrophys.*, 588, A25

Milone, A. P. & Marino, A. F. 2022, Universe, 8, 359

Milone, A. P., Marino, A. F., Dotter, A., et al. 2014, *Astrophys. J.*, 785, 21

Milone, A. P., Marino, A. F., Piotto, G., et al. 2013, *Astrophys. J.*, 767, 120

Milone, A. P., Marino, A. F., Piotto, G., et al. 2015, *Astrophys. J.*, 808, 51

Milone, A. P., Marino, A. F., Renzini, A., et al. 2018, *Mon. Not. Roy. Astron. Soc.*, 481, 5098

Moehler, S. 2001, *Pub. Astron. Soc. Pac.*, 113, 1162

Moehler, S. & Bono, G. 2008, arXiv e-prints, arXiv:0806.4456

Moehler, S., Dreizler, S., Lanz, T., et al. 2011, *Astron. Astrophys.*, 526, A136

Moehler, S., Landsman, W. B., Lanz, T., & Miller Bertolami, M. M. 2019, *Astron. Astrophys.*, 627, A34

Momany, Y., Bedin, L. R., Cassisi, S., et al. 2004, *Astron. Astrophys.*, 420, 605

Momany, Y., Piotto, G., Recio-Blanco, A., et al. 2002, *Astrophys. J. Lett.*, 576, L65

Momany, Y., Zaggia, S., Montalto, M., et al. 2020, Nature Astronomy, 4, 1092

Moni Bidin, C., Villanova, S., Piotto, G., et al. 2012, *Astron. Astrophys.*, 547, A109

Moni Bidin, C., Villanova, S., Piotto, G., Moehler, S., & D'Antona, F. 2011, *Astrophys. J. Lett.*, 738, L10

Mucciarelli, A., Lovisi, L., Ferraro, F. R., et al. 2014, *Astrophys. J.*, 797, 43

Naoz, S. & Fabrycky, D. C. 2014, *Astrophys. J.*, 793, 137

Nardiello, D., Libralato, M., Piotto, G., et al. 2018, *Mon. Not. Roy. Astron. Soc.*, 481, 3382

Ngeow, C.-C., Bhardwaj, A., Graham, M. J., et al. 2023, *Astron. J.*, 165, 190

Norris, J. E. 2004, *Astrophys. J. Lett.*, 612, L25

Norris, J. E. & Da Costa, G. S. 1995, *Astrophys. J. Lett.*, 441, L81

Pacheco, T. A., Diaz, M. P., Levenhagen, R. S., & Coelho, P. R. T. 2021, *Astrophys. J. Suppl.*, 256, 41

Pancino, E., Ferraro, F. R., Bellazzini, M., Piotto, G., & Zoccali, M. 2000, *Astrophys. J. Lett.*, 534, L83

Pandey, S., Subramaniam, A., & Jadhav, V. V. 2021, *Mon. Not. Roy. Astron. Soc.*, 507, 2373

Perets, H. B. & Fabrycky, D. C. 2009, *Astrophys. J.*, 697, 1048

Pichardo Marcano, M., Rivera Sandoval, L. E., Maccarone, T. J., et al. 2023, *Mon. Not. Roy. Astron. Soc.*, 521, 5026

Pietrinferni, A., Hidalgo, S., Cassisi, S., et al. 2021, *Astrophys. J.*, 908, 102

Piotto, G., Bedin, L. R., Anderson, J., et al. 2007, *Astrophys. J. Lett.*, 661, L53

Piotto, G., Milone, A. P., Bedin, L. R., et al. 2015, *Astron. J.*, 149, 91

Piotto, G., Villanova, S., Bedin, L. R., et al. 2005, *Astrophys. J.*, 621, 777

Postma, J., Hutchings, J. B., & Leahy, D. 2011, *Pub. Astron. Soc. Pac.*, 123, 833

Postma, J. E. & Leahy, D. 2017, *Pub. Astron. Soc. Pac.*, 129, 115002

Postma, J. E. & Leahy, D. 2021, *J. of Astrophy. & Astron.*, 42, 30

Prabhu, D. S., Subramaniam, A., & Sahu, S. 2021a, *Astrophys. J.*, 908, 66

Prabhu, D. S., Subramaniam, A., & Sahu, S. 2021b, *J. of Astrophy. & Astron.*, 42, 66

Prabhu, D. S., Subramaniam, A., Sahu, S., et al. 2022, *Astrophys. J. Lett.*, 939, L20

Raso, S., Ferraro, F. R., Dalessandro, E., et al. 2017, *Astrophys. J.*, 839, 64

Rauch, T. & Deetjen, J. L. 2003, in Astronomical Society of the Pacific Conference Series, Vol. 288, Stellar Atmosphere Modeling, ed. I. Hubeny, D. Mihalas, & K. Werner, 103

Rebassa-Mansergas, A., Solano, E., Jiménez-Esteban, F. M., et al. 2021, *Mon. Not. Roy. Astron. Soc.*, 506, 5201

Recio-Blanco, A., Aparicio, A., Piotto, G., de Angeli, F., & Djorgovski, S. G. 2006, *Astron. Astrophys.*, 452, 875

Recio-Blanco, A., Piotto, G., Aparicio, A., & Renzini, A. 2002, *Astrophys. J.*, 572, L71

Reimers, D. 1977, *Astron. Astrophys.*, 57, 395

Rood, R. T. 1973, *Astrophys. J.*, 184, 815

Sahu, S., Subramaniam, A., Simunovic, M., et al. 2019, *Astrophys. J.*, 876, 34

Sahu, S., Subramaniam, A., Singh, G., et al. 2022, *Mon. Not. Roy. Astron. Soc.*, 514, 1122

Salaris, M., Cassisi, S., & Pietrinferni, A. 2016, *Astron. Astrophys.*, 590, A64

Salaris, M., Cassisi, S., Pietrinferni, A., & Hidalgo, S. 2022, *Mon. Not. Roy. Astron. Soc.*, 509, 5197

Sandage, A. & Wallerstein, G. 1960, *Astrophys. J.*, 131, 598

Sandage, A. & Wildey, R. 1967, *Astrophys. J.*, 150, 469

Sandage, A. R. 1953, *Astron. J.*, 58, 61

Schiavon, R. P., Dalessandro, E., Sohn, S. T., et al. 2012, *Astron. J.*, 143, 121

Schwarzschild, M. & Härm, R. 1962, *Astrophys. J.*, 136, 158

Schwarzschild, M. & Härm, R. 1965, *Astrophys. J.*, 142, 855

Searle, L. & Zinn, R. 1978, *Astrophys. J.*, 225, 357

Shapley, H. 1918, *Astrophys. J.*, 48, 154

Shara, M. M., Hinkley, S., Zurek, D. R., Knigge, C., & Dieball, A. 2005, *Astron. J.*, 130, 1829

Shu, F. H. 1982, The Physical Universe (University Science Books)

Sindhu, N., Subramaniam, A., Jadhav, V. V., et al. 2019, *Astrophys. J.*, 882, 43

Singh, G., Sahu, S., Subramaniam, A., & Yadav, R. K. S. 2020, *Astrophys. J.*, 905, 44

Singh, K. P. 2022, in Handbook of X-ray and Gamma-ray Astrophysics, 83

Sirianni, M., Jee, M. J., Benítez, N., et al. 2005, *Pub. Astron. Soc. Pac.*, 117, 1049

Smith, H. A. 1995, Cambridge Astrophysics Series, 27

Stetson, P. B. 1987, *Pub. Astron. Soc. Pac.*, 99, 191

Stetson, P. B., Pancino, E., Zocchi, A., Sanna, N., & Monelli, M. 2019, *Mon. Not. Roy. Astron. Soc.*, 485, 3042

Strickler, R. R., Cool, A. M., Anderson, J., et al. 2009, *Astrophys. J.*, 699, 40

Suntzeff, N. B. & Kraft, R. P. 1996, *Astron. J.*, 111, 1913

Sweigart, A. V. 1997, *Astrophys. J. Lett.*, 474, L23

Tailo, M., Di Criscienzo, M., D'Antona, F., Caloi, V., & Ventura, P. 2016, *Mon. Not. Roy. Astron. Soc.*, 457, 4525

Tandon, S. N., Postma, J., Joseph, P., et al. 2020, *Astron. J.*, 159, 158

Tandon, S. N., Subramaniam, A., Girish, V., et al. 2017, *Astron. J.*, 154, 128

Taylor, M. B. 2005, in Astronomical Society of the Pacific Conference Series, Vol. 347, Astronomical Data Analysis Software and Systems XIV, ed. P. Shopbell, M. Britton, & R. Ebert, 29

Thompson, H. M. A., Keenan, F. P., Dufton, P. L., et al. 2007, *Mon. Not. Roy. Astron. Soc.*, 378, 1619

Tremblay, P. E., Bergeron, P., & Gianninas, A. 2011, *Astrophys. J.*, 730, 128

Valcin, D., Jimenez, R., Verde, L., Bernal, J. L., & Wandelt, B. D. 2021, *J. of Cosmology & Astroparticle Phy.*, 2021, 017

van den Bergh, S. 1967, *Astron. J.*, 72, 70

Vasiliev, E. & Baumgardt, H. 2021, *Mon. Not. Roy. Astron. Soc.*, 505, 5978

Werner, K., Deetjen, J. L., Dreizler, S., et al. 2003, in Astronomical Society of the Pacific Conference Series, Vol. 288, Stellar Atmosphere Modeling, ed. I. Hubeny, D. Mihalas, & K. Werner, 31

Werner, K. & Dreizler, S. 1999, Journal of Computational and Applied Mathematics, 109, 65

Whitney, J. H., O'Connell, R. W., Rood, R. T., et al. 1994, *Astron. J.*, 108, 1350

Whitney, J. H., Rood, R. T., O'Connell, R. W., et al. 1998, *Astrophys. J.*, 495, 284

Worthey, G. 1994, *Astrophys. J. Suppl.*, 95, 107

Yi, S. K., Lee, J., Sheen, Y.-K., et al. 2011, *Astrophys. J. Suppl.*, 195, 22

Zinn, R. & Searle, L. 1976, *Astrophys. J.*, 209, 734

Zinn, R. J., Newell, E. B., & Gibson, J. B. 1972, *Astron. Astrophys.*, 18, 390